

EXPERIMENTAL TESTING OF UNSTEADY THREE-DIMENSIONAL LIFTING
SURFACE THEORIES FOR INCOMPRESSIBLE FLOW

Horst Hertrich

(NASA-TT-F-16200) EXPERIMENTAL TESTING OF
UNSTEADY THREE-DIMENSIONAL LIFTING SURFACE
THEORIES FOR INCOMPRESSIBLE FLOW (Scientific
Translation Service) 108 p HC \$5.25

N75-16513

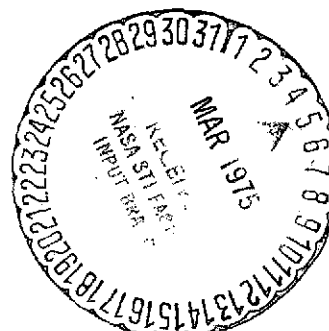
Unclas

CSCL 01A G3/02 10247

Translation of "Zur experimen-
tellen Prüfung instationärer
dreidimensionaler Tragflächen-
theorien bei inkompressibler
Strömung", Communications from
the Max Planck Institute for
Fluid Dynamics and the Aero-
dynamic Test Facility. No. 40,
Gottingen, 1967, 114 pages.

PRICES SUBJECT TO CHANGE

Reproduced by
**NATIONAL TECHNICAL
INFORMATION SERVICE**
US Department of Commerce
Springfield, VA. 22151



NATIONAL AERONAUTICS AND SPACE ADMINISTRATION
WASHINGTON, D. C. 20546 FEBRUARY 1975

1. Report No. NASA TT F 16,200	2. Government Accession No.	3. Recipient's Catalog No.	
4. Title and Subtitle Experimental Testing of Unsteady Three-Dimensional Lifting Surface Theories for Incompressible Flow		5. Report Date February 28, 1975	6. Performing Organization Code
7. Author(s) Horst Hertrich		8. Performing Organization Report No.	
Edited by W. Tollmien and H. Schlichting		10. Work Unit No.	
9. Performing Organization Name and Address SCITRAN Box 5456 Santa Barbara, CA 93108		11. Contract or Grant No. NASW-2483	
12. Sponsoring Agency Name and Address National Aeronautics and Space Administration Washington, D.C. 20546		13. Type of Report and Period Covered Translation	
		14. Sponsoring Agency Code	
15. Supplementary Notes Translation of "Zur experimentellen Prüfung instationärer dreidimensionaler Tragflächentheorien bei inkompressibler Strömung", Communications from the Max Planck Institute for Fluid Dynamics and the Aerodynamic Test Facility. No. 40, Göttingen, 1967, 114 pages.			
16. Abstract Numerous pressure distribution measurements were made on harmonically oscillating rigid semiwing models with and without a rudder in the 3 m wind tunnel of the AVA (Aerodynamic Test Facility) in order to experimentally test various unsteady lifting surface theories. The measurements were carried out with a rectangular and a sweptback wing model with constant chord $l=0.6$ m. Both models have NACA 0012 profiles. The rudder chord was 30% of the wing chord. The model aspect ratios could be adjusted for side ratios of $\Lambda=3.1$ and 2.5. The unsteady differential pressures were determined through hose lines in 7 model sections having 20 measurement points each. Investigations were carried out for pitch oscillations around various axes perpendicular to the incident flow direction and there were rudder rotational oscillations around the rudder leading edge. This was done at reduced frequencies of $ \omega^* =0, 0.13$ to 0.76 , as well as for the case where there was no incident flow (determination of air mass moving with the models). The measurement results were compared with a lifting surface method, a lifting line method, and the plane theory.			
17. Key Words (Selected by Author(s))		18. Distribution Statement Unclassified - Unlimited	
19. Security Classif. (of this report) Unclassified	20. Security Classif. (of this page) Unclassified	21. No. of Pages 107	22. Price

TABLE OF CONTENTS

	Page
NOTATION	iv
1. INTRODUCTION	1
2. EXPERIMENTAL PRINCIPLE	3
3. TEST STAND	6
4. MODELS	9
5. ELECTRONIC MEASUREMENT TECHNIQUES	13
6. THEORIES USED IN THE COMPARISON	17
6.1. Preliminary Remarks	17
6.2. Two-Dimensional Theory	20
6.2.1. Integral representation of pressure	20
6.2.2. Wing rotation	23
6.2.3. Rudder rotation	25
6.2.4. Simultaneous fin and rudder rotation	27
6.3. Three-Dimensional Lifting Surface Theory	27
6.3.1. General integral equation	27
6.3.2. Solution methods	28
6.4. Theory of the Large Aspect Ratio Oscillating Lifting Surface	31
6.4.1. Integral equation of the large aspect ratio lifting surface	31
6.4.2. Solution methods	32
7. MEASUREMENT RESULTS	35
7.1. Oscillations in Quiet Air	35
7.2. Steady Flow	37
7.3. Oscillations in the Case of Incident Flow	41
7.3.1. Preliminary remark	41
7.3.2. Wing rotation	43
7.3.3. Rudder rotation	72
7.3.4. Simultaneous fin and rudder rotation	92
8. SUMMARY	94
9. REFERENCES	95
APPENDIX	100

NOTATION*

Geometrical and Elastomechanical Variables

/3**

t	[sec]	Time
x, y, z	[m]	Cartesian coordinates of the reference system rigidly attached with the central position of the oscillating wing; coordinate direction according to norm LN9300
$\zeta(x, y, t)$	[m]	Oscillation motion of lifting surface
$x_0(y)$	[m]	Coordinate of lifting surface center
x_d	[m]	Coordinate of wing rotation axis
$x_v(y)$	[m]	Coordinate of lifting surface leading edge
$x_h(y)$	[m]	Coordinate of lifting surface trailing edge
$x_R(y)$	[m]	Coordinate of rudder leading edge
$x_m(y)$	[m]	Coordinate of reference axis of the local moment
χ		Dimensionless coordinate, Equation (43)
χ_m		Coordinate of reference axis of local moment, Equation (46)
ξ		Dimensionless coordinate = x/c
u, θ		Elliptical coordinates in the plane $y = \text{const}$, Equation (2)
$\cos \Psi$		Coordinate in span direction = y/s

/4

*A physical system of measures with the units kg, m, sec for mass, length, and time is used.

**Numbers in the margin indicate pagination of original foreign text.

5
6
7
8

l	[m]	Lifting surface chord
c	[m]	One-half lifting surface chord $= l/2$
b	[m]	Span of lifting surface
s	[m]	Semispan of lifting surface $= b/2$
$\epsilon(y)$		Distance of rotational axis from lifting surface center $= [x_d - x_0(y)]/c$
F	[m ²]	Wing area
Λ		Wing aspect ratio $= b^2/F$
B		Rotation amplitude of lifting surface
C		Rotation amplitude of rudder
ν	[s ⁻¹]	Oscillation frequency
ω	[s ⁻¹]	Complex circular frequency $= 2\pi i\nu$

Aerodynamic Variables

V	[m s ⁻¹]	Incident flow velocity
w	[m s ⁻¹]	Downwind
ω^*		Complex reduced frequency, referred to one-half of the lifting surface chord $= \omega c/V$
Ω		Complex reduced frequency, referred to one-half the span $= \omega s/V$
μ	[kg m ⁻¹ s ⁻¹]	Air viscosity
ρ	[kg m ⁻³]	Air density
Re		Reynolds number $= V l \rho / \mu$
Δp	[kg m ⁻¹ s ⁻²]	Pressure jump at lifting surface, Equations (10) and (21)
Π		Amplitude of reduced pressure jump at lifting surface, Equation (5)
Π_b, Π_c		Derivative of reduced pressure jump with respect to the amplitudes B and C ; Equations (69) and (70)
P		Pressure coefficient for simultaneous fin and rudder rotational oscillations, Equation (71)

$T(\omega^*)$		Vortex drag function for two-dimensional flow, Equation (9)	
$T_1(\omega^*, y)$		Modified vortex drag function, Equation (56)	/6
$K(y)$	[m]	Characteristic function: $K_e(y)$ for two-dimensional flow	
$G(u, \theta, \theta')$		Green function	
K_0, K_1		Modified Hankel functions	
$S_n(\Omega, \Psi)$		Auxiliary function	
$f(\omega^*)$		Auxiliary function	
$T_r(x)$		Tchebyscheff polynomial of the first kind	
$J(y)$		Downwind integral	
L	[kg m s ⁻²]	Amplitude of wing aerodynamic force	
M	[kg m ² s ⁻²]	Amplitude of wing pitch moment	
R	[kg m s ⁻²]	Amplitude of rudder aerodynamic force	
N	[kg m ² s ⁻²]	Amplitude of rudder moment	
k_b, k_c		Derivatives of the aerodynamic wing force with respect to the rotation amplitudes B and C; Equations (14) and (31)	
m_b, m_c		Derivatives of the wing moment with respect to the rotational amplitudes B and C; Equations (15) and (32)	
r_b, r_c		Derivatives of the rudder aerodynamic force with respect to the rotational amplitudes B and C; Equations (19) and (33)	
n_b, n_c		Derivatives of the rudder moment with respect to the rotational amplitudes B and C; Equations (20) and (34)	/7
$c_a(y)$		Amplitude of the local coefficient of the wing lift; Equation (44)	
$c_m(y)$		Amplitude of local coefficient of wing moment; Equation (45)	
$p(x, z, t)$	[kg m ⁻¹ s ⁻²]	Local pressure in the profile plane	

a_r^*	Coefficients of the pressure distribution law; Equation (50)
$h_r(x)$	Normal distribution, Equation (42)
d_{rn}^p	Coefficients; Equations (47) and (48)

EXPERIMENTAL TESTING OF UNSTEADY THREE-DIMENSIONAL LIFTING SURFACE THEORIES FOR INCOMPRESSIBLE FLOW*

Horst Hertrich

1. Introduction

Over the last few years, the treatment of the unsteady lifting surface theory has made significant advances. In particular, the calculation of the aerodynamic forces over rigid oscillating lifting surfaces of finite span has been significantly improved. The preliminary work for this was already done in 1940 with the basic paper of H. G. Kuessner [9] on the integral equation of the harmonically oscillating lifting surface for compressible subsonic flow. Later on, C. E. Watkins, H. L. Runyan, and D. S. Woolston [1] numerically solved the kernel function of this integral equation. Based on this, a number of collocation methods were developed for calculating the unsteady aerodynamic forces [2, 3, 4], etc. Other lifting surface methods use a small box method, in which the lifting surface is covered with a network of small boxes [5, 6].

In the older lifting line methods, the vortices are concentrated along a line. The lifting line method is limited to aspect ratios $\Lambda > 3$. Lifting surface methods, on the other hand, can also be used for lifting surfaces with small aspect

*Communications from the Max Planck Institute for Fluid Dynamics and the Aerodynamic Test Facility. W. Tollmein and H. Schlichting, editors.

ratios because of their vortex distribution over the area. Up to the present time, it has not been possible to establish lifting surface methods for the subsonic range which would lead to satisfactory results for wings in combination with rudders. Here one must resort to lifting line methods or the strip theory, which is essentially two-dimensional.

The experimental development has not stayed abreast of the development in the theoretical area. Numerous investigations of unsteady aerodynamic forces under plane and three-dimensional flow conditions have been carried out, both for incompressible as well as for compressible conditions. However, with only a few exceptions, these are global measurements which do not give any information about the distribution of the forces. The experimental verification of unsteady aerodynamic force theories using only global measurements is unsatisfactory. Only an investigation of the unsteady pressure distribution will provide enough information to determine whether a theory can be used.

Pressure distribution measurements were carried out only rarely because even the measurement of global unsteady aerodynamic forces was connected with considerable difficulties, both for planning the experiment and for making measurements. This is especially true for wind tunnel measurements with wings with oscillating rudders, which up to the present time have only been carried out at the NLR* in Amsterdam. Critical comparisons of various aerodynamic force theories using measured three-dimensional pressure distributions have been published to only a very limited extent.

*NLR = Nationaal Lucht- en Ruimtevaartlaboratorium, Amsterdam (National Aerodynamics and Space Laboratory).

2. Experiment Principle

The first measurements of unsteady pressures over a wing with an oscillating rudder were carried out by H. Drescher [16] in 1937 using a small water tunnel of the AVA. The results of the investigations, which were carried out over several years, were later on partially published in the form of a dissertation [17]. In the middle of the Fifties, such measurements were again resumed almost at the same time in England and the USA [18, 19]. After this, this was also again resumed at the NLR in Amsterdam [20] and at the ONERA* in France [21].

/9

The measurements performed up to the present can be divided into two groups, depending on the measurement methods used. The first measurement method consists of assigning a pressure transducer installed in the model with each measurement point. The pressure transducer is placed as close as possible to the pressure tap [18, 19, 22]. In the second measurement method, the pressure taps are connected through lines to a central measurement unit outside of the model [16, 23, 24].

The first method was especially appropriate for investigations with two-dimensional flow, because then only one wing section is measured and, therefore, 10 to 12 pressure difference transducers are sufficient to obtain the distribution of the pressure difference between the top side and the bottom side. It is assumed that the models are so thin that only short connection lines between the pressure transducers and the pressure taps are required. This assumption no longer holds for large models, so that it is necessary to use absolute pressure transducers, which at the same time doubles the number of

*ONERA = Office National de'Études et de Recherches Aérospatiales, Paris (National Aerospace Study and Research Office).

pressure transducers [20]. One disadvantage of thin models is the fact that no measurement values are obtained from the immediate vicinity of the model edges because of the considerable thickness of the pressure transducers. Especially in compressible flow, it is only possible to investigate very small models, so that the very small pressure transducers must be used. For this reason, pressure transducers are used at the ONERA which were developed from medical pressure probes for measuring the blood pressure in the heart chamber [25].

In the case of measurements of wings of finite span, usually one was restricted to a few wing sections; for example, in [18], measurements were made in three steps at 50, 86, and 96% of wing span, where there were nine measurement points each. Pressure transducers are expensive and their calibration complicates the experiment. /10

Using the second measurement method, it is possible to interrogate almost an unlimited number of measurement stations using one pressure measurement capsule, assuming that a suitable switching unit is available which connects the tube line coming from each measurement point to the measurement capsule. Plastic hoses or metal tubes can be used as pressure lines. If the inner diameters are between 1 and 1.5 mm, the external diameter of the small metal tubes does not have to be greater than 2 mm. These small dimensions make it possible to carry out measurements with very small wing parts, for example, in the vicinity of a sharp trailing edge. However, a centrally located pressure measurement capsule does not display the oscillating pressure which occurs on the model, but instead a pressure which is changed in amplitude and phase because of the conduction resistance. This means that the dynamic behavior of the lines

must be known in order to be able to determine the pressures which actually occurred on the model. In other words, the lines must be calibrated. This can be done by pressing a pressure connection equipped with a second pressure measurement capsule onto the pressure measurement tap. Then the pressures of the desired frequency are transmitted to the individual lines of the model [24]. By comparing the values measured by the two pressure measurement capsules, it is then possible to determine the behavior of the line for various frequencies and pressure conditions. It has been found that the calibration factor of the line depends to a lesser extent on the pressure amplitudes than on the frequencies and on the static pressure in the line. The resistance increases for decreasing static pressure. In addition, each line system has an upper limiting frequency beyond which signal transmission can no longer occur. Therefore, in the case of measurements under compressible flow conditions, it is necessary to select lines with especially favorable resistance characteristics. High oscillation frequencies are also required in this velocity range in order to achieve high reduced frequencies. Therefore, it is necessary to carry out preliminary experiments using special calibration devices, or to determine the dynamic behavior of the planned line systems by calculations [26, 27].

In the case of measurements in incompressible flow, the calibration procedure for the pressure lines can be considerably simplified. One can use the fact that the differences in static pressures in the various lines are too small to influence the dynamic behavior. This means that only one line has to be calibrated if it can be assumed that the dynamic behavior of all of the lines is identical. In order to bring this about, all tube lines are manufactured of the same components with the same length and dimensions. If one wishes to have a second measurement

/11

tap immediately adjacent to a certain measurement point and if it is desired to connect the pressure measurement capsule installed in the model to it, it is possible to measure the resistance of this (reference) line by carrying out a comparison measurement with the central measurement capsule. We can then arrive at a conclusion for all of the other lines. This principle was first applied by H. Bergh [23] and has the advantage that the calibration takes only a few seconds and no complicated devices are necessary. This very simple procedure can only be used in the low subsonic range, because the condition of small static pressure differences in the lines will only be satisfied under this condition. At higher velocities, it is necessary to investigate the steady pressure distribution over the model and to introduce it as an additional correction factor.

In the case of measurements in incompressible flow, the procedure described has the advantage of a relatively simple experiment, as well as the advantage that the evaluation of the experiment is greatly simplified. This is because only a single complex correction factor must be considered. Therefore, we selected this principle for the extensive experimental program carried out at the AVA [28].

3. Test Stand

During the development of the test stand, we consider the fact that we wished to carry out not only wind tunnel measurements, but also measurements in the laboratory outside of the wind tunnel. The laboratory measurements were required for testing the complicated measurement technology and for determining the pressure distributions in the case of oscillations in quiet air. The test stand, therefore, had to be easily transportable.

/12

One important aspect for the wind tunnel measurements was the investigation of the influence of the wing aspect ratio on the unsteady aerodynamic forces. Since the manufacturing of several models with various aspect ratios would have been too time consuming and costly, it was natural to use the half-model technology customarily used in aerodynamics. In this method, the model is clamped at the channel wall on one side. In addition, we were able to change the penetration of the model into the wind stream.

In order to be able to clamp the model on one side in the free test section of the 3 m wind tunnel, we built a very heavy wooden frame with an installed clamping device with a torsion spring. The torsion spring consists of eight parallel spring rods arranged in a regular octagon. The clamping length could be adjusted continuously [28].

The test stand has wheels and its height can be adjusted with four spindles. During the wind tunnel experiments, it was supported on an elevating platform and was shielded against the wind current by means of a plate which extended from the lower edge of the exit nozzle up to the lower edge of the capture funnel. (Figures 1 and 2). The plate is used as a plane of symmetry, and one should imagine the model to undergo reflection by this plane.

An electrodynamic exciter was located on this wooden frame which was connected to the model track or at the rudder through a rod, which made the model perform rotational oscillations. In the case of rudder rotational oscillations, an air-filled rubber hose served as a restoring spring. The hose was located on the top side of the plate in a cavity of the fuselage-like body, and at the same time, served as a hermetic seal between the model and the plate.

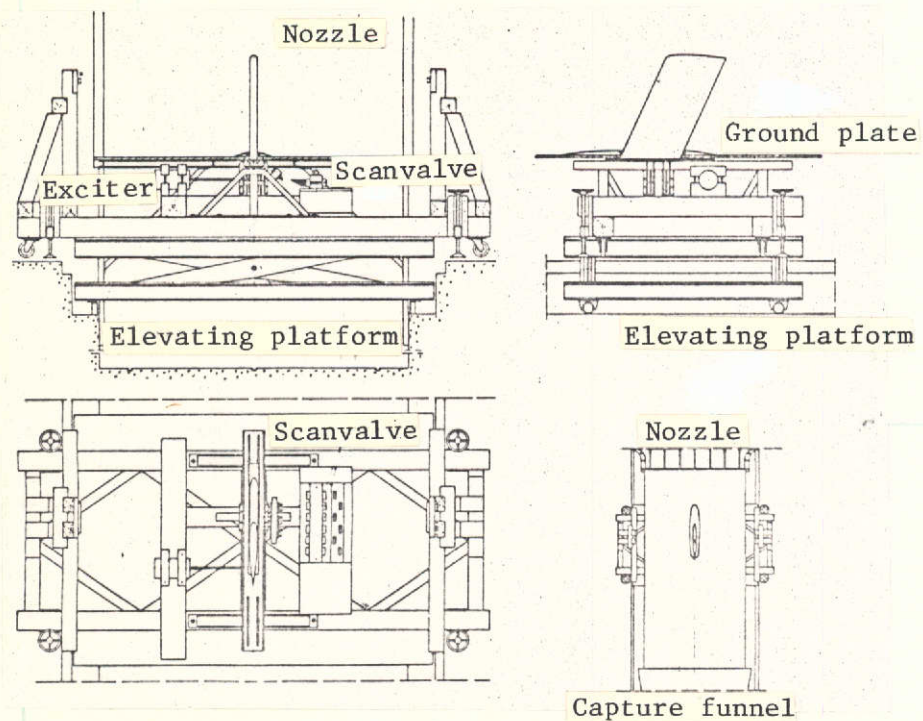


Figure 1. Test stand in the test section of the 3 m wind tunnel.

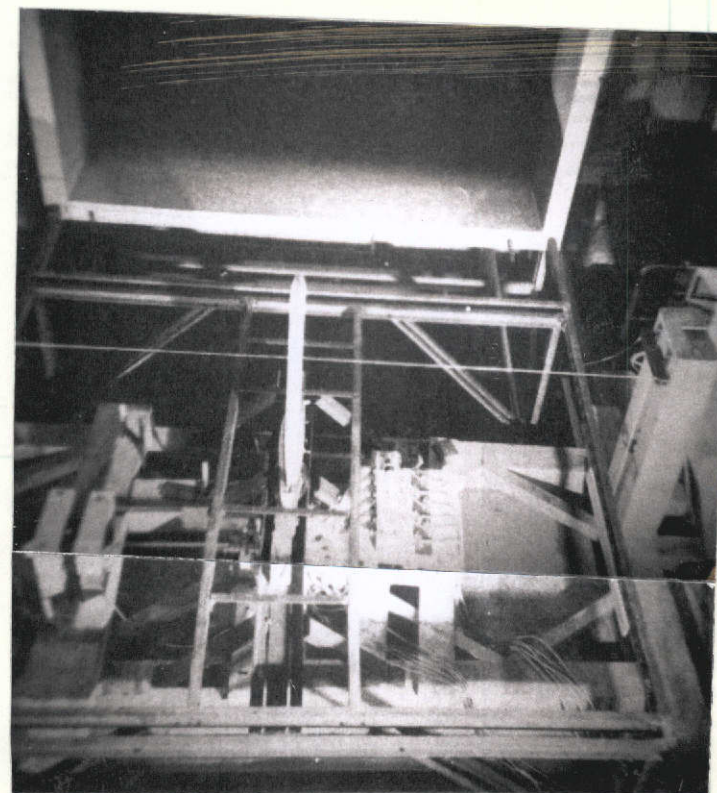


Figure 2. Configuration of test stand between the support for the wind tunnel plate.

The thin profile rods were attached to two wooden blocks outside of the wind flow (Figure 1). The profile rods were used to support the model along the axis of rotation.

/15

4. Models

A rectangular wing and a sweptback wing with a sweepback of 25° was investigated as shown in Figures 3 and 4. Except for the sweepback, these models have the same dimensions as shown in Figures 5 and 6. Both have the NACA 0012 profile. Later on, they were fitted with a full-length rudder amounting to 30% of the wing chord $l = 0.6$ m. The elevation adjustment of the test stand was selected for both models so that aspect ratios of $A = 3.1$ and 2.5 resulted for the half-spans $s = 0.94$ and 0.74 m and for semiwing areas of $F/2 = 0.564$ and 0.444 m².

The models each consist of two halves and were manufactured from glass fiber reinforced polyester resin. A negative mold was made of plaster in which the external skin resin was cast while inserting glass fiber mats. After the outer skin had become rigid, the longitudinal and transverse ribs were glued in, as shown in Figure 7. There are 140 pressure taps in the same configuration in both halves. A 40 mm long brass tube with an internal diameter of 1.6 mm was glued into the holes, which was connected to a 2 m long PVC hose. All of the lines had to be made of similar materials in order to achieve identical dynamic resistance behavior. The hoses were led out along the lower side of the models and connected to six switching devices (scanivalves), Figure 8. The external pressure measurement capsule is switched behind the scanivalves.

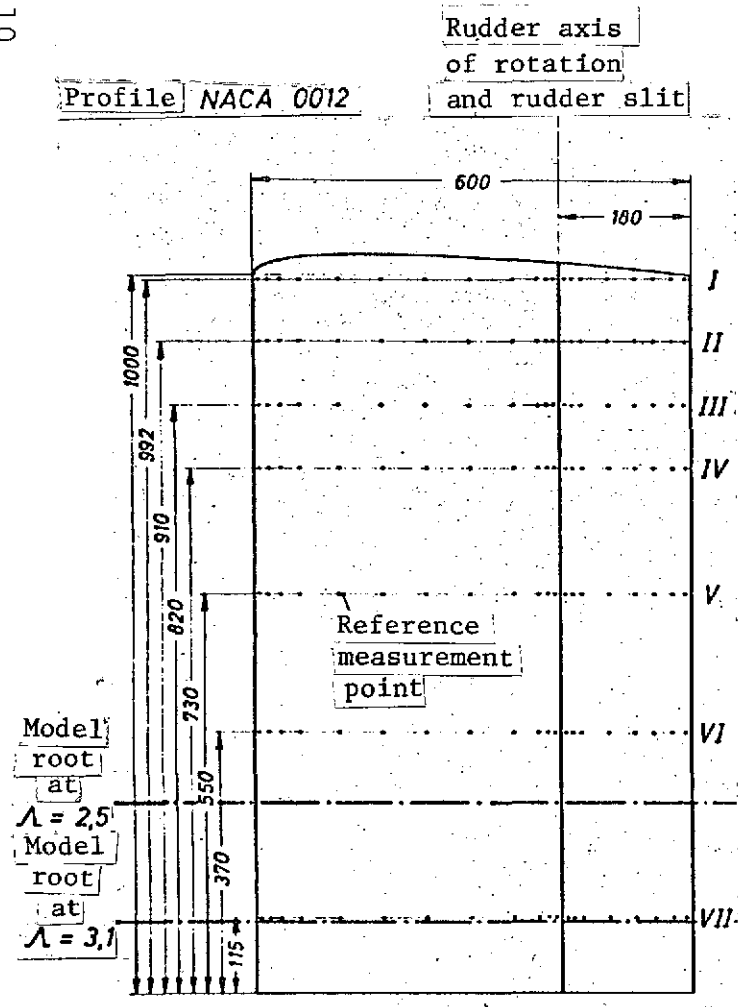


Figure 3. Rectangular wing with pressure measurement locations.

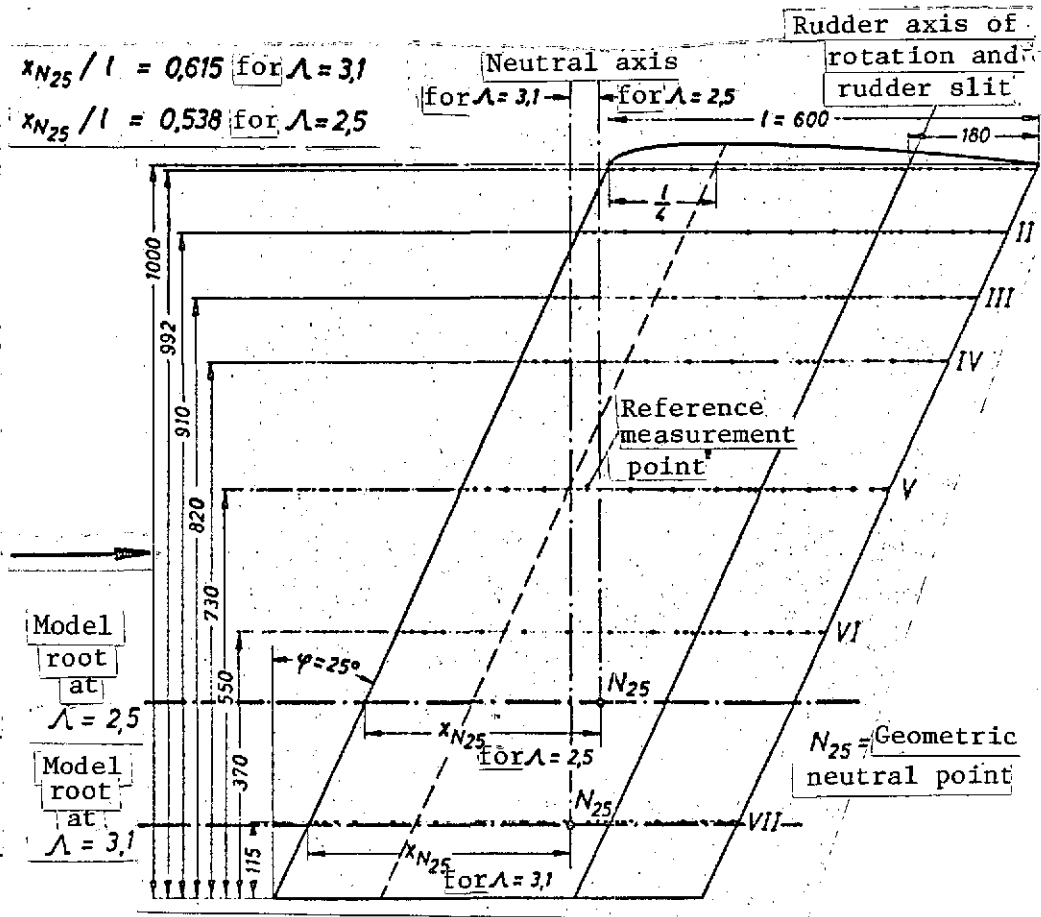


Figure 4. Sweptback wing with pressure measurement points.

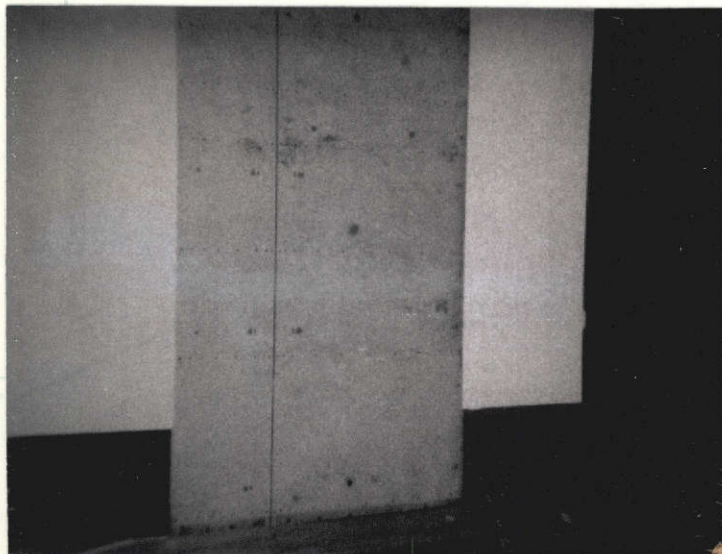


Figure 5. Rectangular wing and rudder in test section.

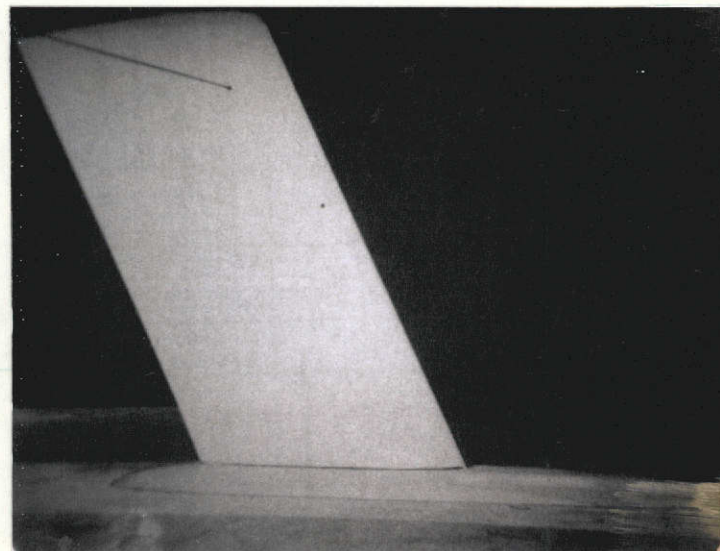


Figure 6. Sweptback wing in test section.

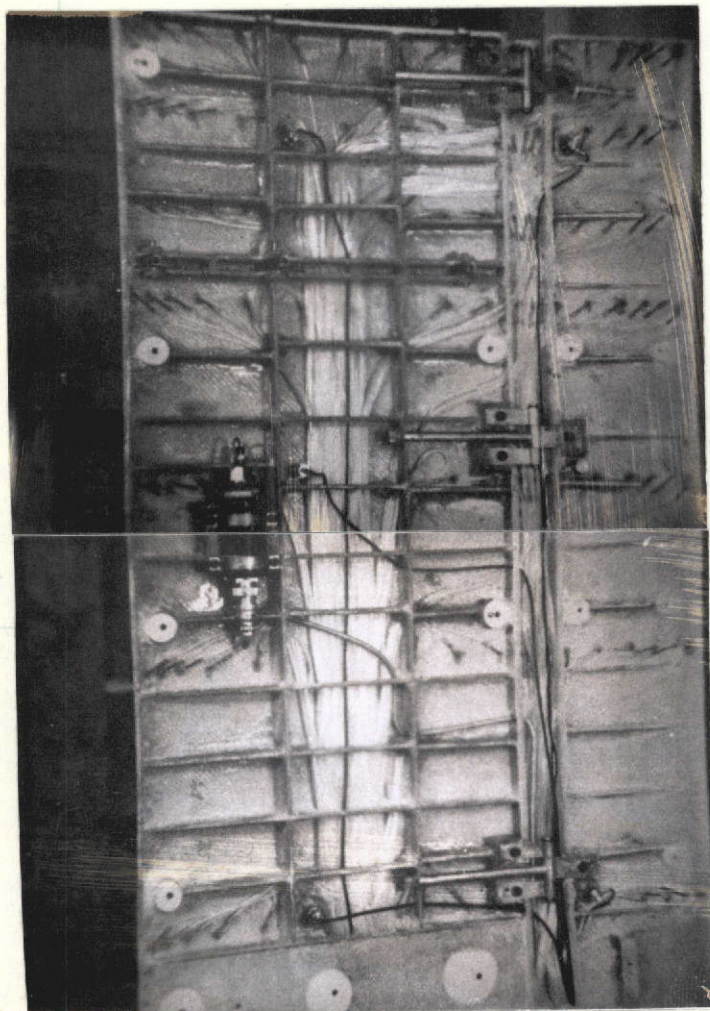


Figure 7. One-half of rectangular wing with installed pressure measurement capsule.

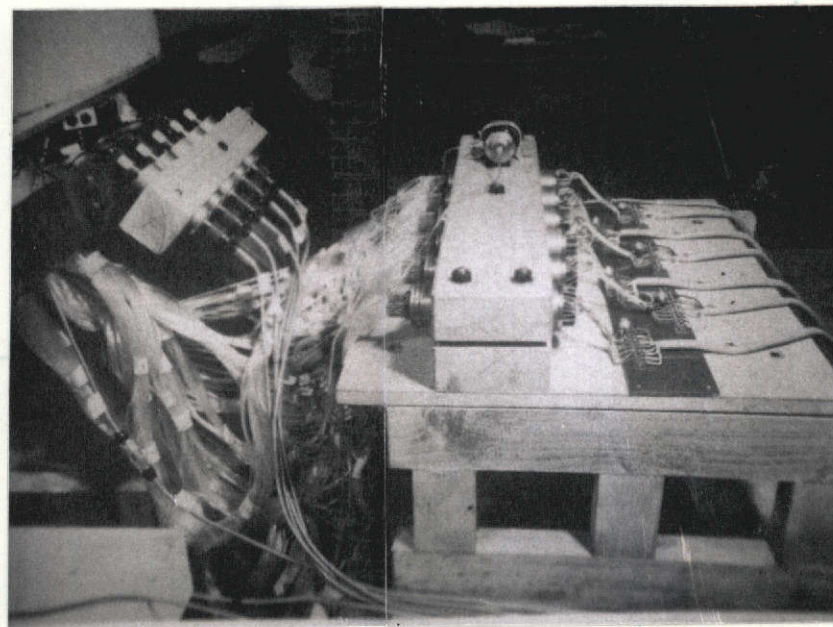


Figure 8. Stepping switch with hose connections, external pressure measurement capsule, and cathode followers.

The internal pressure measurement capsule is located inside the model which is used for calibrating the reference line (Figure 7). In addition, there are six acceleration transducers in the model with which it is possible to check the oscillation shape. Figure 8 shows the cathode follower switched behind the acceleration transducers.

/21

Both model halves are connected in many places by numerous pass pins and screws and are attached along the lower side to a metal track. The torsion spring is clamped to this track.

We measured rotational oscillations around three different rotation axes for the rectangular wing. We used two rotation axes for the sweptback wing. In addition, we have the rudder rotational oscillations around the rudder leading edge for both models, as well as simultaneous fin and rudder rotational oscillations for the rectangular wing. In this way, we were able to investigate eight half wings with a total of 16 different oscillation states using only two models, as shown in Figures 9a and b.

5. Electronic Measurement Techniques

The following quantities were measured:

1. pressure distribution over the model by the external pressure measurement capsule using 280 lines;
2. pressure at the control tap by the pressure measurement capsule installed in the wing;
3. amplitudes of the model of six installed accelerometer transducers; and

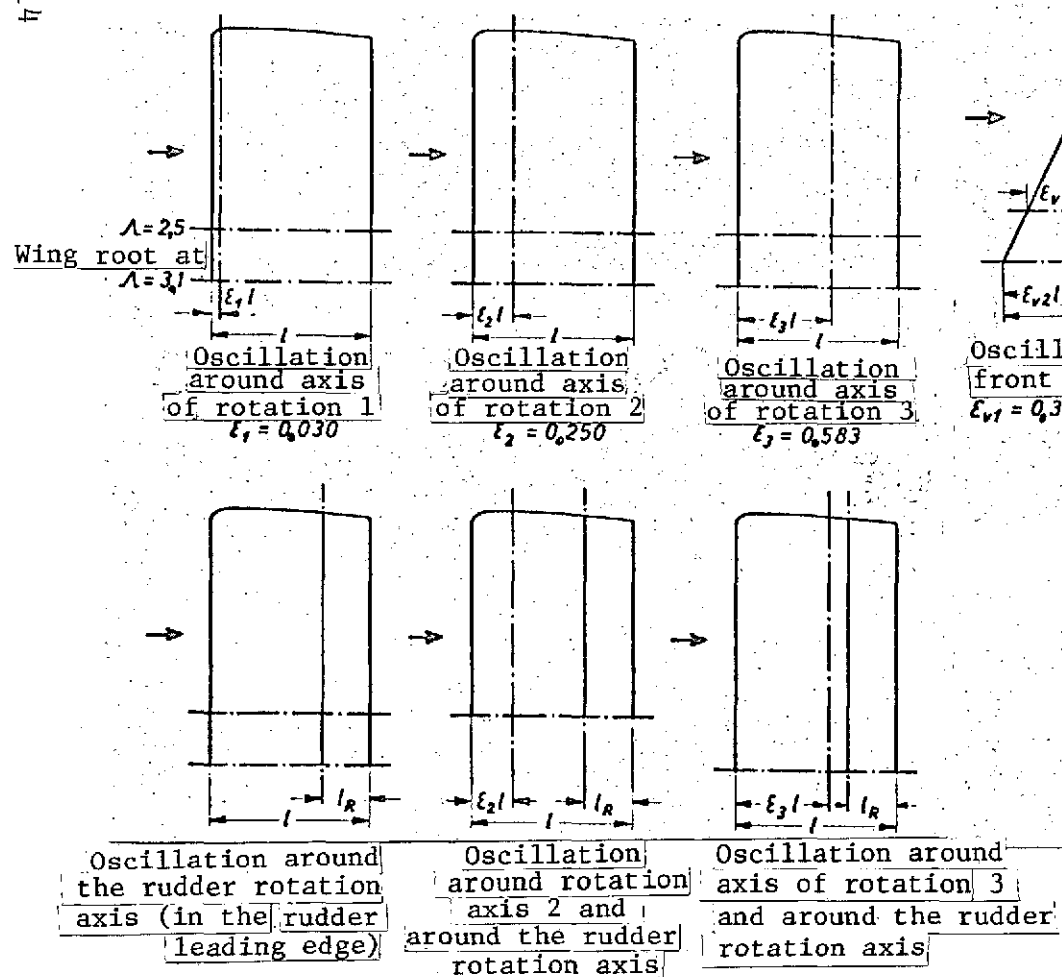


Figure 9a. Investigated oscillation shapes on the rectangular wing
 $l = 0.600$ m; $l_R = 0.180$ m.

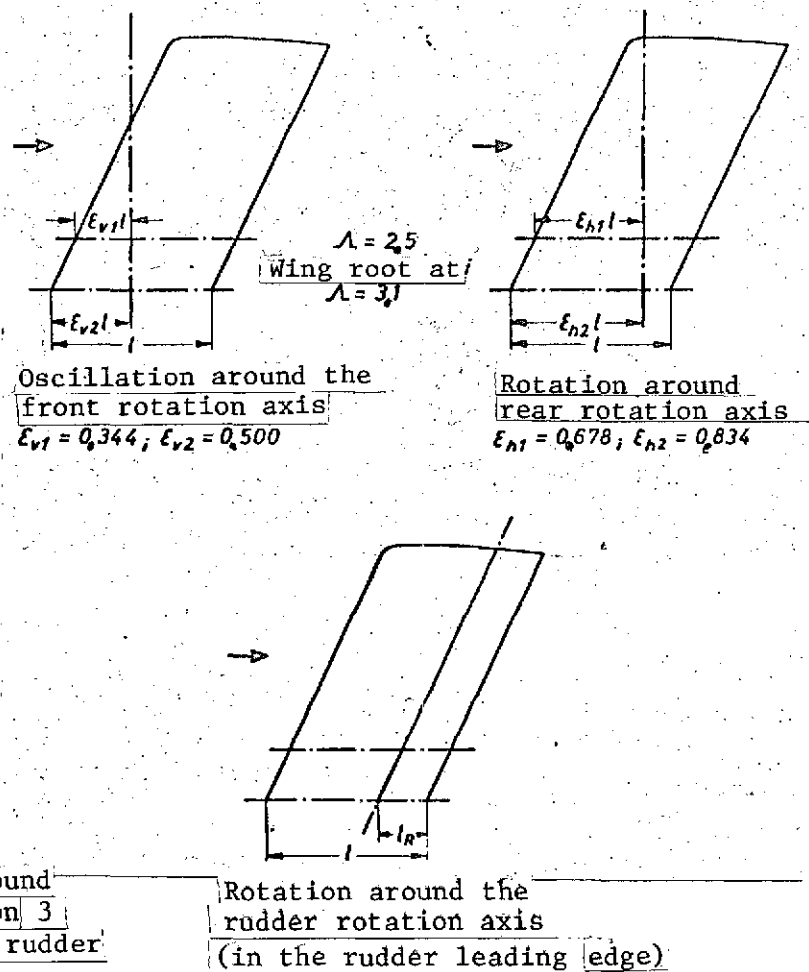


Figure 9b. Investigated oscillation shapes for the sweptback wing
 $l = 0.600$ m; $l_R = 0.180$ m.

4. amplitude at the model track or at the rudder by the electrodynamic velocity transducer with respect to the foundation.

Since about 300 measurement variables are obtained for each pressure distribution measurement (150 measurement values decomposed into real and imaginary parts), the measurement sequence was automated. The switching for this was performed by a control unit. The control unit directs the signals of the measurement transducers through a switch to the recording part of the apparatus; first these are directed to the vector component measurement device. This device performs a harmonic analysis by determining the coefficients /24

$$\begin{aligned} a_1 &= \frac{1}{2\pi} \int_0^{2\pi} f(t) \cos \omega t d(\omega t) \\ b_1 &= \frac{1}{2\pi} \int_0^{2\pi} f(t) \sin \omega t d(\omega t) \end{aligned} \quad (1)$$

of harmonic analysis of the signal $f(t)$. In the theory of harmonic oscillations, one usually considers the coefficients a_1 and b_1 as real and imaginary parts of the complex amplitude. The conversion into digital quantities is done by means of an integrating digital voltmeter to which is connected a printer through a code converter. The printer prints out the real part and the imaginary part in sequence. At the same time, the digital variables are transferred to punched cards using a punch. In order to eliminate disturbances caused by turbulence and slower fluctuations in the wind velocity as much as possible, the measurement time or integration time was extended to six seconds for each component.

The switching process of the control unit is triggered by an end of print pulse of the printer, which transmits the signal after each measurement of the imaginary part. The control unit then either switches to another measurement instrument or switches the scanivalves. The position of the six scanivalves can be controlled through lamps at the control unit. Since the printer has a counter, it is also possible to determine at any time by how much the measurement process has advanced within the recording process.

The accelerometer transducers operate according to the piezo electric principle. Their signals are amplified, integrated twice, and then connected to the recording part by the control unit.

An additional amplitude measurement is done by a velocity recorder, which has a pickoff on a boom on the model track. This recorder produces the required two reference voltages for the vector component measurement device and uses a four component filter.

/25

The measurement sequence is the following:

The characteristic data of a measurement sequence, the amplitude, and the oscillation frequency, are input manually to the printer. Then the control unit is turned on which takes over the entire measurement sequence. The following sequence of measured value transducers is maintained: acceleration transducer, installed pressure measurement capsule, and central pressure measurement capsule (140 times at $\Lambda = 3.1$; 120 times at $\Lambda = 2.5$). At the conclusion of the measurement series, the path amplitudes and the installed pressure measurement capsule are controlled.

The circuit of the measurement apparatus is shown in Figure 10. The structure of the device is shown in Figure 11. The development of the apparatus is discussed in detail in [33], especially the control unit.

6. Theories Used in the Comparison

6.1. Preliminary Remarks

The measurements in the 3 m wind tunnel of the AVA were carried out with the purpose of comparing the results with those of linearized theory of oscillating lifting surfaces with several simplifying assumptions. The term "lifting surface" means that the influence of profile thickness is ignored (infinitesimally thin profile).

The first of these assumptions is the assumption of an incompressible liquid. Since the measurements are carried out at Mach numbers $Ma \leq 0.15$, and since the relative density changes due to the compressibility influence are $\Delta\rho/\rho \approx Ma^2/2$, this simplification is justified.

One important condition for the theoretical solutions in the subsonic range are the so-called edge conditions at the edges of the lifting surface: integrability of the pressure at the edges and fixing of the geometric location of the downwind on the lifting surface. Using this latter condition, the influence of the friction boundary layer is considered phenomenologically. Usually, according to Kutta, it is assumed that (smooth) departure occurs at the trailing edge, and this assumption is also used in the following. However, it is not the only possible assumption. One can assume an oscillating separation point and, in this way, avoid the deviations between the theory

/28

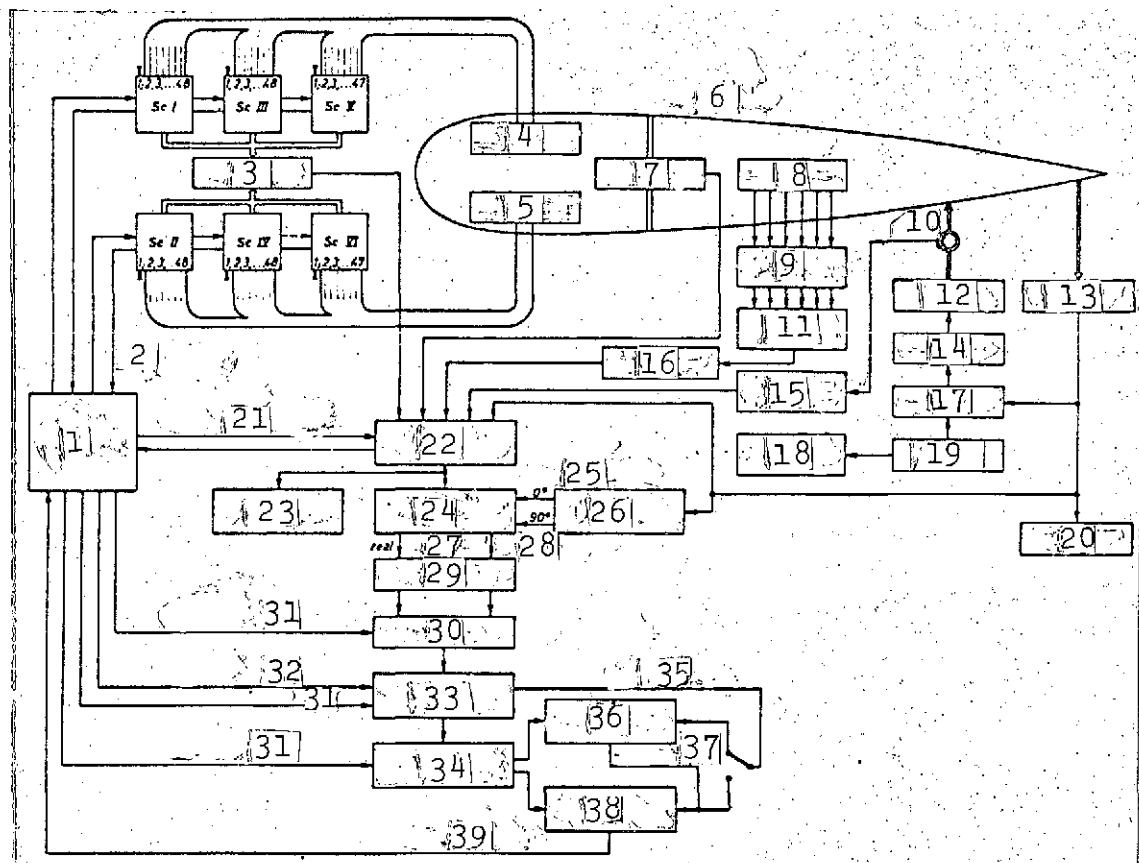


Figure 10. Switching of measurement apparatus.

1- control unit; 2- test and switch line; 3- external pressure measurement capsule; 4- topside: 140 pressure taps; 5- lower side: 140 pressure taps; 6- reference line; 7- internal pressure measurement capsule; 8- 6 accelerometer transducers; 9- 6 cathode followers; 10- strain gauges; 11- switch; 12- electrodynamic exciter; 13- velocity transducer; 14- power amplifier; 15- carrier frequency measurement amplifier; 16- integration amplifier; 17- control amplifier; 18- frequency counter; 19- frequency generator; 20- amplitude display; 21- test and switching line; 22- measurement variable switch; 23- oscillograph; 24- vector component voltmeter; 25- reference voltages; 26- four-phase filter; 27- outputs; 28- imaginary; 29- two separation amplifiers; 30- switch; 31- switch command; 32- measurement command; 33- integrating digital voltmeter; 34- code converter for printer and punch; 35- recording command; 36- punched card punch; 37- punching pulse; 38- digital printer; 39- print pulse.

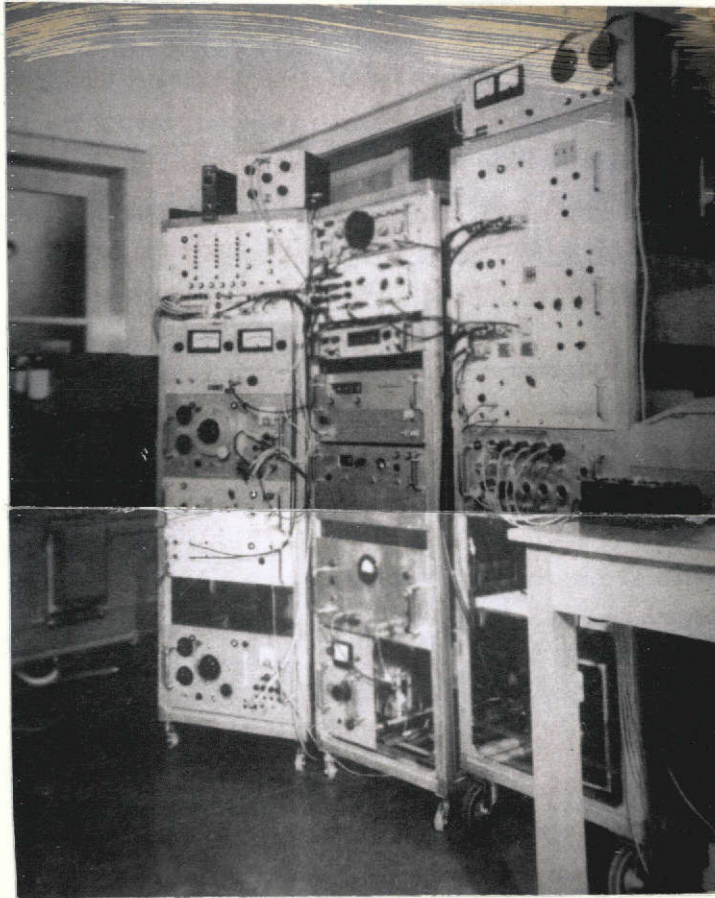


Figure 11. Arrangement of measurement instruments.

and the measurements. In the following, we will not make use of this interesting possibility. It will be considered in future investigations.

For very large wing aspect ratios and (or) very fast oscillations, the flow processes over a wing section in the flow direction depend only slightly on those of an adjacent section, if the adjacent wing sections oscillate with about the same amplitude. One can then approximately assume an independent two-dimensional flow in each wing section. This is a so-called strip theory, which was widely used for flutter calculations in aircraft wings. In the following, we will also consider it as a comparison.

Since large electronic computers can be used, it is possible to calculate sufficiently accurate approximate solutions of the integral equation of the general (three-dimensional) unsteady lifting surface theory (see Section 6.3). Such solutions may be considered for wings of small to average aspect ratios and they will also be used in comparisons with measurements in the following.

For lifting surfaces with large aspect ratios, the double integral calculation of the general lifting surface theory can be approximately reduced to a simple integral equation and, therefore, to a lifting line method (see Section 6.4). In the final result, only the vortex drag function T must be replaced in the strip theory mentioned above by a function which depends on the coordinate y and the oscillation shape of the wing. This theory is also used as a comparison.

/29

6.2. Two-Dimensional Theory

6.2.1. Integral representation of pressure

The two-dimensional theory has been discussed in many magazines and textbooks. We should especially like to mention the basic work of H. G. Kuessner and L. Schwarz [7] and the table monograph of H. G. Kuessner and H. Goellnitz [14].

The two-dimensional theory has led to good results for the large aspect ratio wing. Since we investigated wings with small side ratios ($\Lambda = 3.1$ and 2.5) in our measurements, we should expect considerable deviations. Nevertheless, the two-dimensional theory is of interest because it makes clear what improvements must be made to the large aspect ratio theory to be discussed below.

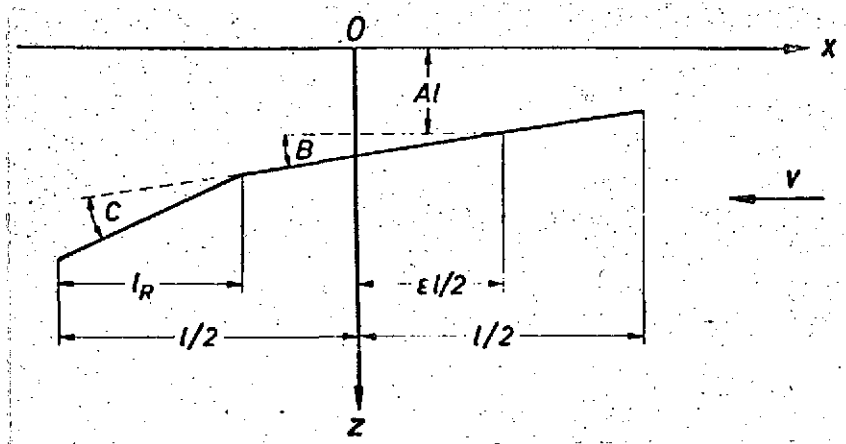


Figure 12. Deflection of segment profile,

We will use the coordinate system according to the aerodynamic standard 9300 (Figure 12). The positive x axis points in the direction of flight, that is, against the incident flow direction, and the positive z axis points downwards.*

We will first consider a segment profile with the half chord c . We will introduce elliptical coordinates according to:

$$\left. \begin{aligned} x &= c \cosh u \cos \theta & ; & & 0 \leq u < \infty \\ z &= c \sinh u \sin \theta & ; & & -\pi < \theta \leq \pi \end{aligned} \right\} \quad (2)$$

We have $u = 0$ along the segment profile. Along the leading edge, $\theta = 0$ holds and we have $\theta = \pi$ at the trailing edge. In addition, we assume that the reduced frequency is /31

$$\omega^* = \frac{\omega c}{V} \quad (3)$$

We assume that the segment profile carries out the oscillation motion $\zeta(x, t)$ and that $u = 0$, and that the downwind is

*In [9], the x axis is the reverse of this.

$$w(x, 0, t) = \left(\frac{\partial}{\partial t} - V \frac{\partial}{\partial x} \right) \zeta(x, t) = V \bar{w}(\theta) \exp \omega t. \quad (4)$$

and that there is the pressure jump

$$\Delta p = \lim_{z \rightarrow +0} p(x, z, t) - \lim_{z \rightarrow -0} p(x, z, t) = \rho V^2 \pi(\theta) \exp \omega t. \quad (5)$$

The pressure jump defined in Equation (5) is, therefore, the normal force per area unit, which the oscillating lifting surface exercises on the liquid in the positive z direction. This definition is appropriate in aeroelasticity and is usually used.

Using the variables used above, according to H. G. Kuessner [8, 13], we obtain the following integral representation for the reduced pressure jump π at the lifting surface $u = 0$, which satisfies the Kutta condition:

$$\begin{aligned} \pi(\theta) = & -\frac{4}{\pi} \int_0^\pi \bar{w}(\theta') \sin \theta' d\theta' \cdot \left\{ \left(\omega^* - \frac{1}{\sin \theta'} \frac{\partial}{\partial \theta'} \right) G(0, \theta, \theta') \right. \\ & \left. + G_{\theta'}(0, \theta, 0) [G_\theta(0, \pi, \theta') \pi(\omega^*) - G_\theta(0, 0, \theta')] \right\} \end{aligned} \quad (6)$$

where

$$\pi(\omega^*) = \frac{\int_0^\infty \exp(-\omega^* \cosh u) G_{\theta, \theta'}(u, \pi, 0) du}{\int_0^\infty \exp(-\omega^* \cosh u) G_{\theta, \theta'}(u, 0, 0) du} \quad (7)$$

For incompressible flow, the Green function becomes

$$G(u, \theta, \theta') = -\frac{1}{4} \ln \frac{\cosh u - \cos(\theta + \theta')}{\cosh u - \cos(\theta - \theta')} \quad (8)$$

and the vortex entrainment function

$$T(\omega^*) = - \frac{K_0(\omega^*) - K_1(\omega^*)}{K_0(\omega^*) + K_1(\omega^*)} \quad (9)$$

K_0 , K_1 are modified Hankel cylinder functions.

The reduced pressure jump Π is found from the integral equation (6), and from Equation (39), it is seen to be constant everywhere for constant and positive downwind.

6.2.2. Wing rotation

For wing rotational oscillations around an arbitrary rotation axis which is specified by $x_d = \epsilon c$, from Equations (4) through (8) and with

$$\zeta(x, t) = B(\epsilon c - x) \exp \omega t \quad (9a)$$

we obtain the following pressure distribution in the chord direction:

$$\begin{aligned} \Delta p(\theta, B) &= \rho V^2 B T_B(\theta) \exp \omega t \\ &= \rho V^2 B \left[\left\{ (1 + T(\omega^*)) \left(1 + \frac{\omega^*}{2} + \omega^* \epsilon(y) \right) - \omega^* \right\} \operatorname{ctg} \frac{\theta}{2} \right. \\ &\quad \left. + (2 \omega^{*2} \epsilon(y) + 4 \omega^*) \sin \theta - \omega^{*2} \sin \theta \cos \theta \right] \exp \omega t \end{aligned} \quad (10)$$

In Equation (10), $\epsilon(y)$ is the distance of the rotation axis from the wing center, /33

$$\epsilon(y) = \frac{x_d - x_0(y)}{c} \quad (11)$$

By integrating Equation (10) over the entire wing chord, we obtain the following for the aerodynamic force amplitude along the strip of width dy

$$dL = \rho V^2 c dy B \cdot \pi k_b \quad (12)$$

and the following for the moment around the front neutral axis

$$dM = \rho V^2 c^2 dy B \cdot \pi m_b \quad (13)$$

the theoretical derivatives are

$$k_b = (1 + T(\omega^*)) \left(1 + \frac{\omega^*}{2} + \omega^* \epsilon(y)\right) + \omega^* + \omega^{*2} \epsilon(y) \quad (14)$$

and

$$m_b = \omega^* + \frac{1}{2} \omega^{*2} \epsilon(y) + \frac{1}{8} \omega^{*2} \quad (15)$$

For a rudder with the rudder leading edge

$$\cos \varphi = \frac{x_R(y) - x_0(y)}{c} \quad (16)$$

from Equation (10) if we integrate from the limit φ to π , we find the rudder aerodynamic force caused by wing rotation acting on the strip of width dy

$$dR = \rho V^2 c dy B \cdot \pi r_b \quad (17)$$

and the rudder moment around the rudder leading edge

$$dN = \rho V^2 c^2 dy B \cdot \pi n_b \quad (18)$$

with the derivatives

$$\begin{aligned} \pi r_b = & (1 + T(\omega^*)) \left(1 + \frac{\omega^*}{2} + \omega \epsilon(y)\right) \Phi_{31} + \omega^* \Phi_{32} \\ & + \epsilon(y) \omega^{*2} \left(\pi - \varphi + \frac{1}{2} \sin 2\varphi + \frac{\sin^3 \varphi}{3(y)}\right) \end{aligned} \quad (19)$$

and

$$\pi n_0 = (1 + T(\omega^*)) \left(1 + \frac{\omega^*}{2} + \omega^* \varepsilon(y)\right) \phi_8 + \frac{1}{2} \omega^* \phi_9 - \omega^{*2} \left\{ (\pi - \varphi) \left(\frac{1}{8} + \varepsilon(y) \cos \varphi\right) + \varepsilon(y) \sin \varphi (\cos^2 \varphi + \frac{2}{3} \sin^2 \varphi) + \sin \varphi \cos \varphi \left(\frac{1}{12} \sin^2 \varphi + \frac{1}{8}\right) \right\} \quad (20)$$

The auxiliary functions $\phi_n(\varphi)$ are shown in the appendix.

6.2.3. Rudder rotation

From Equations (4) to (8) in the case of rudder rotational oscillations around the rudder leading edge and with

$$\zeta(x, t) = C \varepsilon_R (x_R - x) \exp \omega t \quad \text{with } \varepsilon_R = \begin{cases} 0, & \text{when } x > x_R \\ 1, & \text{when } x < x_R \end{cases} \quad (20a)$$

we find the pressure distribution

$$\begin{aligned} \Delta p(\theta, C) &= \frac{1}{\pi} \rho V^2 C T_c(\theta) \exp \omega t \\ &= \frac{1}{\pi} \rho V^2 C \{ (1 + T(\omega^*)) T_{c1} + (1 + T(\omega^*)) \omega^* T_{c2} \\ &\quad + T_{c3} + \omega^* T_{c4} + \omega^{*2} T_{c5} \} \exp \omega t \end{aligned} \quad (21)$$

the Π_{cn} are abbreviations

$$T_{c1} = \phi_1 \operatorname{ctg} \frac{\theta}{2} \quad (22)$$

$$T_{c2} = \frac{1}{2} \phi_2 \operatorname{ctg} \frac{\theta}{2} \quad (23)$$

$$T_{c3} = -2 \sin \varphi \operatorname{ctg} \frac{\theta}{2} + \ln \frac{1 - \cos(\theta + \varphi)}{1 - \cos(\theta - \varphi)} \quad (24)$$

$$\begin{aligned} T_{c4} = & -\dot{\Phi}_3 \operatorname{ctg} \frac{\theta}{2} + 4(\pi - \varphi) \sin \theta \\ & + 2(\cos \varphi - \cos \theta) \ln \frac{1 - \cos(\theta + \varphi)}{1 - \cos(\theta - \varphi)} \end{aligned} \quad (25)$$

$$\begin{aligned} T_{c5} = & [(\pi - \varphi) 2 \cos \varphi + \sin \varphi] \sin \theta - (\pi - \varphi) \sin \theta \cos \theta \\ & + (\cos \varphi - \cos \theta)^2 \frac{1}{2} \ln \frac{1 - \cos(\theta + \varphi)}{1 - \cos(\theta - \varphi)} \end{aligned} \quad (26)$$

When we integrate Equation (21) over the entire wing chord, we find the force amplitude acting on the strip of width dy

$$dL = \rho V^2 c \, dy \, C \cdot \pi k_c \quad (27)$$

and the following expression for the amplitude of the moment around the neutral axis

$$dM = \rho V^2 c^2 \, dy \, C \cdot \pi m_c \quad (28)$$

When we integrate over the rudder chord, we obtain the rudder aerodynamic force

$$dR = \rho V^2 c \, dy \, C \cdot \pi r_c \quad (29)$$

and the rudder moment around the rudder leading edge

$$dN = \rho V^2 c^2 \, dy \, C \cdot \pi n_c \quad (30)$$

The derivatives are

$$\pi k_c = (1 + T(\omega^*)) \left(\dot{\Phi}_1 + \frac{1}{2} \omega^* \dot{\Phi}_2 \right) + \omega^* \dot{\Phi}_3 + \frac{1}{2} \omega^{*2} \dot{\Phi}_4 \quad (31)$$

$$\pi m_c = \dot{\Phi}_5 + \frac{1}{2} \omega^* \dot{\Phi}_6 + \frac{1}{4} \omega^{*2} \dot{\Phi}_7 \quad (32)$$

$$\pi^2 r_c = (1 + T(\omega^*)) (\bar{\phi}_1 + \frac{1}{2} \omega^* \bar{\phi}_2) \bar{\phi}_{31} + \bar{\phi}_{35} + \omega^* \bar{\phi}_{36} + \frac{1}{2} \omega^{*2} \bar{\phi}_{37} \quad (33)$$

$$\pi^2 n_c = (1 + T(\omega^*)) (\bar{\phi}_1 + \frac{1}{2} \omega^* \bar{\phi}_2) \frac{1}{2} \bar{\phi}_8 + \bar{\phi}_{10} + \frac{1}{2} \omega^* \bar{\phi}_{11} + \frac{1}{2} \omega^{*2} \bar{\phi}_{12} \quad (34)$$

6.2.4. Simultaneous fin and rudder rotation

In the case of simultaneous fin and rudder rotational oscillations, usually there is a phase displacement between the two oscillation shapes. Since the resulting pressure distribution can be referred to the motion of the fin, we must write:

$$\Delta p(\theta, B, C) = \rho V^2 [B T_b(\theta) \exp \omega t + C T_c(\theta) \exp (\omega t + \delta)] \quad (35)$$

In Equation (35), δ is the phase angle between the two oscillation shapes. For the special case $\delta = \pi$, we find

$$\Delta p_1(\theta, B, C) = \rho V^2 [B T_b(\theta) - C T_c(\theta)] \exp \omega t \quad (36)$$

6.3. Three-Dimensional Lifting Surface Theory

/37

6.3.1. General integral equation

The general integral equation of the first kind for an oscillating lifting surface in a subsonic range was given by H. G. Kuessner [9] and also see [13]. Here we will restrict ourselves to a plane lifting surface in an incompressible flow. According to Equation (4), we assume that

$$w(x, y, 0, t) = V \bar{w}(x, y) \exp \omega t \quad (37)$$

is the given downwind on the lifting surface. According to Equation (5),

$$\Delta p = \lim_{z \rightarrow +0} p(x, y, z, t) - \lim_{z \rightarrow -0} p(x, y, z, t) = \rho V^2 T(x, y) \exp \omega t \quad (38)$$

is the pressure jump over the lifting surface and ω is the complex oscillation frequency. The physical meaning of this pressure jump was already discussed above. Then the integral equation of downwind at the lifting surface $z = 0$ is

$$\begin{aligned} \bar{w}(x, y) = & -\frac{1}{4\pi} \int_{-s}^s \int_{x_h(y')}^{x_v(y')} dx' dy' T(x', y') \exp \frac{\omega}{V} (x-x') \cdot \\ & \left\{ \frac{\omega}{V|y-y'|} \int_{\tau_0}^{\infty} \frac{\tau d\tau}{\sqrt{\tau^2+1}} \exp \left(\frac{\omega}{V} |y-y'| \tau \right) + \right. \\ & \left. \frac{(x'-x) \exp \left(\frac{\omega}{V} |y-y'| \tau_0 \right)}{(y-y')^2 \sqrt{(x'-x)^2 + (y-y')^2}} \right\} \end{aligned} \quad (39)$$

Here we have

$$\tau_0 = \frac{x' - x}{|y - y'|} \quad (40)$$

The integration over y' is divergent at the point $y' = y$ and must, therefore, be done in a special way, which has been developed by C. E. Watkins, H. L. Runyan, and D. S. Woolston [1], and others. /38

6.3.2. Solution methods

Based on [1], B. Laschka [3] selected a solution method which was already used by E. Truckenbrodt [35] and H. Multhopp [36] for calculating steady aerodynamic force distributions. The solution method uses the Glauert trial solution

$$\Pi(x, y) = \frac{1}{2} \sum_{r=0}^R a_r^*(y) h_r(x) \quad (41)$$

with the normal distribution

$$h_r(x) = \frac{T_r(1 - 2x) + T_{r+1}(1 - 2x)}{\pi \sqrt{(1-x)x}} \quad (42)$$

Here the functions $T_r(1 - 2x)$ are the Tchebyscheff polynomials of the first kind with the argument $1 - 2x$ with the three-dimensional coordinate

$$x = \frac{x_v(y) - x}{1} \quad (43)$$

We have the following relationship which involves the complex coefficients a_r^* and the complex lift and moment coefficients:

$$c_a(y) = \frac{2}{i} \int_{x_h}^{x_v} \Pi(x, y) dx = a_0^*(y) \quad (44)$$

$$\begin{aligned} c_m(y) &= -\frac{2}{i^2} \int_{x_h}^{x_v} \Pi(x, y) (x_m - x) dx \\ &= \frac{1}{4} [(4x_m - 1) a_0^*(y) + a_1^*(y)] \end{aligned} \quad (45)$$

The moment derivative refers to the x_m axis

$$x_m = \frac{x_v(y) - x_m(y)}{1} \quad (46)$$

The trial solution for $\Pi(x, y)$ must be introduced in Equation (39). The difficulty now consists of presenting the kernel function in such a way that a numerical solution method can be used. We cannot discuss the details of the method discussed in [3]. We will only give the results here, which produce two

complex equation systems for the symmetric and antisymmetric oscillation shapes.

For the symmetric oscillation shapes, the downwind at the lifting surface is expanded as follows:

$$\bar{w}(x_p, y_p) = \sum_{r=0}^R \sum_{n=1}^{\frac{m+1}{2}} \bar{a}_{rn} \bar{d}_{rn}^{vp} ; \quad \begin{matrix} v = 1, 2, \dots, \frac{m+1}{2} \\ p = 0, 1, \dots, R \end{matrix} \quad (47)$$

and for the antisymmetric oscillation shape, it is expanded in

$$\bar{w}(x_p, y_p) = \sum_{r=0}^R \sum_{n=1}^{\frac{m+1}{2}} \tilde{a}_{rn} \tilde{d}_{rn}^{vp} ; \quad \begin{matrix} v = 1, 2, \dots, \frac{m+1}{2} \\ p = 0, 1, \dots, R \end{matrix} \quad (48)$$

The downwind or the amplitudes are to be taken at the discrete point η and

$$\chi_p = \frac{x_v(\eta) - x_p(\eta)}{1} ; \quad p = 0, 1, \dots, R \quad (49)$$

where $\eta = y/s$. The \bar{a}_{rn} and \tilde{a}_{rn} , respectively, are the desired coefficients in the expansion equations (47) (48) at the discrete point $\eta = \eta_n$:

$$a_{rn} = a_r^*(\eta_n) \frac{1}{4s} \quad (50)$$

The coefficients d_{rn}^{vp} consist of universal quadrature constants and of influence functions, see [3]. The quadrature constants are tabulated. The influence functions must be calculated for each wing shape and reduced frequency. In the calculation, we select three points in the chord direction and ten stations in the span direction [40].

6.4. Theory of the Large Aspect Ratio Oscillating Lifting Surface

6.4.1. Integral equation of the large aspect ratio lifting surface

The integral equation for the theory of the large aspect ratio oscillating lifting surface was established by H. G. Kuessner [9], see also [10 — 13]. In the case of large aspect ratio lifting surfaces, the parameter given in Equation (40)

$$\tau_0 = \frac{x' - x}{|y - y'|} \quad (51)$$

is usually $\ll 1$ at most points of the lifting surface. Therefore, we may approximately set

$$\tau_0 \approx 0 \quad (52)$$

/41

In this case, the lower limit in the integral equation (39) becomes zero and the second term in the bracket drops out. Assuming the characteristic function

$$K(y) = \int_{x_h(y)}^{x_v(y)} \gamma(x, y) \exp\left(-\frac{\omega x}{V}\right) dx \quad (53)$$

and the special downwind distribution

$$w_1(x, y, 0, t) = V \bar{w}_1(y) \exp\left[\omega\left(t + \frac{x}{V}\right)\right] \quad (54)$$

we then find the following simplified integral equation for the characteristic function from Equation (39) by using partial integration

$$\bar{w}_1(y) \approx \bar{w}_1(y) \frac{K(y)}{K_e(y)} + \frac{1}{4\pi} \int_{-s}^s S\left(\frac{\omega}{V} |y - y'|\right) \frac{dK(y')}{dy'} \cdot \frac{dy'}{y - y'} \quad (55)$$

Here K_e is the characteristic function in the two-dimensional flow. The function S is defined and tabulated in [9, 12, and 15]. For $\omega = 0$, we have $K(y) = \Gamma(y)$ (circulation) and $S = 1$. Equation (55) then becomes the integral equation of the so-called Prandtl lifting line theory, which is also a lifting surface theory.

In order to be able to treat arbitrary downwind distributions using Equation (55) and not only those having the form (54), another approximation is required. From the given downwind w , we will subtract the downwind \bar{w}_1 according to Equation (54), which has just the right magnitude so that the characteristic functions for w and w_1 in two-dimensional flow coincide. The pressure produced by \bar{w}_1 is calculated according to Equation (55). The pressure, which is produced by the downwind difference, is calculated according to the two-dimensional theory. /42

As shown in [12], the approximation assumptions amount to replacing only the function $T(\omega^*)$ by the modified vortex entrainment function

$$T_1(\omega^*, y) = \frac{K(y)}{\pi c \bar{w}_1(y) [I_0(\omega^*) - I_1(\omega^*)]^2} \cdot \frac{I_0(\omega^*) + I_1(\omega^*)}{I_0(\omega^*) - I_1(\omega^*)} \quad (56)$$

in the two-dimensional solution [Equation (6)] mentioned above. I_0 and I_1 are the modified Bessel functions.

6.4.2. Solution methods

The characteristic function in the case of two-dimensional flow is

$$K_e(y) = \pi c I(\omega^*) \bar{w}(y) = \frac{2c \exp[-(\frac{\omega}{V} x_0(y))]}{\omega^* [K_0(\omega^*) + K_1(\omega^*)]} \cdot I(y) \quad (57)$$

for

$$J(y, B) = \pi B (\omega^* \epsilon(y) + \frac{\omega^*}{2} + 1) \quad (58)$$

for wing rotational oscillations around an arbitrary rotation axis and

$$J(y, C) = C (\phi_1 + \frac{\omega^*}{2} \phi_2) \quad (59)$$

for rudder rotation around the rudder leading edge.

In order to solve the integral equation (55), it is useful to use a harmonic trial solution. We set

$$y = s \cos \psi \quad (60)$$

$$K(y) = \sum_{n=1}^N \frac{k_n}{n} \sin n \psi \quad (61)$$

Then, the integral equation (55) finally becomes the algebraic equation

$$K_e(s \cos \psi) = \sum_{n=1}^N k_n \left\{ \frac{1}{n} \sin n \psi + \frac{\pi l}{4s} \cdot f(\omega^*) S_n(\Omega, \psi) \right\} \quad (62)$$

$S_n(\Omega, \psi)$ and $f(\omega^*)$ are auxiliary functions. The functions S_n have been calculated in [15] for $n = 1$ to 19: Ω is the reduced frequency referred to one-half of the span

$$\Omega = \frac{\omega s}{V} \quad (63)$$

In order to determine the desired coefficients k_n in Equation (62), it is necessary to substitute N discrete values $\psi = \psi_m$ so that we find a system of N linearized, inhomogeneous, and complex

equations for the coefficients k_n . Nine points $\cos \psi_m$ are selected for the calculation:

$$\cos \psi_m = 0; 0.3; 0.4; 0.5; 0.6; 0.7; 0.8; 0.9; 1.0 \quad (64)$$

For these stations, we calculate the modified function T_1 with which it is then possible to determine the pressure distribution at these sections. Since the model only has seven sections with pressure taps, it would have been sufficient to carry out the calculation for these seven sections. The determination of the global forces becomes more accurate the more stations $\cos \psi_m$ are used.

As already mentioned in Section 6.4.1, the solution for the large aspect ratio theory differs from the two-dimensional theory only because the functions $T(\omega^*)$ of the two-dimensional solution must be replaced by the modified functions $T_1(\omega^*, y)$ according to Equation (56). With this substitution, we can, therefore, apply the expression for the pressure distribution, for the aerodynamic forces, and moments of Section 6.2 in the theory of the oscillating large aspect ratio lifting surface. /44

The three theories mentioned were programmed for the IBM 7040 computer installation of the AVA. The author wishes to thank Mr. H. Triebstein and Mr. K. Lohmann for the programming work [40, 41].

7. Measurement Results

7.1. Oscillations in Quiet Air

Figures 13 and 14 give an example of a pressure distribution for oscillations in quiet air. These are rudder rotational oscillations of the sweptback wing [32]. In addition to the measured values, we also show the limiting case of the two-dimensional theory for $V = 0$ and, therefore, for $|\omega^*| = \infty$. From Equation (21), we obtain the following for this limiting case

$$\Delta p_0(\theta, C) = \rho |\omega|^2 c^2 C [\Pi_{c5}] \exp \omega t \quad (65)$$

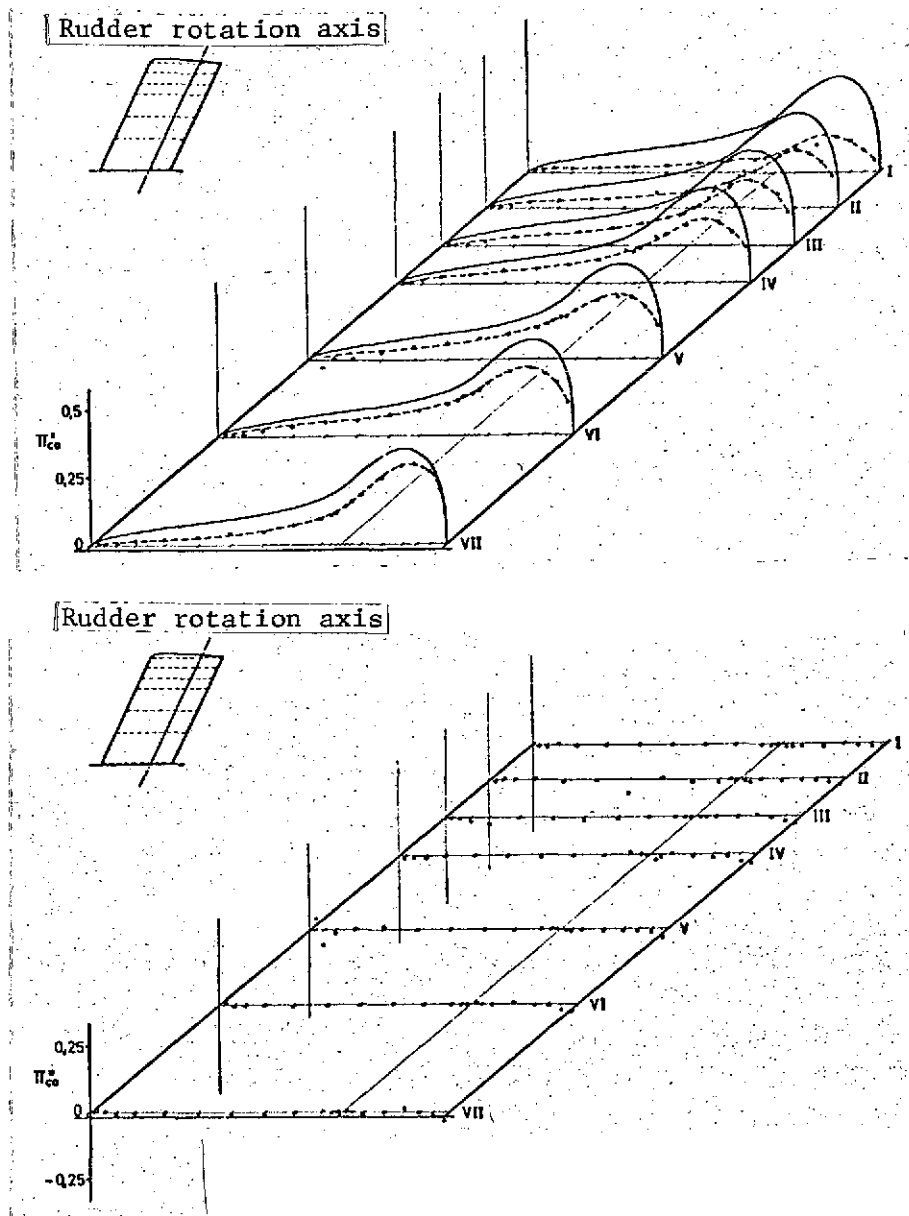
where Π_{c5} is given by Equation (26).

The following complex pressure derivative for the rudder rotational oscillations is defined at $V = 0$ for purposes of plotting:

$$\Pi_{c0} = \Pi'_{c0} + i \Pi''_{c0} = \frac{\Delta p_0(\theta, C)}{\rho |\omega|^2 c^2 C \exp \omega t} \quad (66)$$

In Equation (65), we have $\Pi''_{c0} = 0$, i.e., the oscillating air mass is in phase with the motion, according to the theory.

In spite of the very low pressures (order of one-tenth of a millimeter of water column), the scatter in the measured value is small. The requirement for identical dynamic resistance behavior of the pressure lines is apparently satisfied for both models. If we consider the fact that the plane theory cannot consider the pressure equalization at the end of the wing, we can see that the measured values have the same tendency as the theoretical prediction. This is also true for the imaginary part, because the measured values are close to zero, whereas



Figures 13 and 14. Distribution of the oscillating air mass $\pi_{co} = \pi'_{co} + i\pi''_{co}$ for rudder rotational oscillations of the sweptback wing: $\Lambda = 3.1$; $\nu = 6$ Hz; -o- measurement; — two-dimensional theory.

they should be exactly equal to zero according to the theory. Additional examples for the pressure distributions for oscillations in quiet air are contained in [29 — 32].

7.2. Steady Flow

The boundary layer thickness along the wind tunnel plate is first determined in preliminary experiments. The height of the fuselage-like body which frames the model root (see, for example, Figure 6) is then selected so that it penetrates somewhat above the maximum boundary layer thickness. Outside of the boundary layer, the free jet had a great deal of turbulence and direction fluctuations in the vicinity of the plate, so that flow separation occurred at the lowest section in the vicinity of the nose of the model. Therefore, we did not consider the lowest section when integrating the pressure distribution over the wing area.

In order to also obtain the derivatives for the limiting case $\omega^* = 0$, i.e., steady flow, we measured the pressure distributions for various angles of attack α of the wings as well as for various deflection angles ξ of the rudders for retracted fin [37]. By integrating the steady pressure distributions over the wing area, we were able to determine the lift and moment coefficients and, therefore, their increases with angle of attack α for the various configurations. The lift and moment increases correspond to the real parts of the unsteady derivatives for the limiting case $\omega^* = 0$, for example

$$\left. \frac{dc_A}{d\alpha} = \lim_{\omega^* \rightarrow 0} k_B = \pi k'_B \right| \quad (67)$$

$$\left. \frac{dc_M}{d\alpha} = \lim_{\omega^* \rightarrow 0} m_B = \pi m'_B \right| \quad (67a)$$

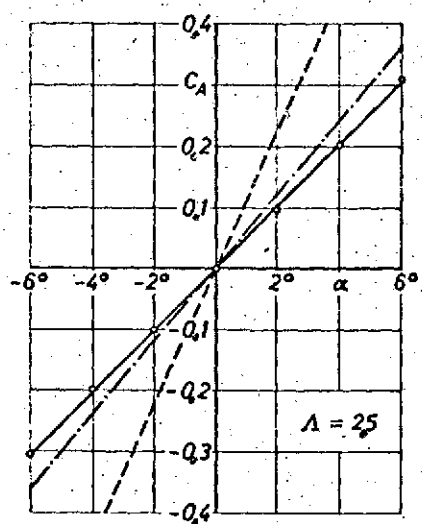
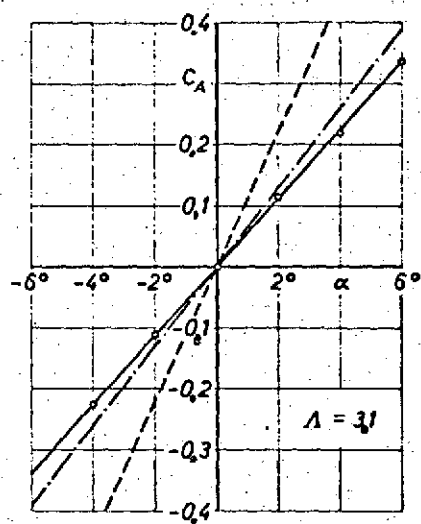
In Equations (67) and (67a), the quantities c_A and c_M are the total lift and total moment coefficients of the wing. The global aerodynamic force and moment derivatives for wing rotation, k_B and m_B , are formed as follows:

$$k_B = k'_B + i k''_B = \frac{1}{s} \int_0^s k_b(y) dy \quad (68)$$

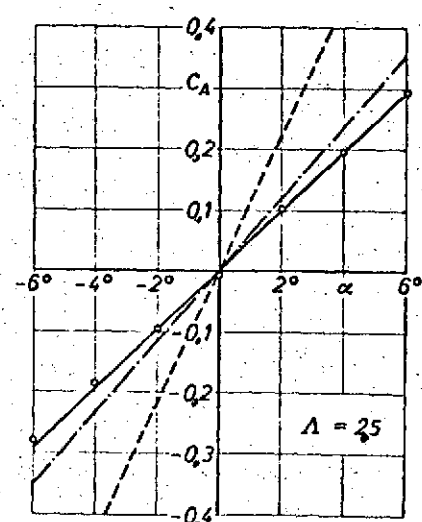
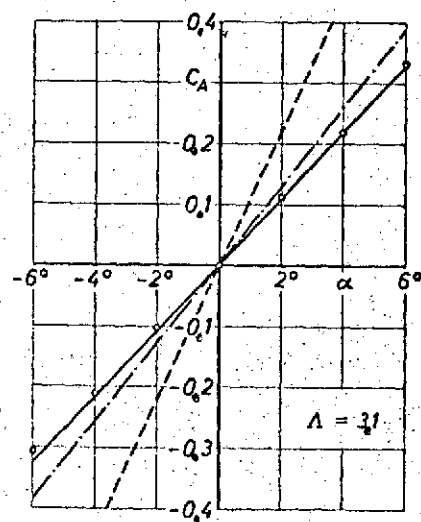
$$m_B = m'_B + i m''_B = \frac{1}{s} \int_0^s m_b(y) dy \quad (68a)$$

In Equations (67) and (67a), only the real part of the derivatives is contained, because the imaginary part must vanish for $\omega^* = 0$ according to definition.

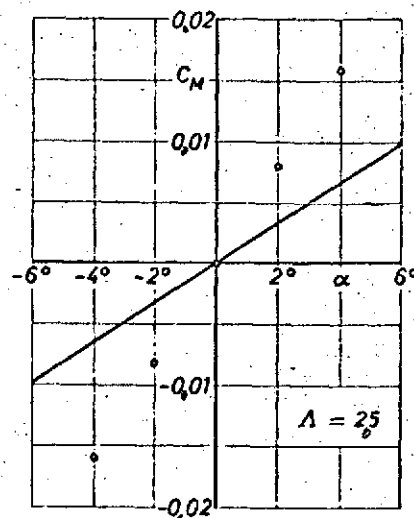
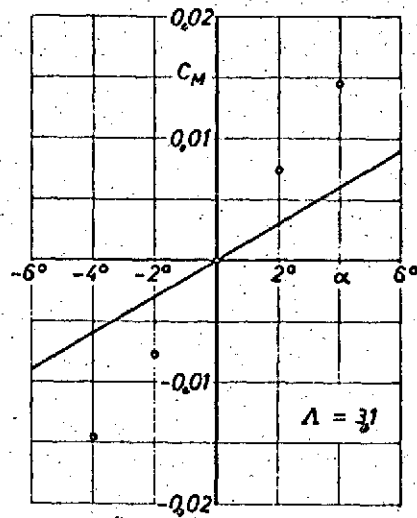
Figures 15 through 22 contain lift and moment coefficients of the investigated wings. The moments are referred to the neutral axis. In addition to the measured values, we also show the variations which are found from the three discussed unsteady aerodynamic force theories for the limiting case of steady flow. It can be seen that the lifting surface method, called the three-dimensional theory in the figures, produces an exceptional agreement for the lift coefficients, Figures 15 to 18. However, the agreement is not as good for the moment coefficients, Figures 19 to 22. Here the measured values are considerably above those of the theory. The deviation must be attributed to the influence of the finite thickness, which was not considered by the theory. The results presented here confirm earlier measurements of N. Scholz with rectangular wings of various aspect ratios [43]. Similarly large deviations can also be found in measurements under plane flow conditions [44].



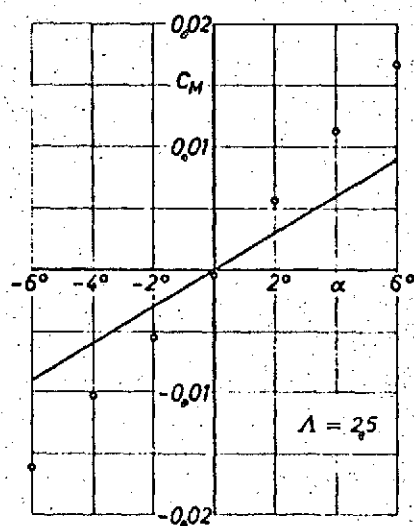
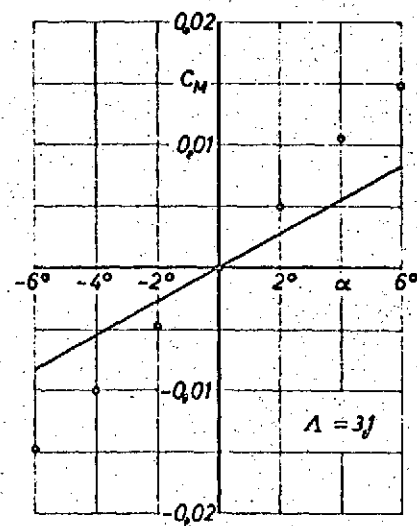
Figures 15 and 16. Lift coefficient values of rectangular wing.



Figures 17 and 18. Lift coefficient values of sweptback wing.
 o- measurement, profile NACA 0012; --- two-dimensional theory;
 -.- large aspect ratio theory; — three-dimensional theory.
 (all theories — flat plate).



Figures 19 and 20. Moment coefficient values of rectangular wing.



Figures 21 and 22. Moment coefficient values of sweptback wing.
o- measurement, profile NACA 0012; — three-dimensional theory, flat plate.

Tables 1a and b contain the numerical values of the increases or the derivatives, respectively. The table contains the measured values which have been corrected for the finite jet diameter of the wind tunnel. The corrections are very small. The measured values for rudder deflection are given in [37].

7.3. Oscillations in the Case of Incident Flow

751

7.3.1. Preliminary remark

The wind tunnel measurements with operating models were carried out for the reduced frequencies $|\omega^*| = 0.13$ to 0.76 . The variation of the reduced frequency was done by changing the oscillation frequency ν in the range between 3 and a maximum of 18 Hz at a constant stagnation pressure $q = 100$ mm WS and, therefore, constant Reynolds number $Re \approx 1.6 \cdot 10^6$. It was also done by reducing the stagnation pressure for a constant oscillation frequency $\nu = 6$ Hz. The lowest Reynolds number was $0.5 \cdot 10^6$. The oscillation amplitudes of the wings amounted to between 0.2 to 0.8 degrees. The rudder rotation oscillations had amplitudes of up to 1.6 degrees.

Dimensionless pressure derivatives were selected for plotting the unsteady pressure distributions, and for the wing rotation according to Equation (10), we use

$$\bar{T}_b = \bar{T}_b' + i \bar{T}_b'' = \frac{\Delta p(\theta, B)}{\rho V^2 B \exp \omega t} \quad (69)$$

whereas for the rudder rotation, according to Equation (21), we use

$$\bar{T}_c = \bar{T}_c' + i \bar{T}_c'' = \frac{\Delta p(\theta, C)}{\rho V^2 C \exp \omega t} \quad (70)$$

TABLE 1a. LIFT INCREASE $dc_A/d\alpha = \pi k'_B$ FOR WING AT ANGLE OF ATTACK.*

Wing	Measurement	Corrected measurement	Three-dimensional theory (lifting surface theory)	Large aspect ratio theory (lifting line theory)	Two-dimensional theory
Rectangular wing $\Lambda = 3.1$	3.18	3.23	3.21	3.70	$6.28 = 2\pi$
Rectangular wing $\Lambda = 2.5$	2.89	2.93	2.85	3.40	6.28
Sweptback wing $\Lambda = 3.1$	3.08	3.13	3.10	3.67	6.28
Sweptback wing $\Lambda = 2.5$	2.80	2.84	2.77	3.35	6.28

TABLE 1b. MOMENT INCREASE $dc_M/d\alpha = \pi m'_B$ OF WING AT ANGLE OF ATTACK.*

Wing	Measurement	Corrected measurement	Three-dimensional theory (lifting surface theory)	Large aspect ratio theory (lifting line theory)	Two-dimensional theory
Rectangular wing $\Lambda = 3.1$	0.209	0.212	0.086	0	0
Rectangular wing $\Lambda = 2.5$	0.230	0.233	0.094	0	0
Sweptback wing $\Lambda = 3.1$	0.146	0.148	0.078	0	0
Sweptback wing $\Lambda = 2.5$	0.160	0.162	0.084	0	0

*[Translator's Note: Commas in numbers indicate decimal points.]

In the case of simultaneous fin and rudder rotation, two amplitudes are involved. If the phase angle between the two oscillation shapes is $\delta = \pi$, then according to Equation (36) we find the following dimensionless and amplitude-dependent pressure coefficient

$$P = P' + i P'' = \frac{\Delta p_1(\theta, B, C)}{\rho V^2 \exp i \omega t} \quad (71)$$

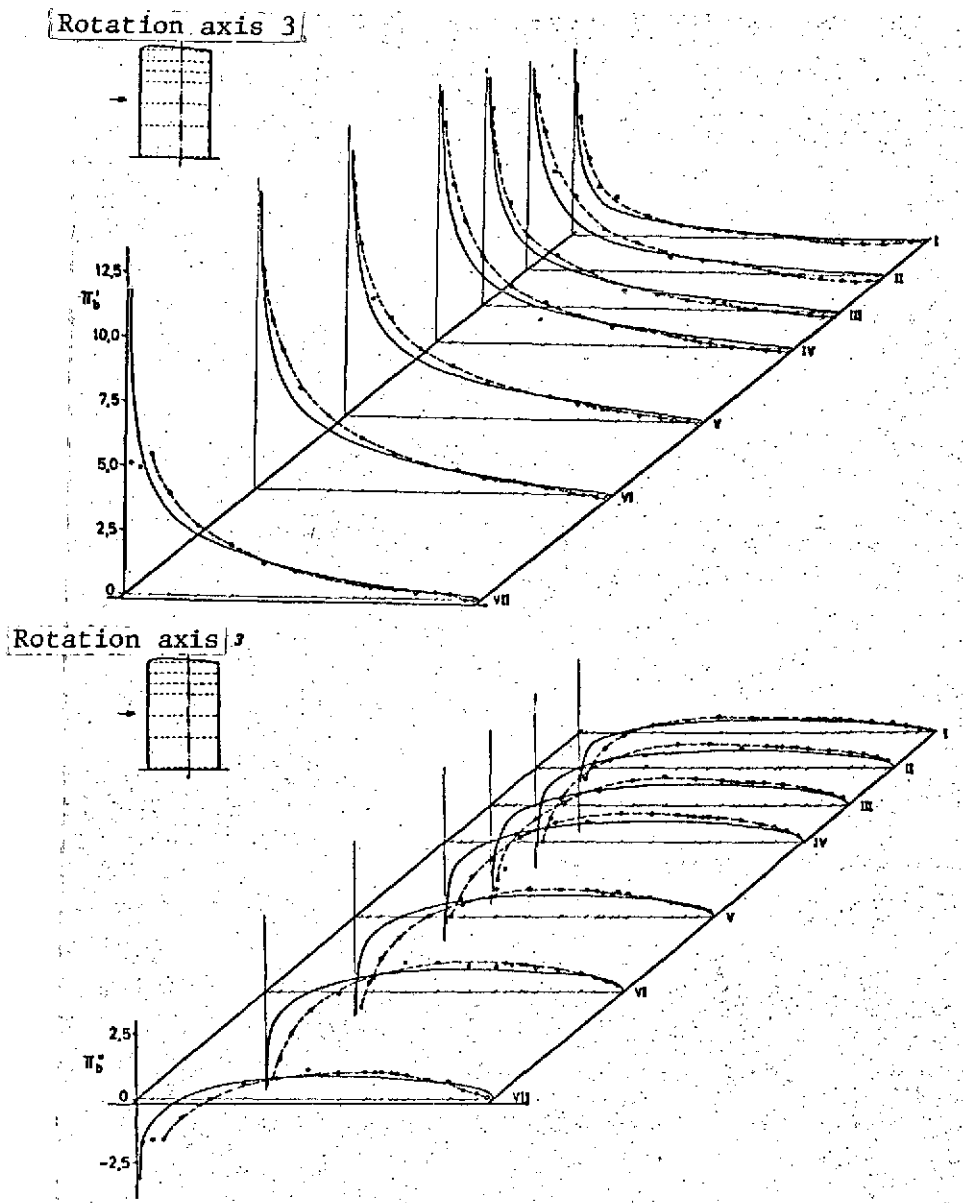
The measured local derivatives are found by integrating the measured pressure distributions at the seven (for the aspect ratio $\Lambda = 3.1$) or six (for $\Lambda = 2.5$) model sections (see Figures 3 and 4). The global derivatives are obtained by integrating the pressure distribution over the entire wing and rudder area. In order to distinguish the local derivatives, the global derivatives have large letters as subscripts, see Equation (68). /52

The local moment derivatives for wing pitch oscillations are referred to the $z/4$ line. The corresponding global derivatives refer to the neutral axis, that is, the axis through the geometric neutral point (see Figure 4). The wing and rudder moments are positive for a tail load.

We should like to remark, in conjunction with the following pressure distributions, that the measurement examples presented represent a relatively small selection of the results contained in [29 — 32]. A complete reproduction of them would go outside the scope of this report.

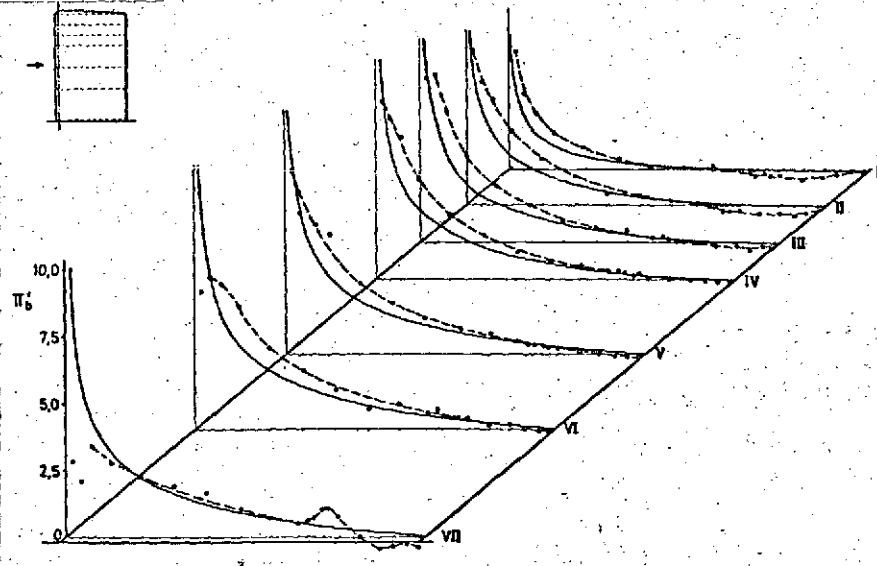
7.3.2. Wing rotation

Figures 23 to 28 show the three measured pressure distributions for harmonic rotational oscillations of the rectangular wing with a side ratio $\Lambda = 3.1$. The examples given are distinguished by the position of the rotation axis (see Figure 9a). The



Figures 23 and 24. Pressure distribution $\pi_b = \pi_b' + i\pi_b''$ over rectangular wing for rotational oscillations around axis 3; $\Lambda = 3.1$; $\nu = 8$ Hz; $|\omega^a| = 0.364$; $-o-$ measurement; \longrightarrow three-dimensional theory.

Rotation axis 1



Rotation axis 1

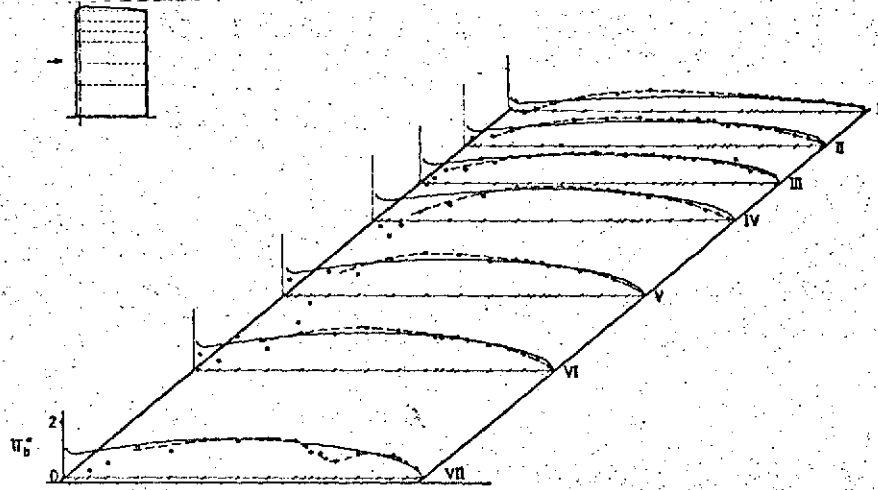
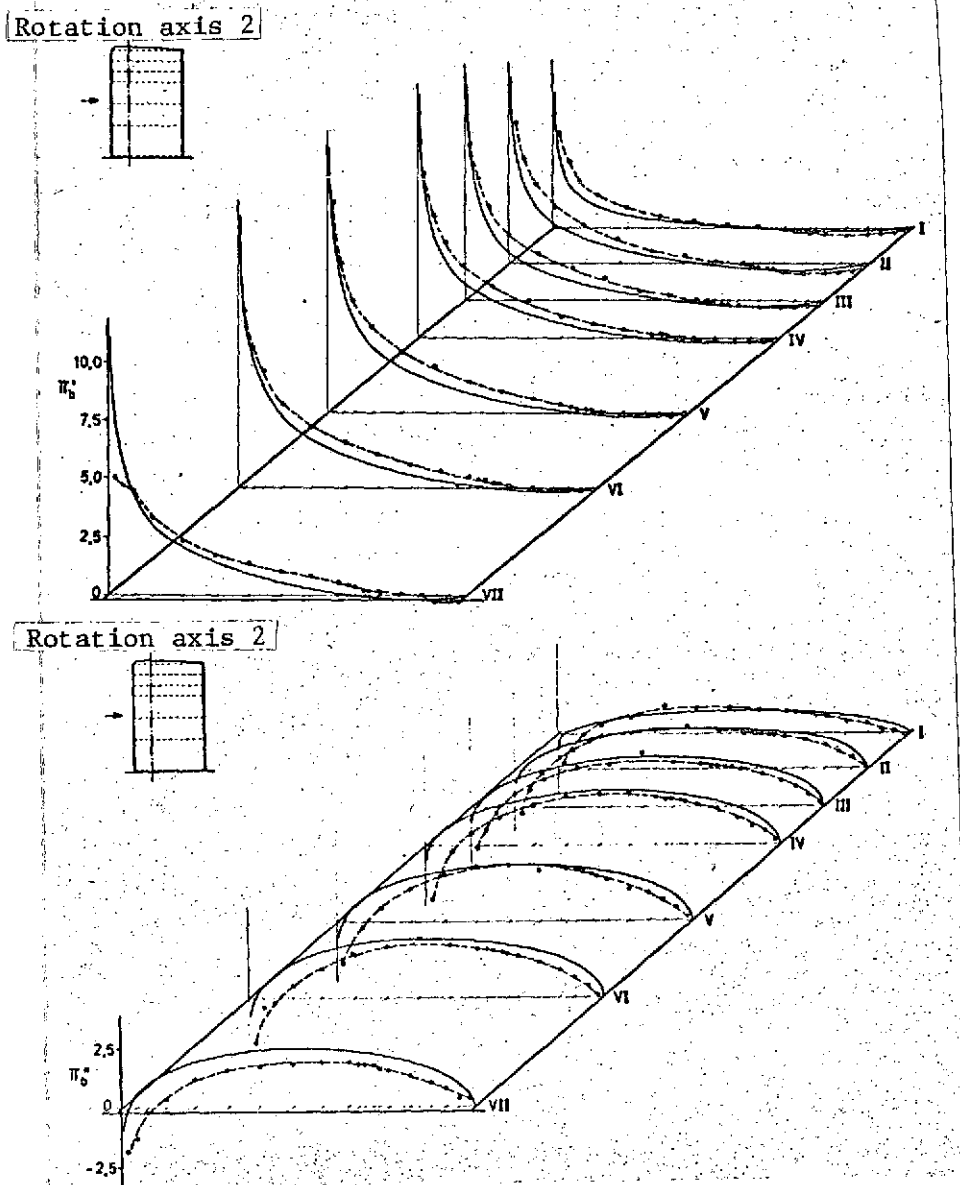


Figure 25 and 26. Pressure distribution $\pi_b = \pi'_b + i\pi''_b$ over rectangular wing for rotational oscillations around axis 1; $\Lambda = 3.1$; $\nu = 8$ Hz; $|\omega^*| = 0.364$; -o- measurement; — three-dimensional theory.



Figures 27 and 28. Pressure distribution $\pi_b = \pi_b' + i\pi_b''$ over rectangular wing for rotational oscillations around axis 2; $\bar{A} = 3.1$; $\nu = 16.06 \text{ Hz}$; $|\omega^*| = 0.744$; -o- measurement; — three-dimensional theory.

results of the lifting surface theory according to [3] are given in addition to the measured values, and they are referred to as the three-dimensional theory.

As already mentioned above, there was partial flow separation in the vicinity of the tunnel plate. This produces an irregularity in the pressure variation of Section VII, especially in the real part, see Figure 25 for example. In addition, the pressure distribution is usually continuous. Only the pressure distributions for rotational oscillations around axis 1 represent an exception to this. Because this rotation axis is near the wing leading edge, we find only small oscillation amplitudes here, so that the tunnel turbulence appears more pronounced in this case (Figures 25 and 26).

The comparison with the three-dimensional theory shows that the measured real parts have a somewhat steeper variation than according to theory. Especially in the outer wing segments, the measured values deviate relatively strongly from the results of the theory in the vicinity of the trailing edge, because here negative measured values occur to an increasing extent because of the three-dimensional flow around the profile (see Figures 23 and 25). Only at higher reduced frequencies can one find a better agreement (Figure 27). In general, we can evaluate the agreement between the three-dimensional theory and the measurement results to be a good one, and one reason for this is that the deviations described above cancel to a certain extent when we integrate over the wing chord. As far as the position of the rotation axis is concerned, we find that extreme rotation axis positions such as the axis 1 cannot be evaluated as favorably as rotation axes in the central part of the wing (for example, see Figures 23 and 25). Therefore, we should expect an improvement in the theory for extreme rotation axis positions by introducing a large number of support points in the chord direction.

/56

The conclusions reached for the side ratio $\Lambda = 3.1$ also apply for the side ratio $\Lambda = 2.5$, as discussed in [30].

In order to be able to compare the measured results with the large aspect ratio theory and the two-dimensional theory, two pressure distributions in the section IV of the rectangular wing with $\Lambda = 3.1$ are plotted separately, see Figures 29, 30a and b. It can be seen that, in the real part and as the reduced frequency $|\omega^*|$ decreases, the three-dimensional theory is superior to the large aspect ratio theory (Figure 29). If there is a large reduced frequency, the converse is true (Figure 30a). No noticeable differences appear in the imaginary part as the reduced frequency is decreased. For a large $|\omega^*|$, the three-dimensional theory is clearly superior (Figure 30b). This result can be considered to be typical for other sections as well. However, one must consider the fact that the two-dimensional theory will have considerably larger deviations in sections close to the end of the wing, because it only applies for plane flow. This clarifies the representation of the local aerodynamic force derivatives in Figures 31 and 32. Since it is a wing with a constant chord, the values of the two-dimensional theory do not change over the span. The large aspect ratio theory, as well as the three-dimensional theory, agree well with the decrease of the measured values towards the end of the wing. This is also true for the smaller aspect ratio $\Lambda = 2.5$, see Figure 32. /62

Figures 33 to 36 show two pressure distributions for rotational oscillations of the two sweptback wings $\Lambda = 3.1$ and 2.5, respectively. The two rotation axes are perpendicular to the flow direction, see Figure 9b.

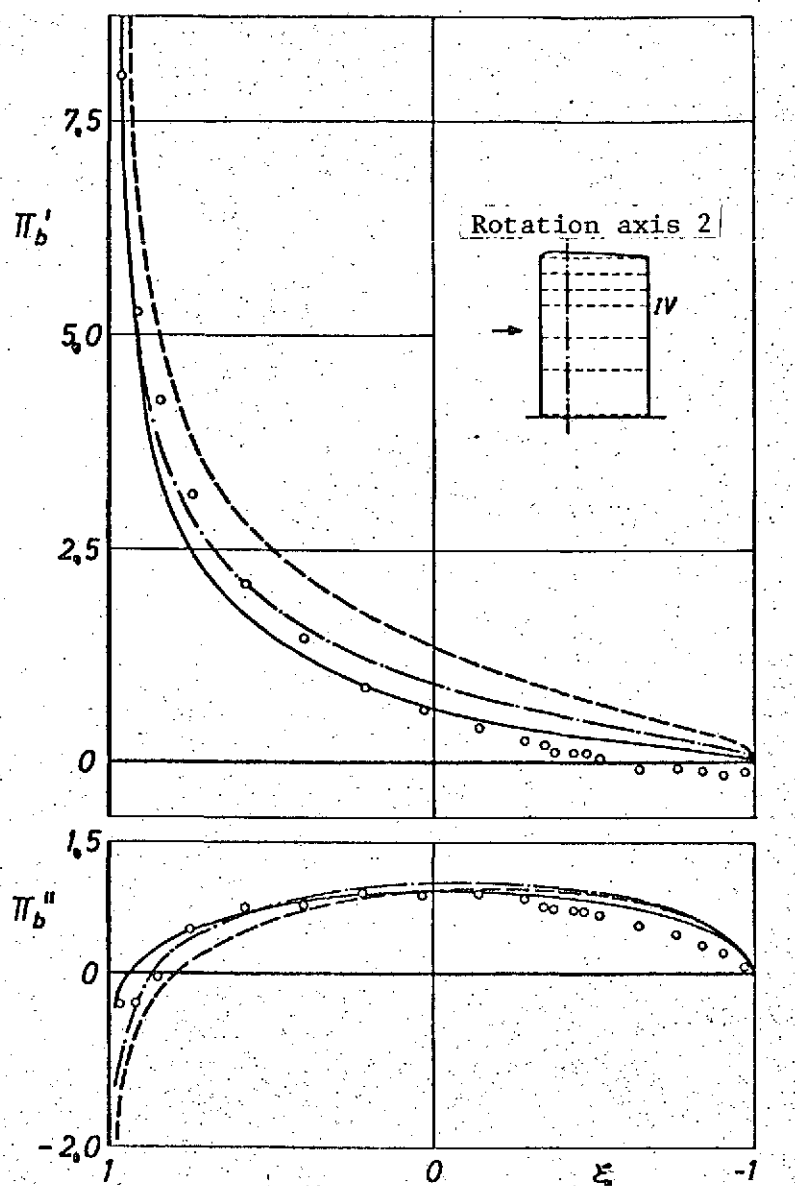


Figure 29. Pressure distribution $\pi_b = \pi_b' + i\pi_b''$ through section IV of rectangular wing for rotational oscillation around axis 2; $\Lambda = 3.1$; $\nu = 6.56$ Hz; $|\omega^*| = 0.304$; o - measurement; — three-dimensional theory; -- large aspect ratio theory; --- two-dimensional theory.

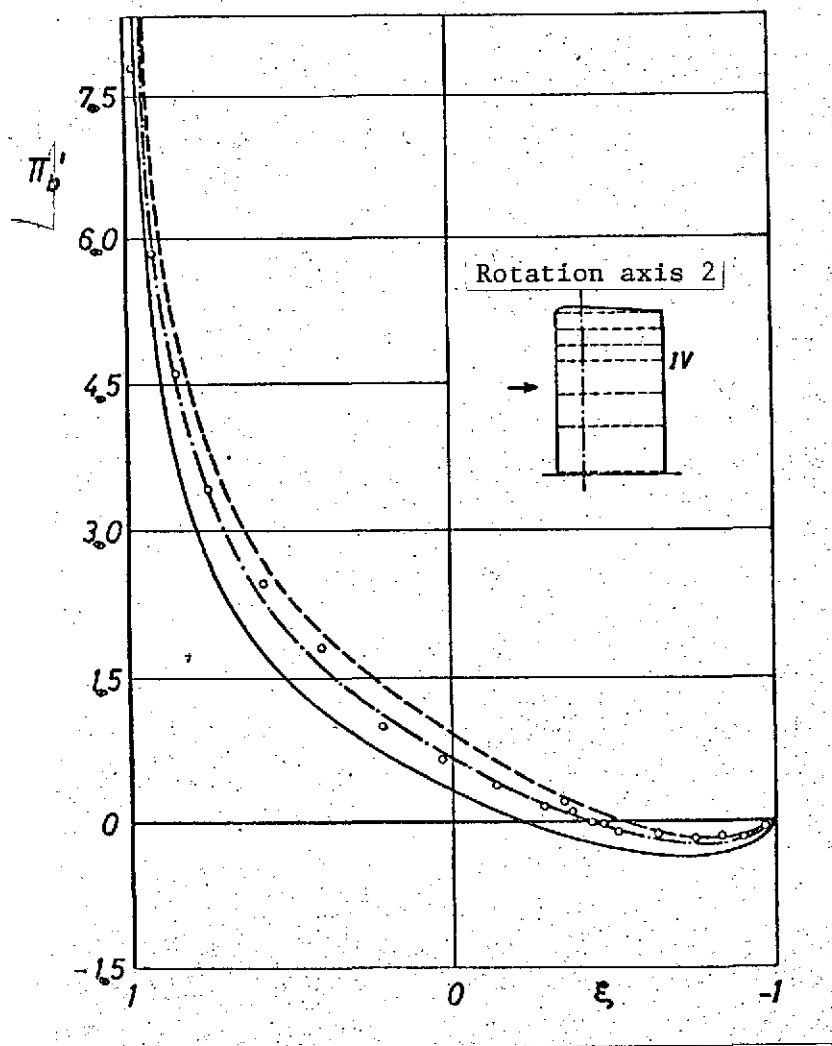


Figure 30a. Pressure distribution $\pi_b = \pi'_b + i\pi''_b$ through section IV of rectangular wing for rotational oscillation around axis 2; real part π'_b ; $\Lambda = 3.1$; $\nu = 16.06$ Hz; $|\omega^*| = 0.744$

o- measurement; — three-dimensional theory; - - - large aspect ratio theory; --- two-dimensional theory.

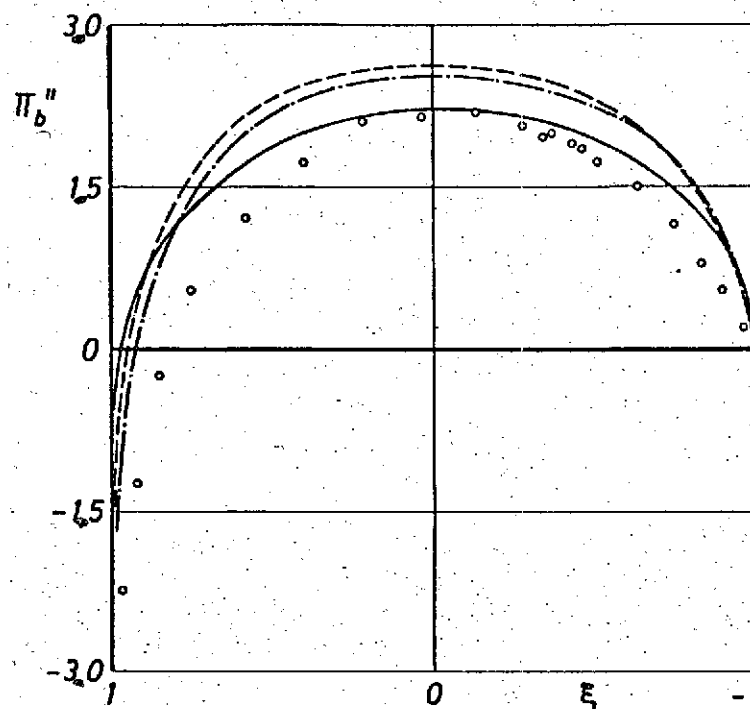


Figure 30b. Pressure distribution $\pi_b = \pi'_b + i\pi''_b$ in section IV of rectangular wing for rotational oscillations around axis 2; imaginary part π''_b ;

$\Lambda = 3.1$; $\nu = 16.06$ Hz; $|\omega^*| = 0.744$

o- measurement; — three-dimensional theory; - - - large aspect ratio theory; --- two-dimensional theory.

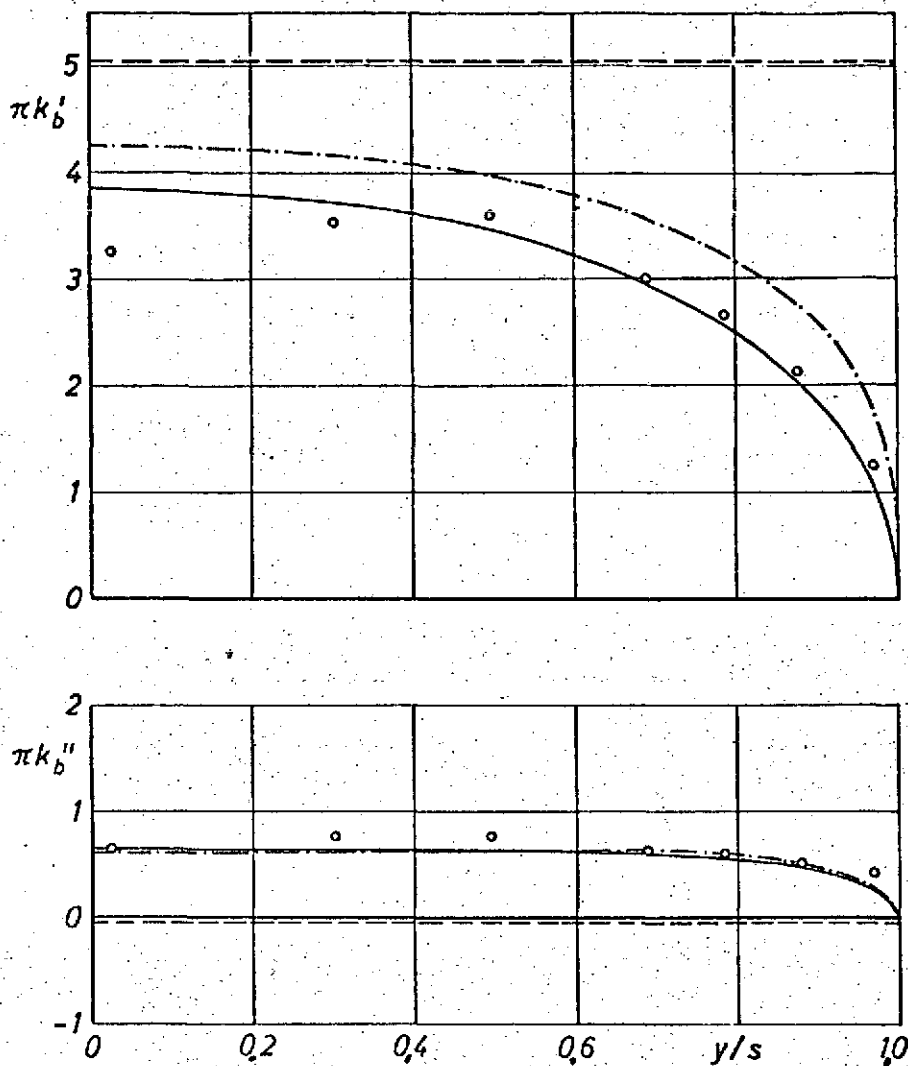


Figure 31. Aerodynamic force distribution in the span direction over rectangular wing with rotational oscillations around axis 2; $|\Lambda| = 3.1$; $\nu = 3 \text{ Hz}$; $|\omega^{\#}| = 0.138$; o - measurement; — three-dimensional theory; -·- large aspect ratio theory; --- two-dimensional theory.

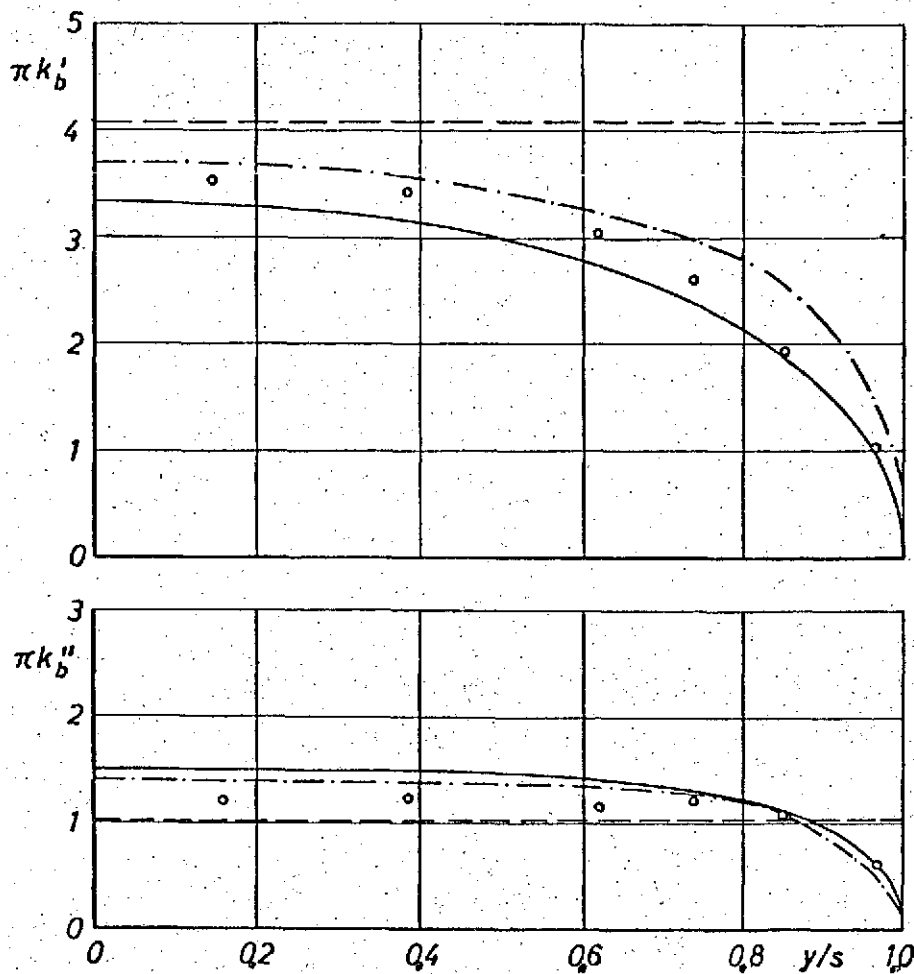
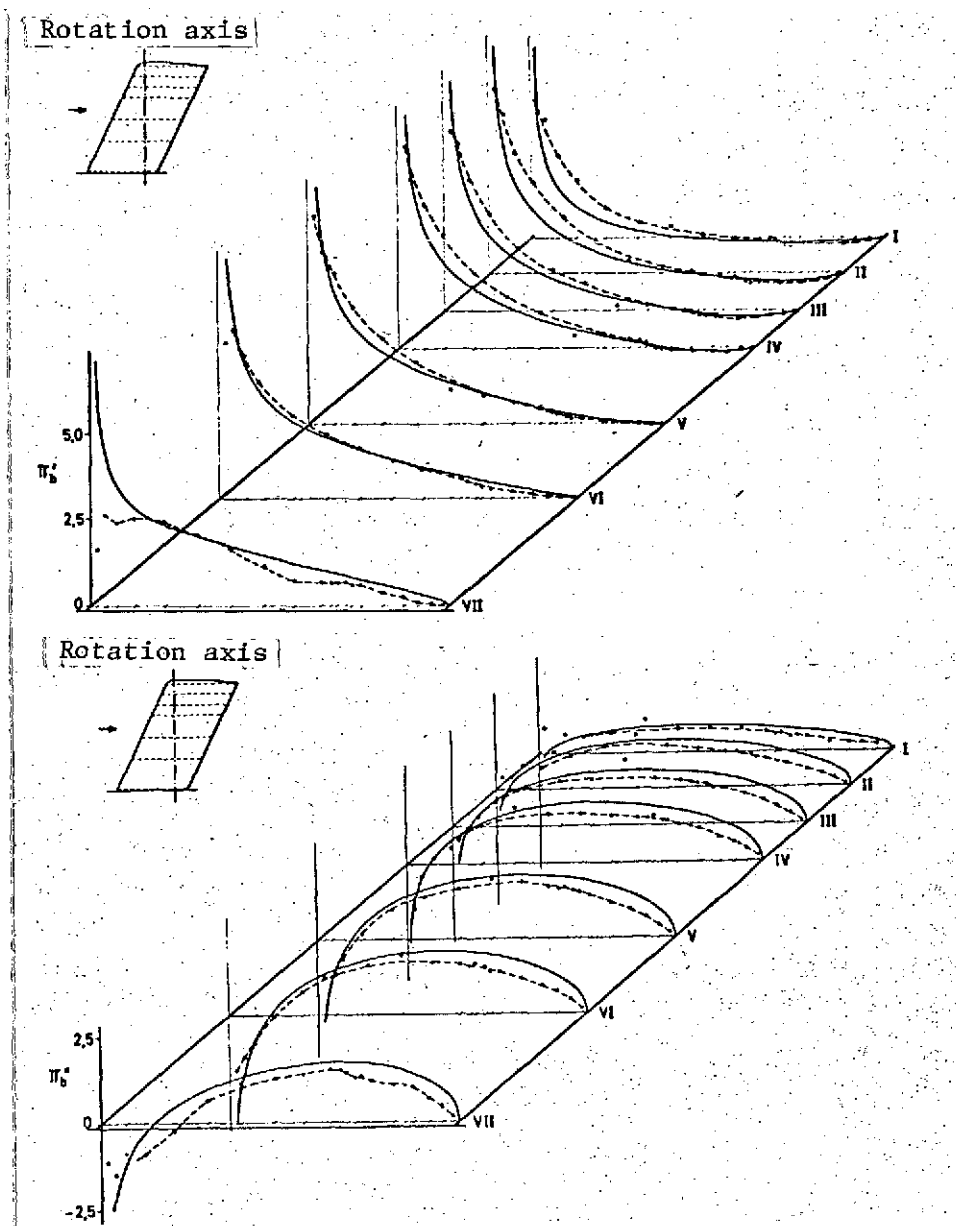
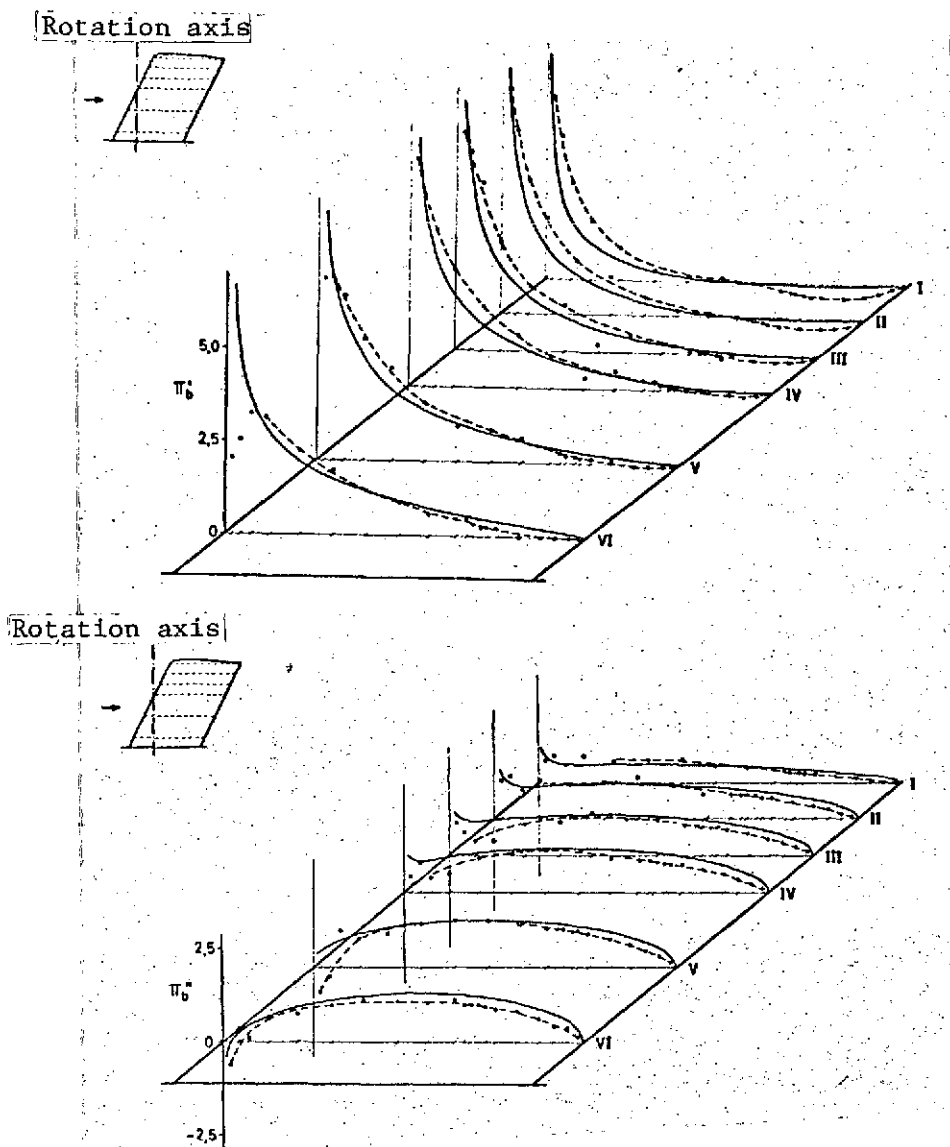


Figure 32. Aerodynamic force distribution in the span direction over rectangular wing with rotational oscillations around axis 3; $\Lambda = 2.5$; $\nu = 10$ Hz; $|\omega^*| = 0.455$; o— measurement; — three-dimensional theory; -·- large aspect ratio theory; --- two-dimensional theory.



Figures 33 and 34. Pressure distribution $[\pi_b = \pi_b' + i\pi_b'']$ over swept-back wing for the rotational oscillations around trailing edge; $\Lambda = 3.1$; $\nu = 14$ Hz; $|\omega^*| = 0.622$; -o- measurement; — three-dimensional theory.



Figures 35 and 36. Pressure distribution $\pi_b = \pi_b' + i\pi_b''$ over swept-back wing for rotational oscillations around leading edge; $\Lambda = 2.5$; $\nu = 8 \text{ Hz}$; $|\omega^*| = 0.358$; -o- measurement; — three-dimensional theory.

The disturbances at the nose of the model caused by tunnel turbulence are more pronounced for the sweptback wing than for the rectangular wing. Here again they appear more pronounced at the lower oscillation frequencies than for the higher ones [31]. The agreement with the three-dimensional theory is about the same as for the rectangular wing.

Figures 37 through 39 again show the pressure distributions of the individual sections in which again we show the values of the large aspect ratio theory and the two-dimensional theory. Considering the real part, it can be seen that the variation of the three-dimensional theory is always below the one for the other two theories. Here again we have no basic changes in the span direction as Figures 38 and 39 show. On the other hand, the imaginary parts do not show this uniform behavior. As already found in Figure 36, if the rotation axis is in front, there are clear changes in the theory in the span direction in the region of the nose. Depending on whether the rotation axis for the individual sections is selected inside the wing or ahead of the leading edge, we find a decrease or increase in the imaginary part according to the three-dimensional theory. Figures 38 and 39 show how the imaginary parts according to the two-dimensional theory and according to the large aspect ratio theory differ. In the two-dimensional theory, there is also an increase at the nose caused by the rotation axis in front of it, but it only occurs for a large distance of the rotation axis (Figure 39). The large aspect ratio theory has the opposite characteristics, because here the imaginary part at the nose decreases more strongly towards the end of the wing. This behavior is not in agreement with the measured results. This can be traced to the influence of the modified function T_1 , which makes itself very pronounced in the imaginary part. This becomes clear in the representation of the theoretical pressure

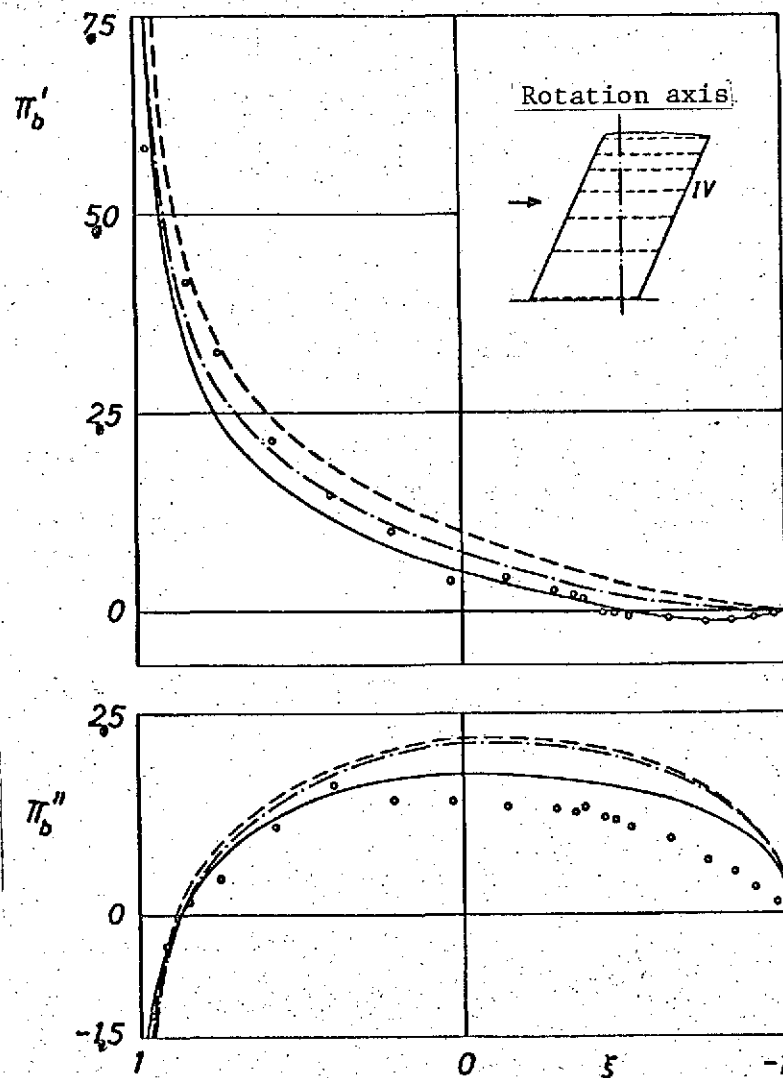


Figure 37. Pressure distribution $\pi_b = \pi'_b + i\pi''_b$ at section IV of sweptback wing for rotational oscillations around trailing edge; $\Lambda = 3.1$; $\nu = 14$ Hz; $|\omega^*| = 0.622$; o- measurement; — three-dimensional theory; --- large aspect ratio theory; -.- two-dimensional theory.

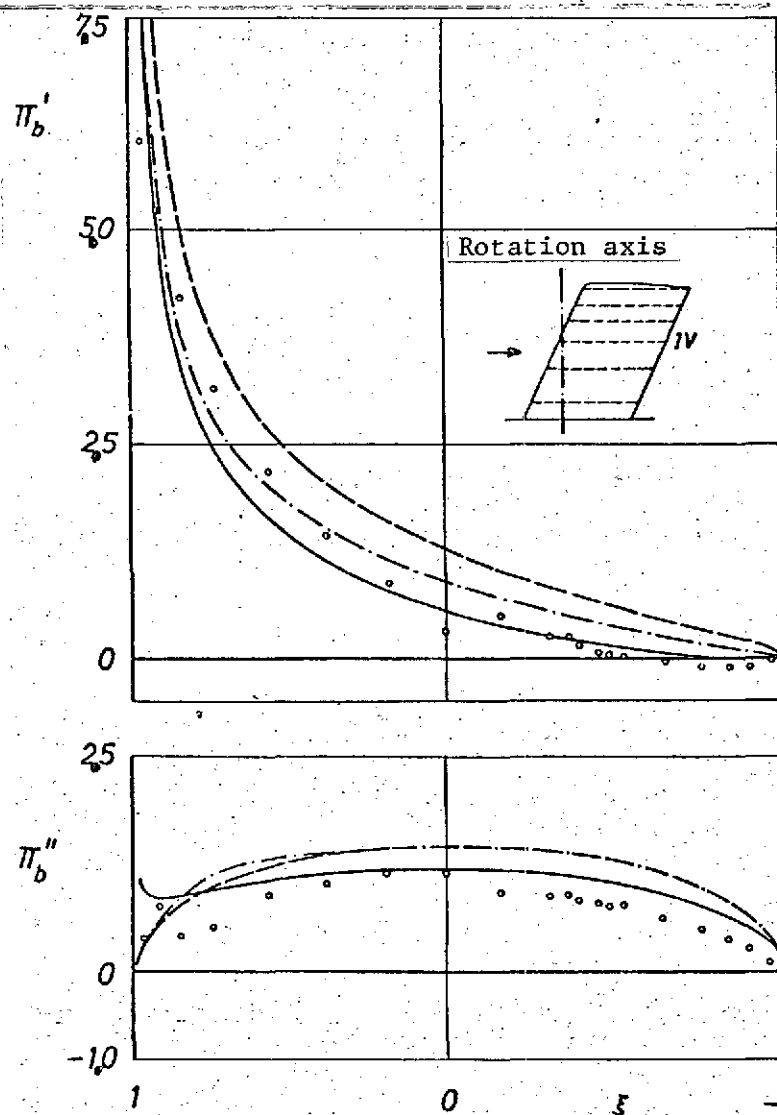


Figure 38. Pressure distribution $\pi_b = \pi'_b + i\pi''_b$ at section IV of sweptback wing for rotational oscillations around trailing edge; $\Lambda = 2.5$; $\nu = 8$ Hz; $|\omega^*| = 0.358$; o- measurement; — three-dimensional theory; --- large aspect ratio theory; -.- two-dimensional theory.

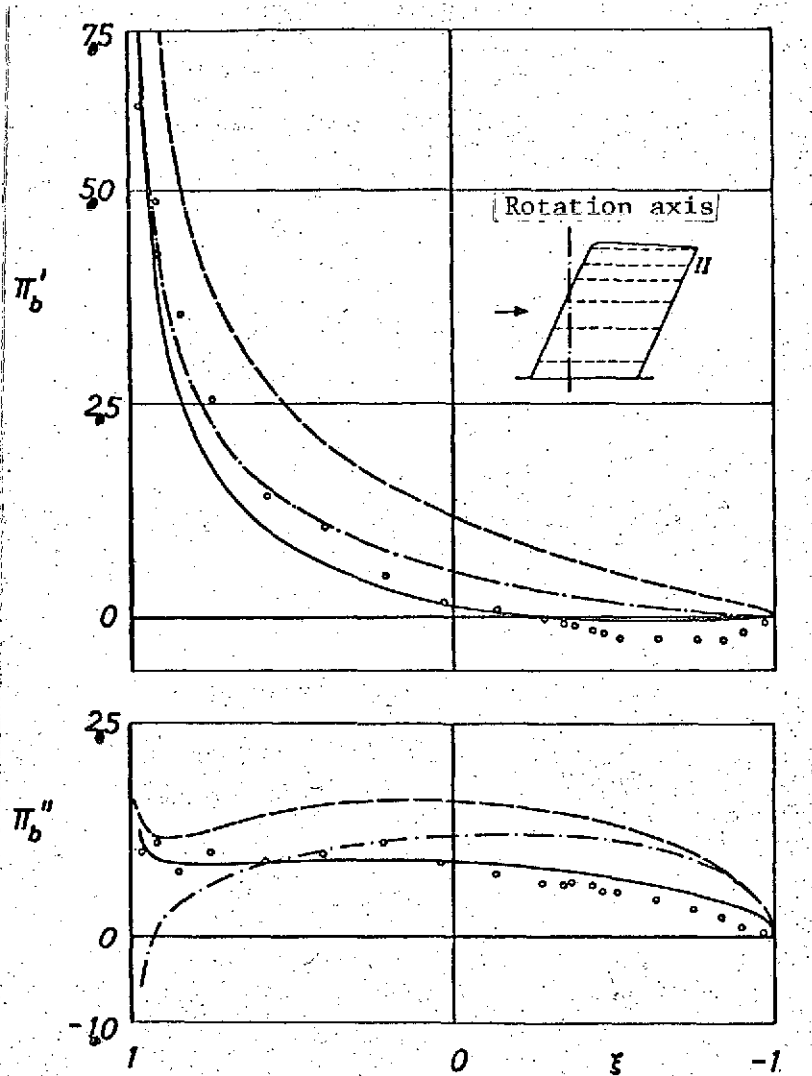


Figure 39. Pressure distribution $\pi_b = \pi'_b + i\pi''_b$ at section II of sweptback wing for rotational oscillations around trailing edge; $\Lambda = 2.5$; $\nu = 8$ Hz; $|\omega^*| = 0.358$; o- measurement; — three-dimensional theory; -- large aspect ratio theory; -.- two-dimensional theory.

distribution in the span direction for the three theories, as shown in Figures 40 and 41. In Figures 40 and 41, we show the theoretical pressure variations over the semispan for a number of stations in the chord direction. Since the two-dimensional theory results in straight lines for all stations, only one station is shown in the region of the leading edge and the trailing edge. The real part shows a good basic agreement between the three-dimensional theory and the large aspect ratio theory (Figure 40). The imaginary part, on the other hand, shows the deviations mentioned above (Figure 41).

Figures 42 and 43 show two aerodynamic force distributions in the span direction.

Figures 44 to 53 show the global aerodynamic force and moment derivatives for pitch oscillations of the rectangular wings and of the sweptback wings around various rotation axes.

The representation of the aerodynamic force derivatives shows that, by displacing the rotation axis from the leading edge to the center of the wing, a flatter increase in the imaginary part is produced. For all of the configurations, one can see that there is a relatively good agreement between the measured values and the three-dimensional theory. Here again the large aspect ratio theory also shows good results. As expected, the deviations of the two-dimensional theory are especially large for the real part.

The moment derivatives are referred to the neutral axis. For this reference axis, the large aspect ratio theory does not introduce any change over the two-dimensional theory, because then the T function is not contained in the formulas [see Equations (15) and (32)]. There is quite good agreement between

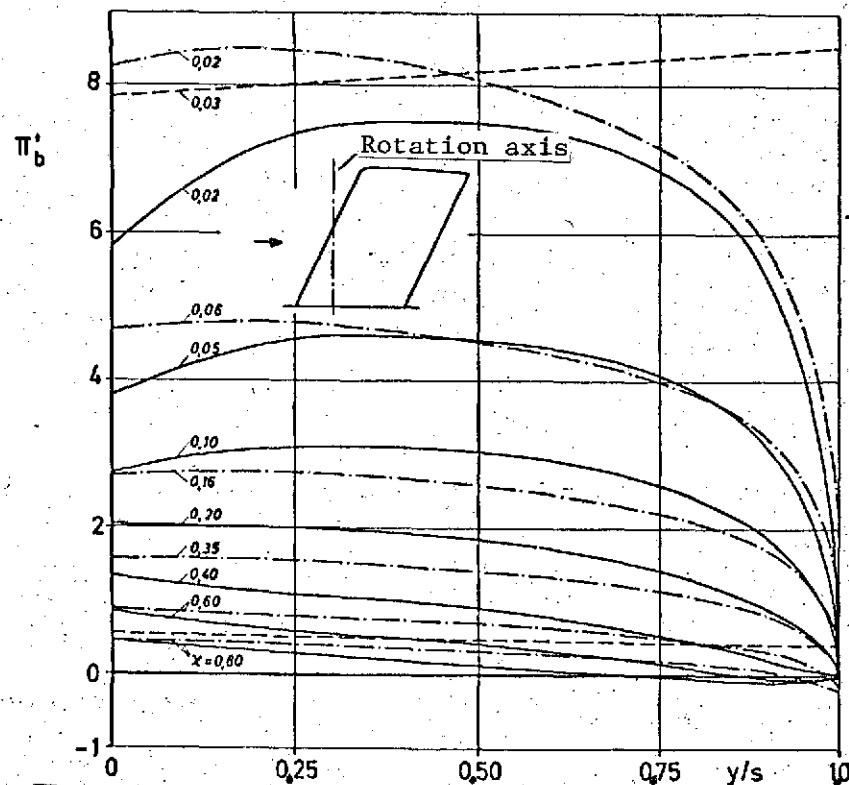


Figure 40. Theoretical pressure variation $\pi'_b = \pi'_b + i\pi''_b$ in span direction over sweptback wing for rotational oscillations around leading edge; real part π'_b ; $\Lambda = 2.5$; $|\omega^*| = 0.358$; — three-dimensional theory; - - - large aspect ratio theory; --- two-dimensional theory.

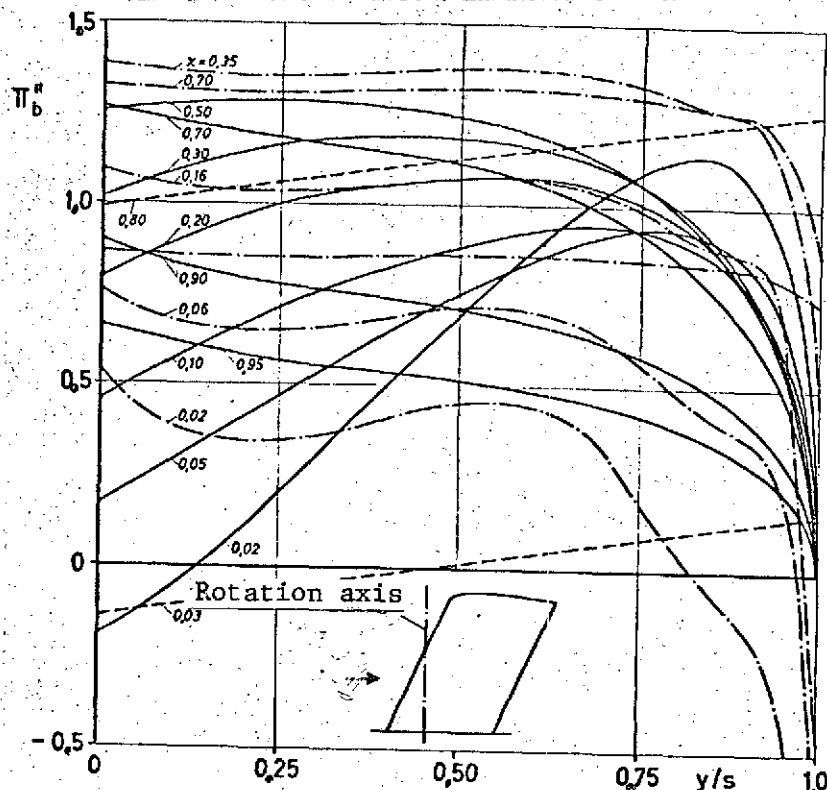


Figure 41. Theoretical pressure variation $\pi''_b = \pi'_b + i\pi''_b$ in span direction over sweptback wing for rotational oscillations around leading edge; imaginary part π''_b ; $\Lambda = 2.5$; $|\omega^*| = 0.358$; — three-dimensional theory; - - - large aspect ratio theory; --- two-dimensional theory.

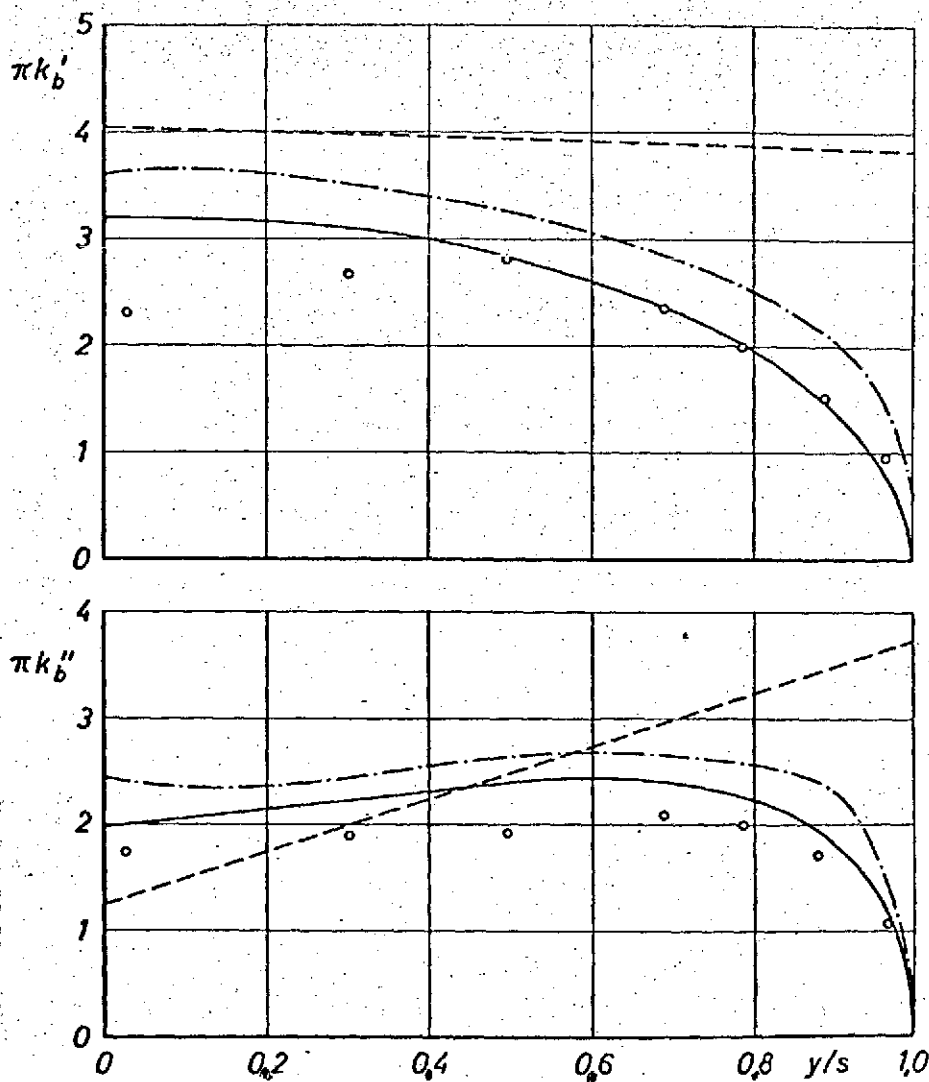


Figure 42. Aerodynamic force distribution in span direction over sweptback wing for rotational oscillations around leading edge $\Lambda = 3.1$; $\nu = 6$ Hz; $|\omega^*| = 0.289$; o- measurement; — three-dimensional theory; -·- large aspect ratio theory; --- two-dimensional theory.

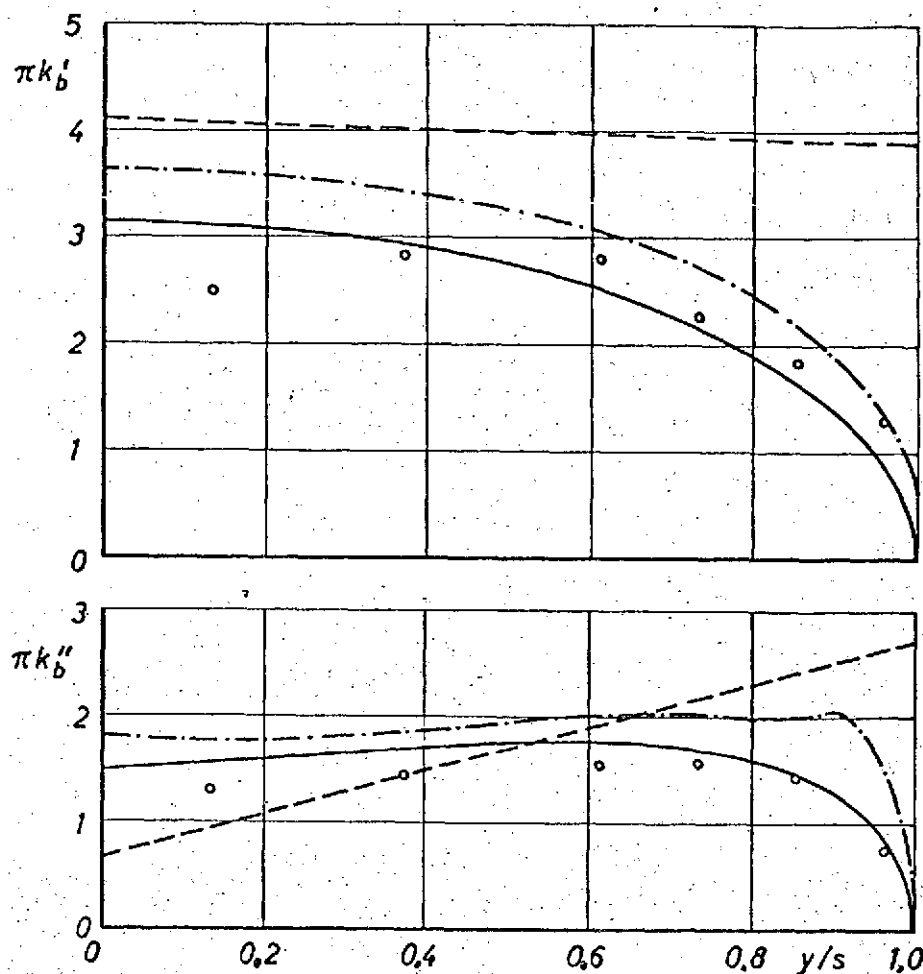


Figure 43. Aerodynamic force distribution in span direction over sweptback wing for rotational oscillations around trailing edge $\Lambda = 2.5$; $\nu = 10$ Hz; $|\omega^*| = 0.453$; o - measurement; — three-dimensional theory; --- large aspect ratio theory; -.- two-dimensional theory.

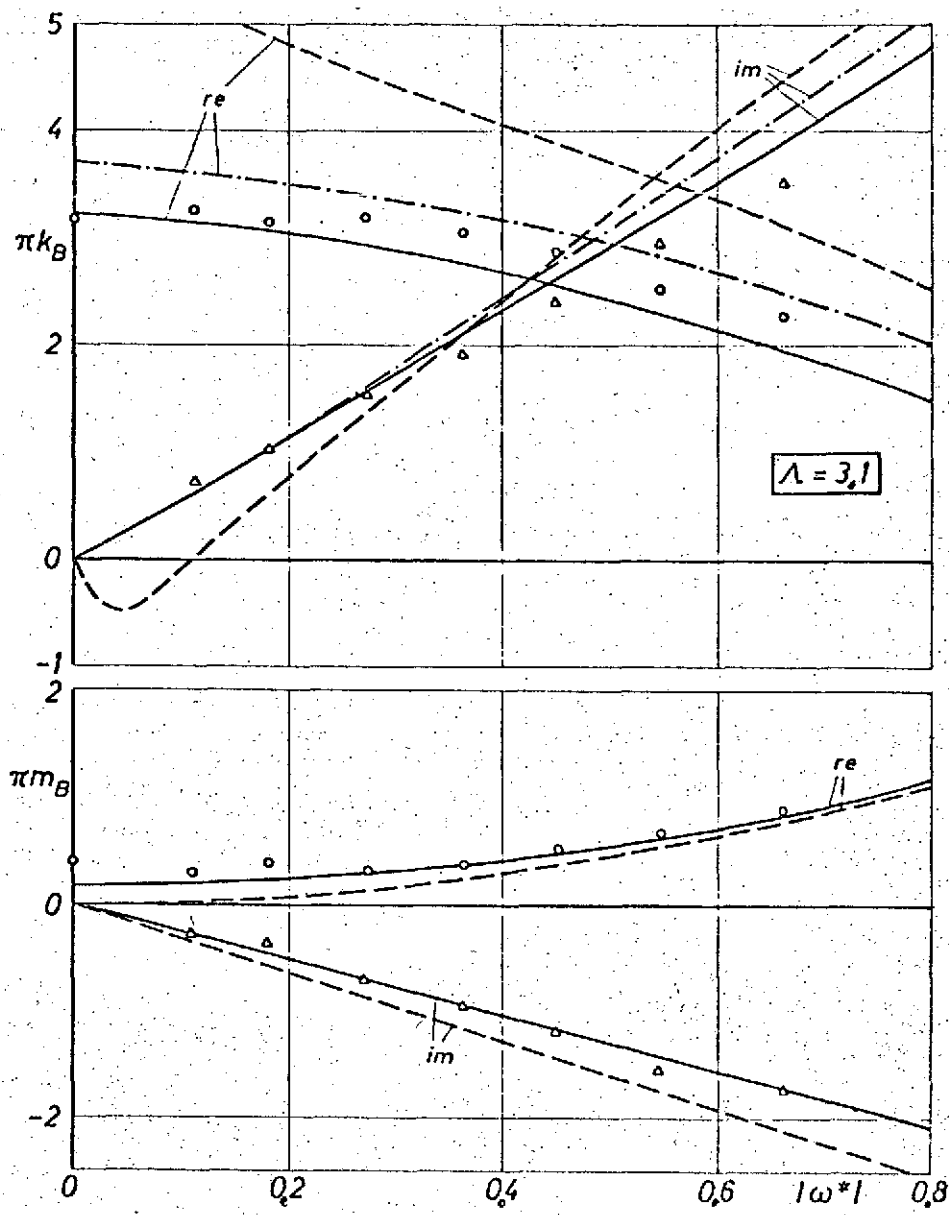


Figure 44. Global forces and moments of the rectangular wing for rotational oscillations around axis 1. o

o- real part } measurement at $Re = 1.6 \cdot 10^6$
 Δ - imaginary part }
 — three-dimensional theory
 - - - large aspect ratio theory
 - · - two-dimensional theory

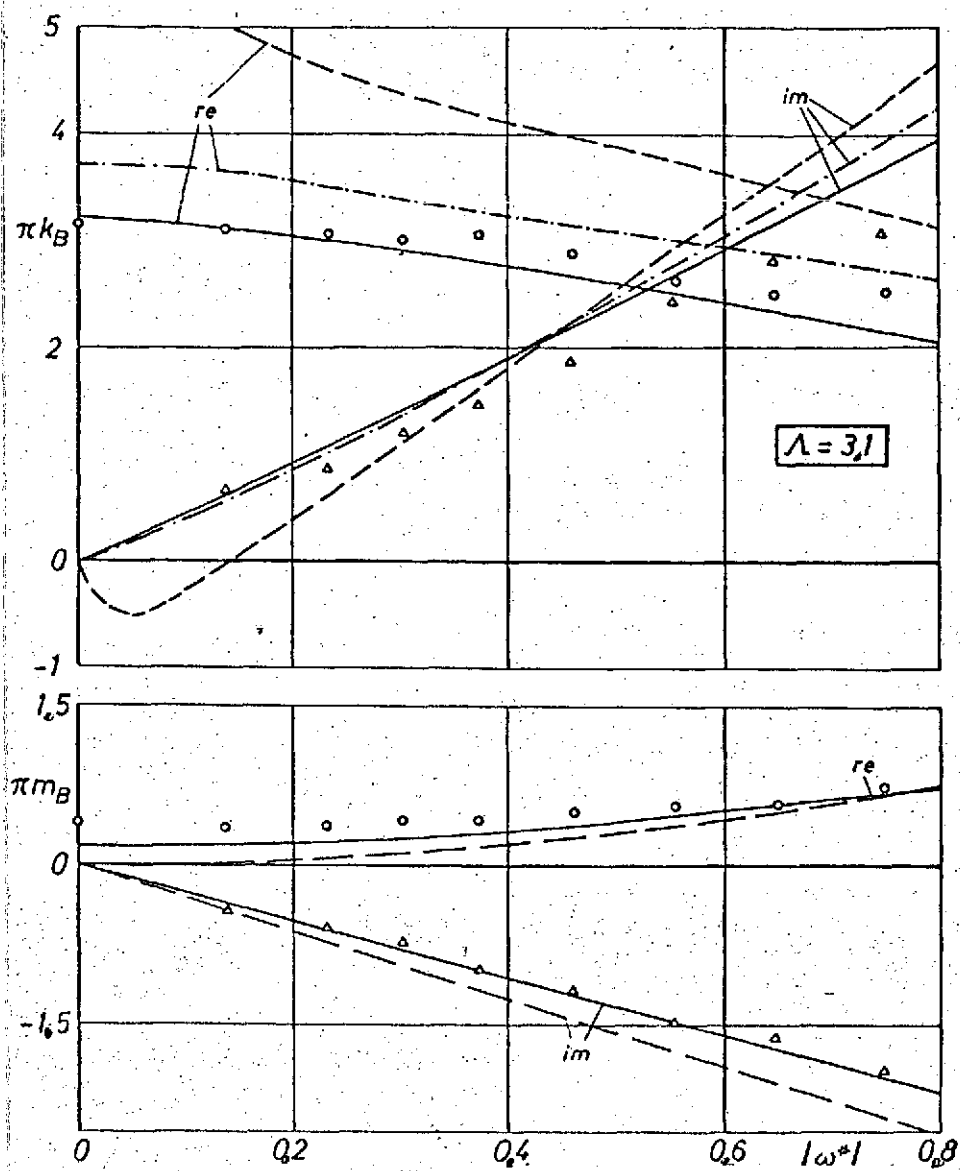


Figure 45. Global forces and moments of the rectangular wing for rotational oscillations around axis 2.

o- real part } measurement at $Re = 1.6 \cdot 10^6$
 Δ - imaginary part }
 — three-dimensional theory
 - - - large aspect ratio theory
 --- two-dimensional theory

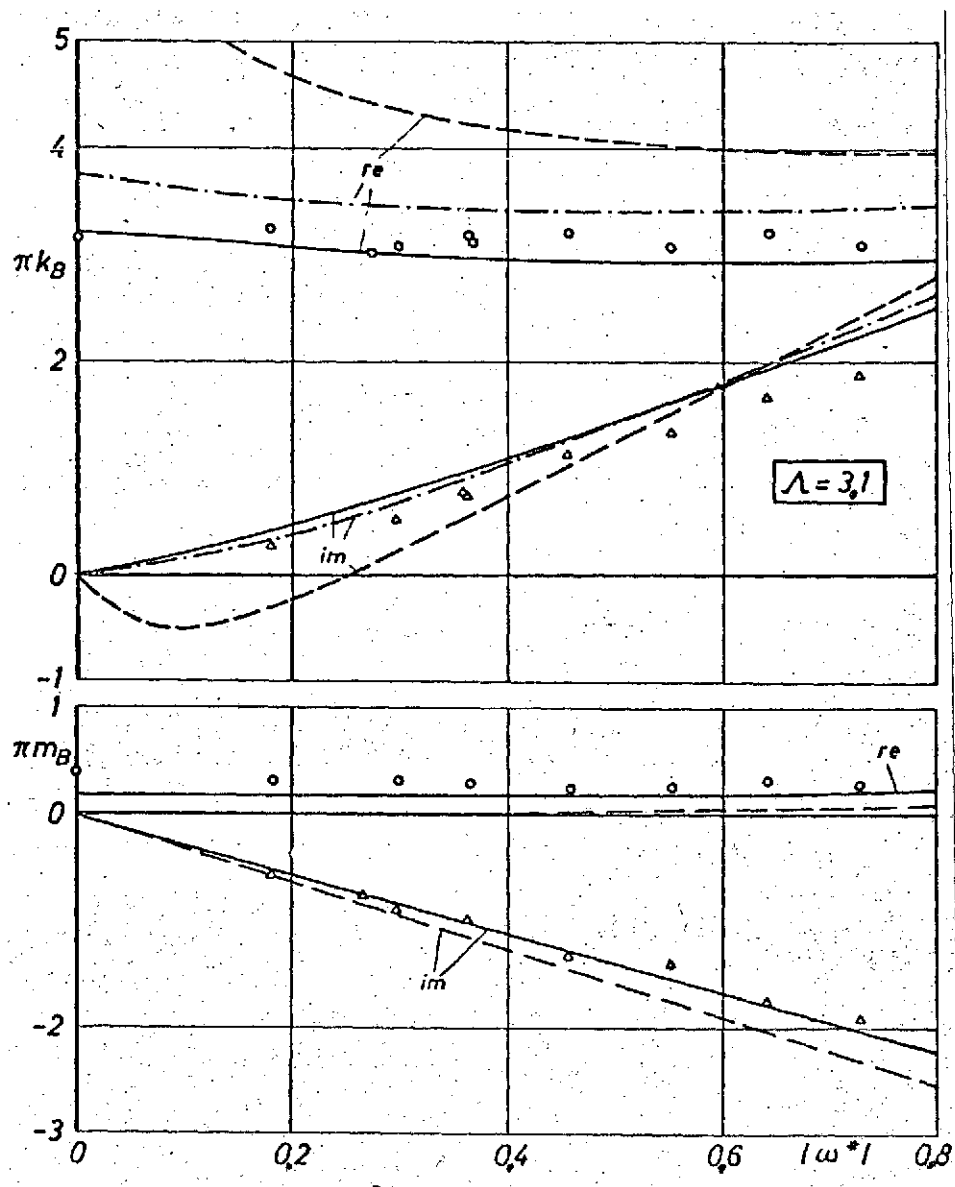


Figure 46. Global forces and moments of the rectangular wing for rotational oscillations around axis 3.

\circ - real part
 Δ - imaginary part

 $\left. \begin{array}{l} \text{measurement at} \\ \text{Re} = 1,6 \cdot 10^6 \end{array} \right\}$

 --- three-dimensional theory
 --- large aspect ratio theory
 --- two-dimensional theory

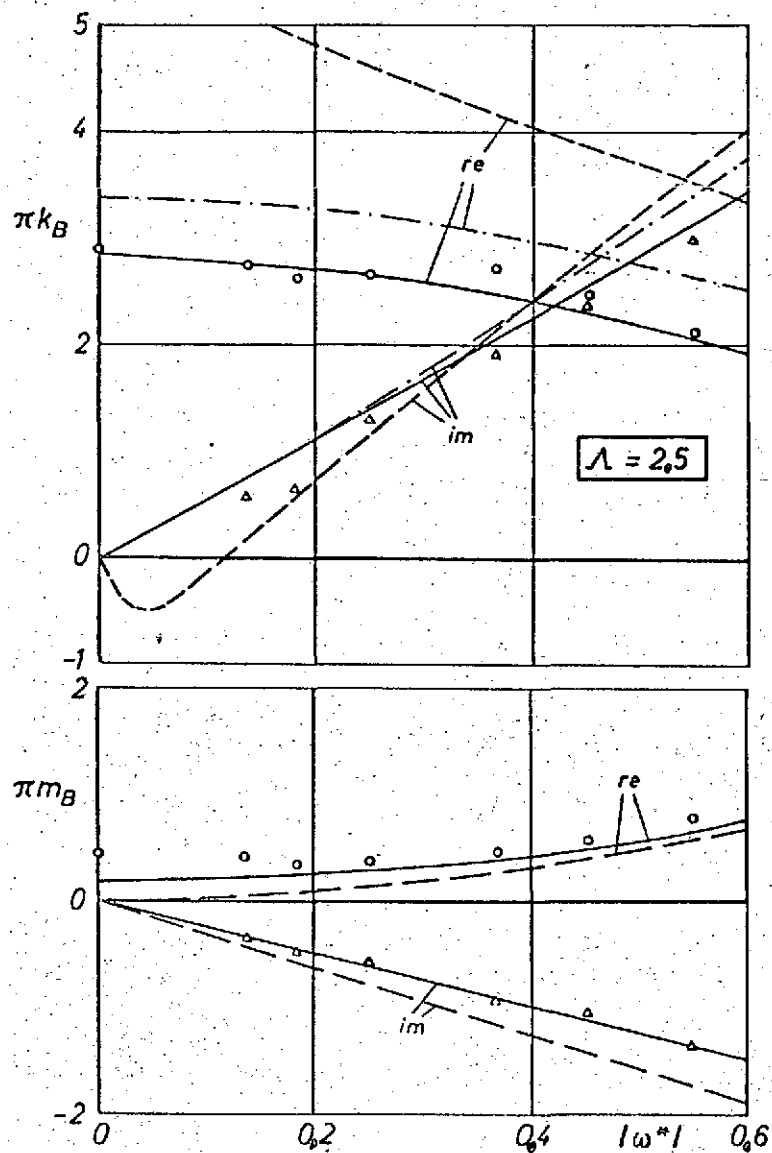


Figure 47. Global forces and moments of the rectangular wing for rotational oscillations around axis 1.

o- real part } measurement at $Re = 1.6 \cdot 10^6$
 Δ- imaginary part }

— three-dimensional theory
 - - - large aspect ratio theory
 - · - two-dimensional theory

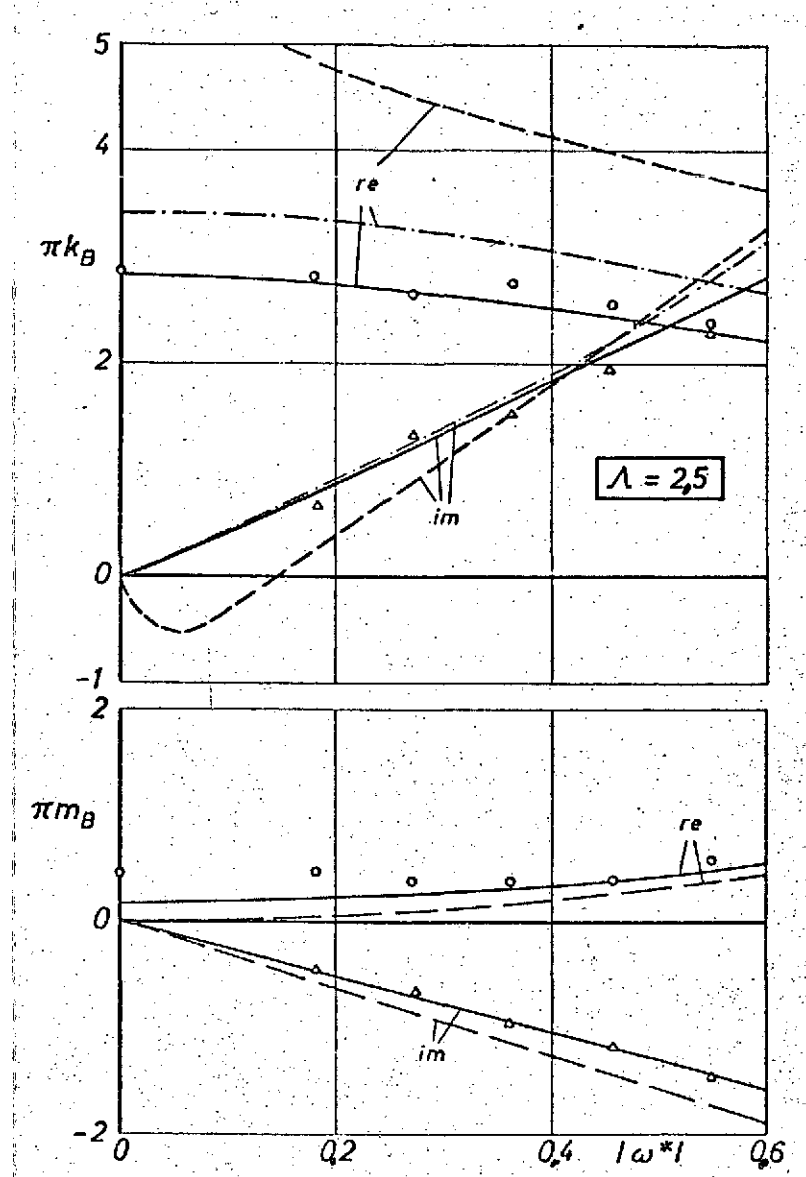


Figure 48. Global forces and moments of the rectangular wing for rotational oscillations around axis 2.

o- real time } measurement at $Re = 1.6 \cdot 10^6$
 Δ- imaginary time }
 — three-dimensional theory
 - - large aspect ratio theory
 - · - two-dimensional theory.

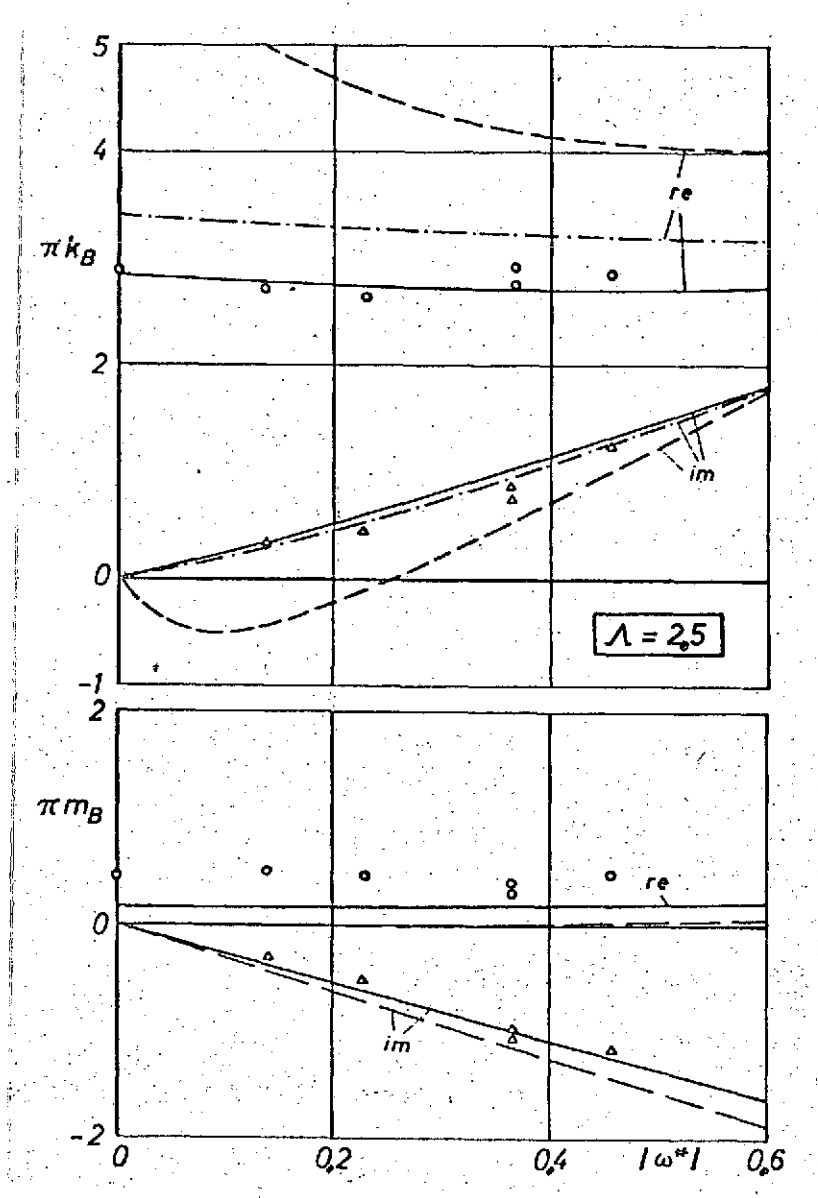


Figure 49. Global forces and moments of the rectangular wing for rotational oscillations around axis 3.

o- real time } measurement at
Δ- imaginary time } Re = $1,6 \cdot 10^6$

- three-dimensional theory
- large aspect ratio theory
- two-dimensional theory

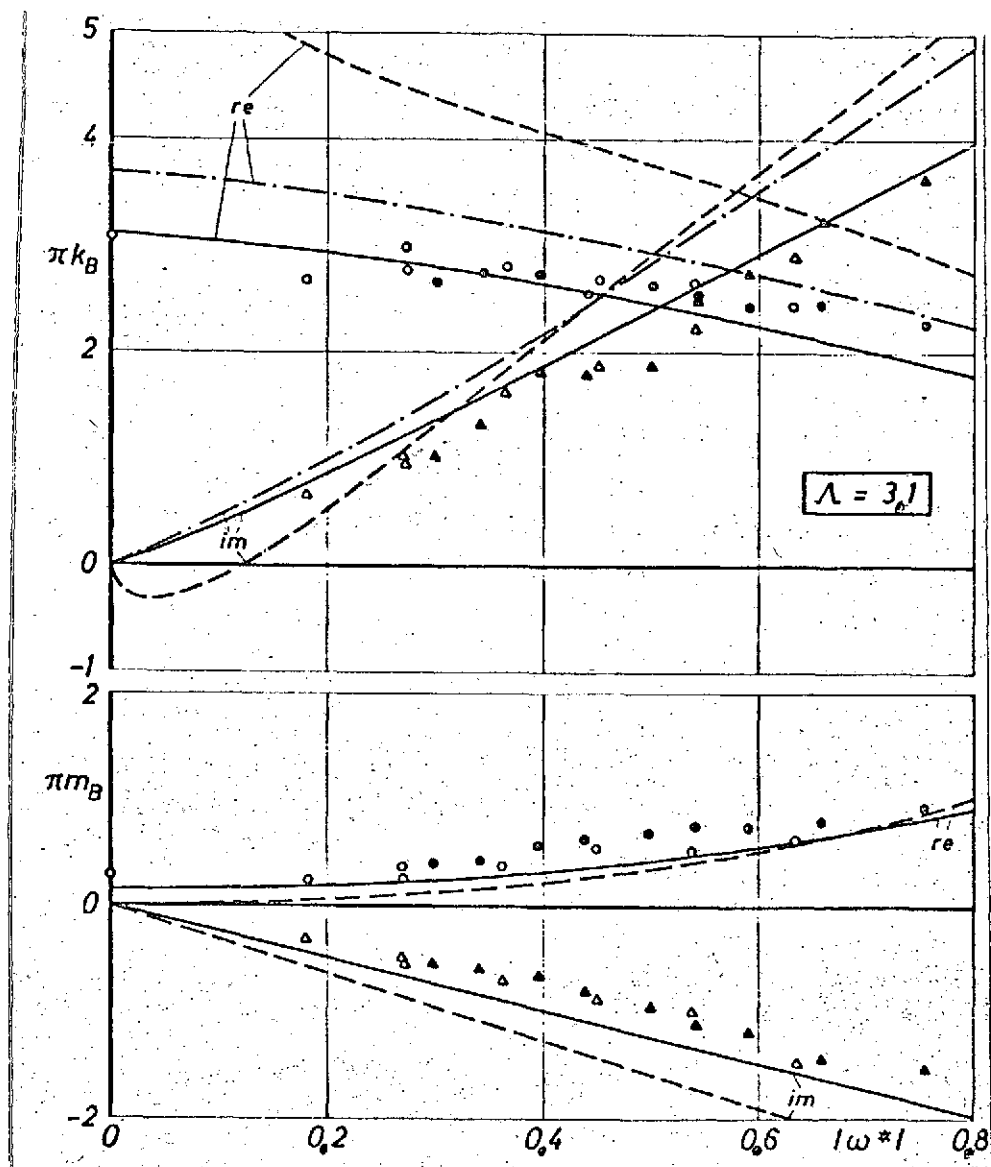


Figure 50. Global forces and moments of sweptback wing for rotational oscillations around leading edge.

o- real part	} measurement at $Re = 1,65 \cdot 10^6$	— three-dimensional theory
Δ - imaginary part		
●- real part	} measurement at $Re = 1,45 \cdot 10^6 - 0,57 \cdot 10^6$	- - - two-dimensional theory
\blacktriangle - imaginary part		

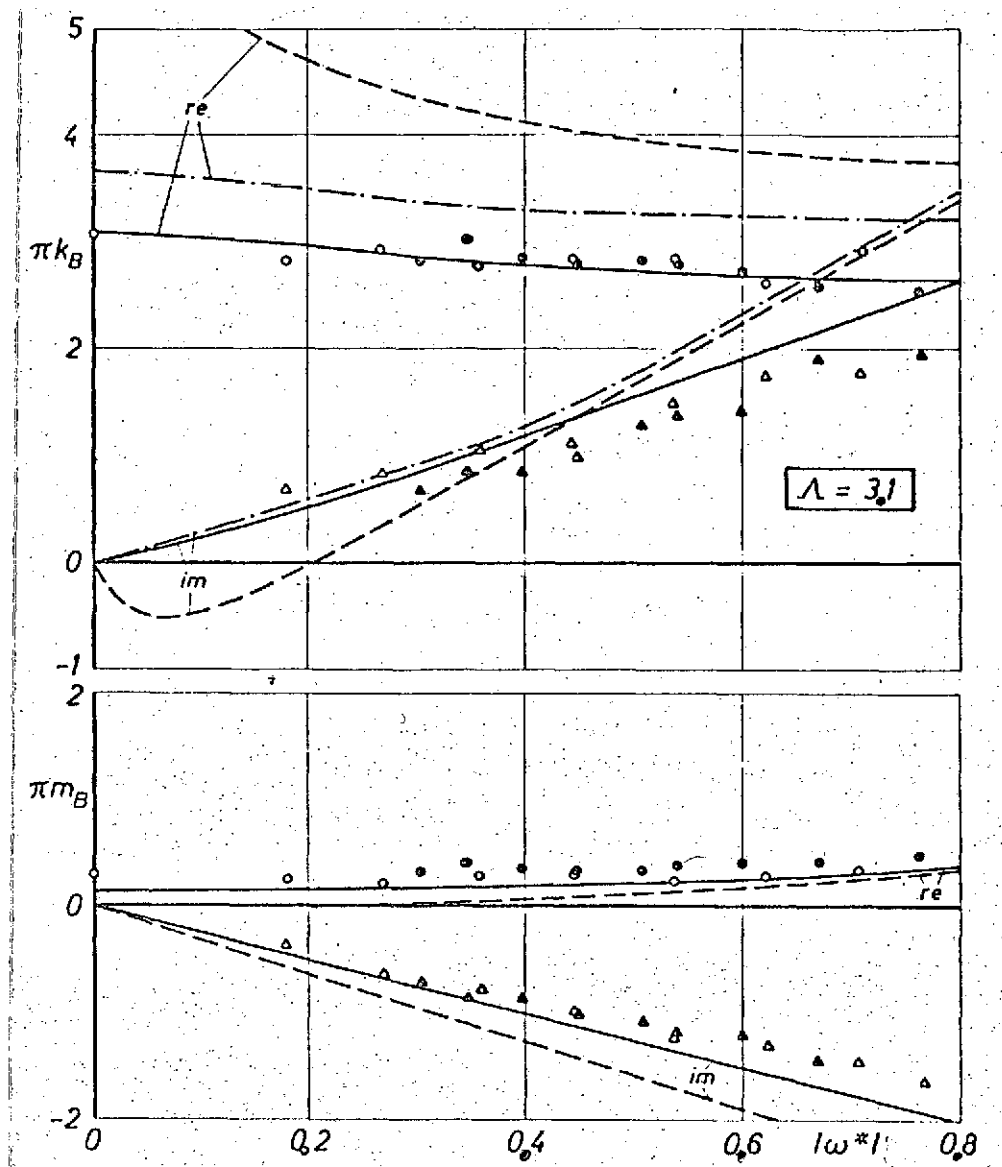


Figure 51. Global forces and moments of sweptback wing for rotational oscillations around trailing edge.

○- real part	} measurement at $Re = 1.65 \cdot 10^6 = \text{const}$	— three-dimensional theory
△- imaginary part		- - - large aspect ratio theory
●- real part	} measurement at $Re = 1.45 \cdot 10^6 - 0.57 \cdot 10^6$	- · - two-dimensional theory
▲- imaginary part		

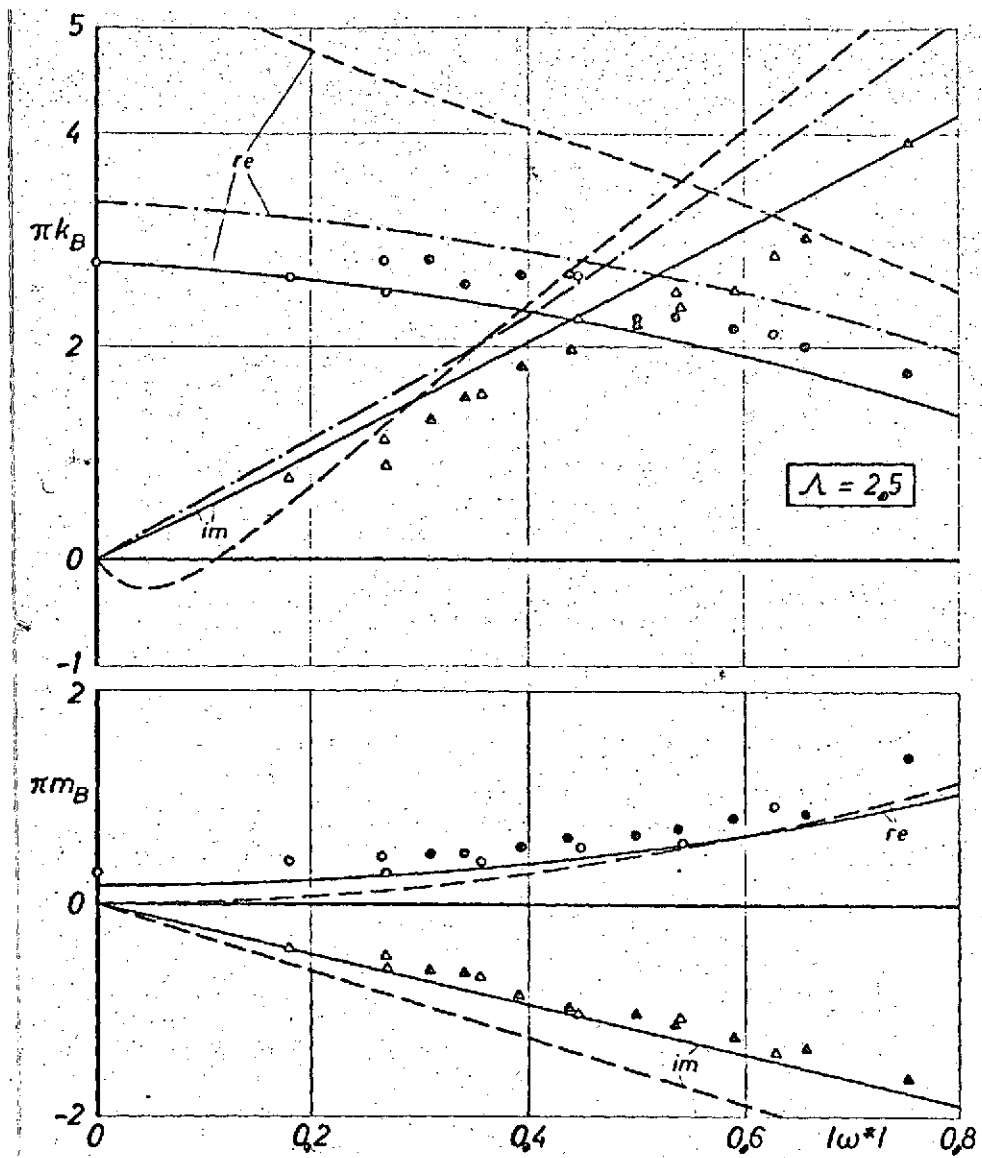


Figure 52. Global forces and moments of sweptback wing for rotational oscillations around leading edge.

o- real part } measurement at $Re = 1.65 \cdot 10^6 = \text{const}$ } — three-dimensional theory
 Δ- imaginary part } $Re = 1.65 \cdot 10^6 = \text{const}$ } --- large aspect ratio theory
 ●- real part } measurement at $Re = 1.45 \cdot 10^6 - 0.57 \cdot 10^6$ } --- two-dimensional theory
 ▲- imaginary part } $Re = 1.45 \cdot 10^6 - 0.57 \cdot 10^6$ }

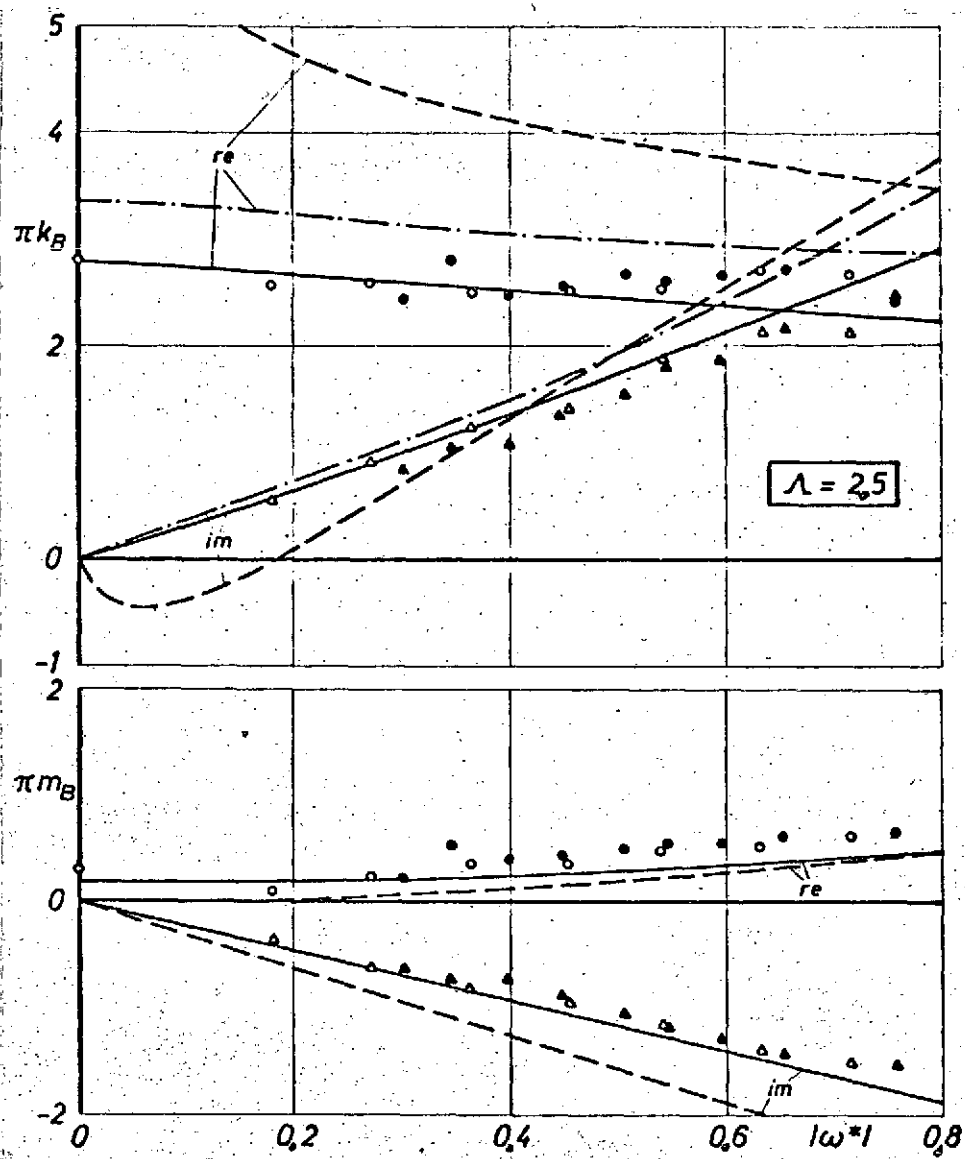


Figure 53. Global forces and moments of sweptback wing for rotational oscillations around trailing edge.

o- real part } measurement at $Re = 1.65 \cdot 10^6 = \text{const}$ } — three-dimensional theory
 Δ- imaginary part } measurement at $Re = 1.65 \cdot 10^6 = \text{const}$ } --- large aspect ratio theory
 ●- real part } measurement at $Re = 1.45 \cdot 10^6 - 0.57 \cdot 10^6$ } --- two-dimensional theory
 ▲- imaginary part } measurement at $Re = 1.45 \cdot 10^6 - 0.57 \cdot 10^6$ }

measured values and the three-dimensional theory for the moment derivatives. It is somewhat better for the rectangular wings than for the sweptback wings.

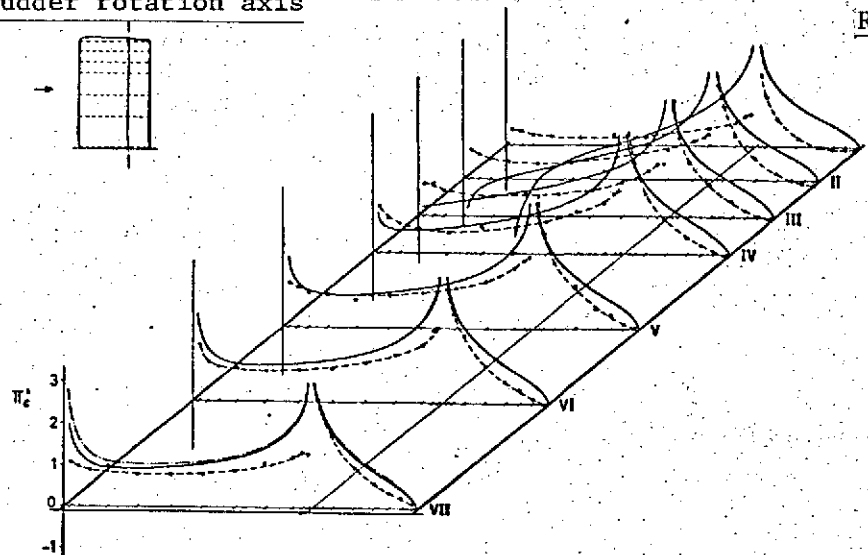
The representations of the global derivatives of the swept- /83
back wings also contain measured values obtained at various Reynolds numbers. In these measurements, we did not vary the oscillation frequency as before, but we brought about a change in the reduced frequency by dropping the stagnation pressure at a constant oscillation frequency of $\nu = 6$ Hz. Increasing reduced frequencies, therefore, means decreasing Reynolds numbers. The Reynolds number was reduced from $Re = 1.65 \cdot 10^6$ for $|\omega^*| \approx 0.270$ to $Re = 0.57 \cdot 10^6$ for $|\omega^*| \approx 0.760$. As Figures 50 through 53 show, we were not able to establish any noticeable influence of the Reynolds number in this range, because all the measured values lie within a certain scatter range.

7.3.3. Rudder rotation

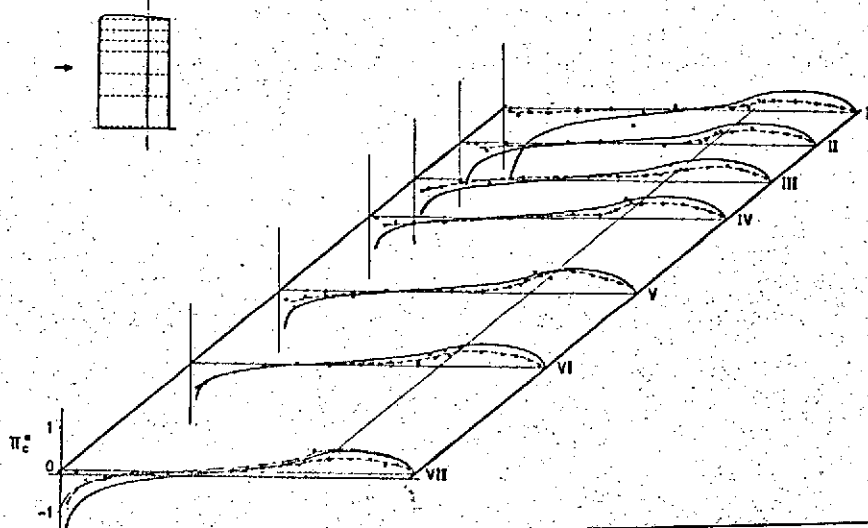
Figures 54 to 57 contain two pressure distributions of the rectangular wings for rudder rotational oscillations around the rudder leading edge. The fin is fixed and is not set at an angle. The large aspect ratio theory curves are plotted, in addition to the measured values for this oscillation form. It was not possible to use the collocation method for solving this lifting surface theory, according to [3], because the three support points in the chord direction are not sufficient to be able to determine the singularity which occurs for rudder oscillations at the rudder slit (see also [38]).

The two-dimensional theory is also shown, in addition to the large aspect ratio theory, for the section closest to the model root, that is Section VII at $\Lambda = 3.1$ or Section VI at $\Lambda = 2.5$.

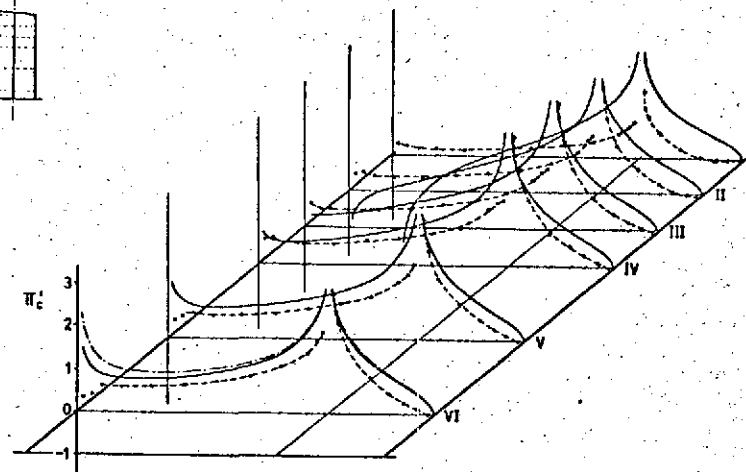
Rudder rotation axis



Rudder rotation axis



Rudder rotation axis



Rudder rotation axis

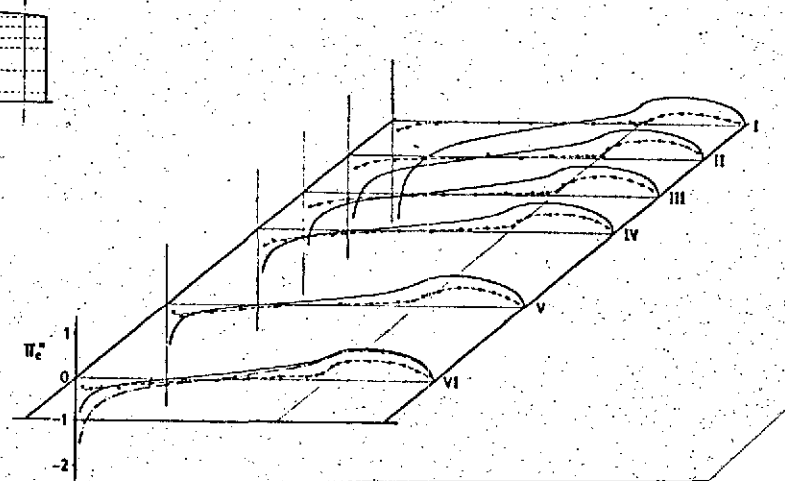


Figure 54 and 55. Pressure distribution $\pi_c = \pi'_c + i\pi''_c$ over rectangular wing for rudder rotational oscillations $\Lambda = 3, 1$; $\nu = 6 \text{ Hz}$; $|\omega^*| = 0, 349$. -o- measurement; — large aspect ratio theory; -.- two-dimensional theory.

Figures 56 and 57. Pressure distribution $\pi_c = \pi'_c + i\pi''_c$ over rectangular wing for rudder rotational oscillations $\Lambda = 3, 1$; $\nu = 6 \text{ Hz}$; $|\omega^*| = 0, 349$. -o- measurement; — large aspect ratio theory; -.- two-dimensional theory.

The variation of the two-dimensional theory is identical for all sections; this was also true for the sweptback wing discussed below.

It can be seen that there is good agreement over a wide range of the model area, especially at the large aspect ratio $\Lambda = 3.1$ (Figures 54 and 56), between the measured values and the large aspect ratio theory. The measured values are, as expected, usually somewhat smaller than the theoretical values. Only over the rudder is the measured real part increase steeper in the vicinity of the rudder slit than predicted by theory, so that here the measured values exceed even the large aspect ratio theory and the two-dimensional theory (see, for example, section [V] in Figure 54). The fact that the increase in the measured real parts is not as steep over the fin can be attributed to the formation of the rudder slit. Because the rudder slit was produced by cutting open the resin skin of the model, a sharp edge resulted, which carries out only slight deflections corresponding to the rudder oscillation amplitude. These deflections of the rudder leading edge have the effect of a rudder step oscillation. Apparently the pressure distribution over the fin depends greatly on the nature of the rudder slit and on the motion of the rudder leading edge. In the results presented, the deflection of the rudder leading edge amounted to only a few percent of the deflection of the rudder trailing edge. /86

The variation of the large aspect ratio theory in the span direction has a decrease towards the nose in the vicinity of the wing tip. This decrease occurs for both components, whereas for wing rotation, we only found it in the imaginary part (see above). This is a contradiction to the measured results, because they take on a uniform variation over the fin. The reason for the differing behavior of the theory can be attributed to the

various approximations made. These approximations were made in the large aspect ratio theory. The modification of the T function with respect to the pressure variation has an especially large effect on the front half of the wing. It does not have a strong effect over the rudder. The pressure variation of the large aspect ratio theory over the rudder is therefore hardly changed at the wing tip, compared with the two-dimensional theory. (see Figures 58 and 59). This fact contradicts the measured values, because the measured real parts over the rudder are negative and increase towards the outside, which is produced by the three-dimensional flow, just like for wing rotation (see Figures 54 and 56).

Figures 60 and 61 show aerodynamic force distributions of the rectangular wings in the span direction. The measured values are obtained by integrating the measured pressure distributions /91 over the entire wing chord at the individual measurement sections. For the aspect ratio $\Lambda = 3.1$, we have approximate agreement with the large aspect ratio theory. The fact that this theory gives a good representation of the pressure equalization over the wing is a result of the decrease in the theoretical variation at the nose discussed above. As to be expected, large deviations already occur for the aspect ratio $\Lambda = 2.5$ (Figure 61).

Figures 62 and 63 show aerodynamic force distributions of the rudder in the span direction. The measured values are obtained by integration over the pressure distribution measured over the rudder at the individual sections. It can be seen that, even for the large aspect ratio $\Lambda = 3.1$, there are considerable deviations between the measured values and the two theories (Figure 62). Here the large aspect ratio theory gives only a slight improvement compared to the two-dimensional theory. The reason for this is that the terms independent of the T function in the expressions for the rudder derivatives increase [see (33)].

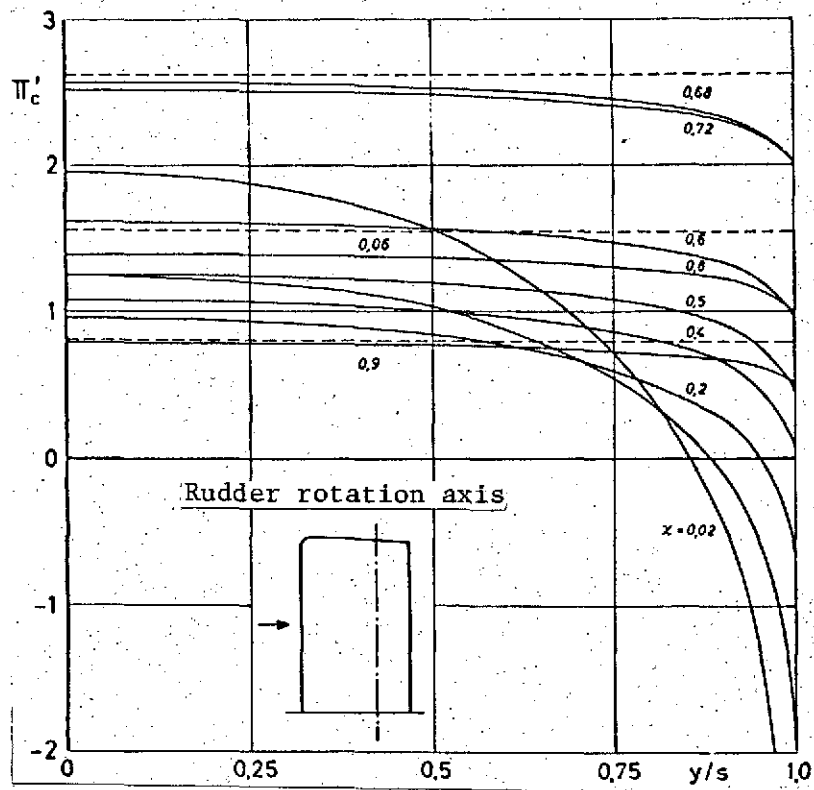


Figure 58. Theoretical pressure variation $\pi_c = \pi'_c + i\pi''_c$ in span direction over rectangular wing for rudder rotational oscillations. Real part π'_c ; $\Lambda = 3, 1$; $|\omega^*| = 0, 269$; — large aspect ratio theory; --- two-dimensional theory.

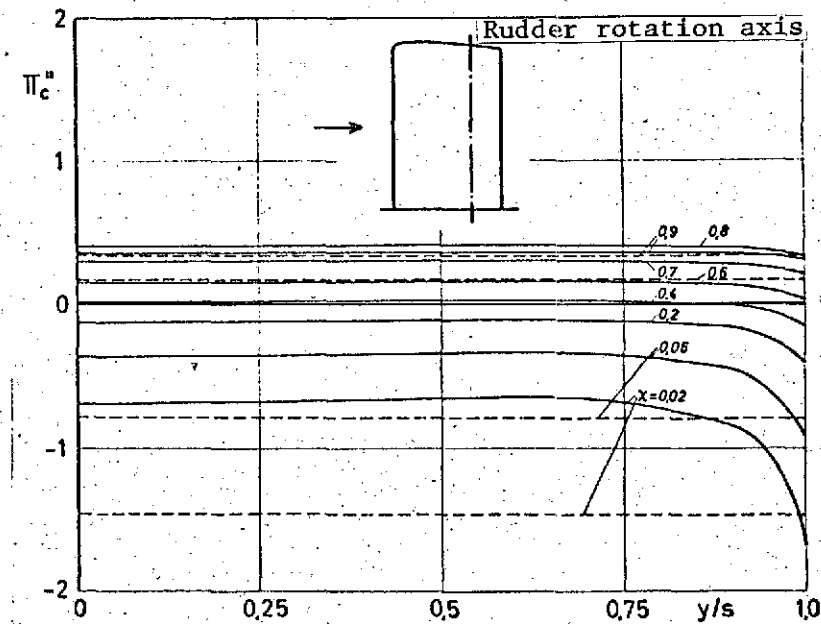


Figure 59. Theoretical pressure variation $\pi_c = \pi'_c + i\pi''_c$ in span direction over rectangular wing for rudder rotational oscillations. Imaginary part π''_c ; $\Lambda = 3, 1$; $|\omega^*| = 0, 269$; — large aspect ratio theory; --- two-dimensional theory.

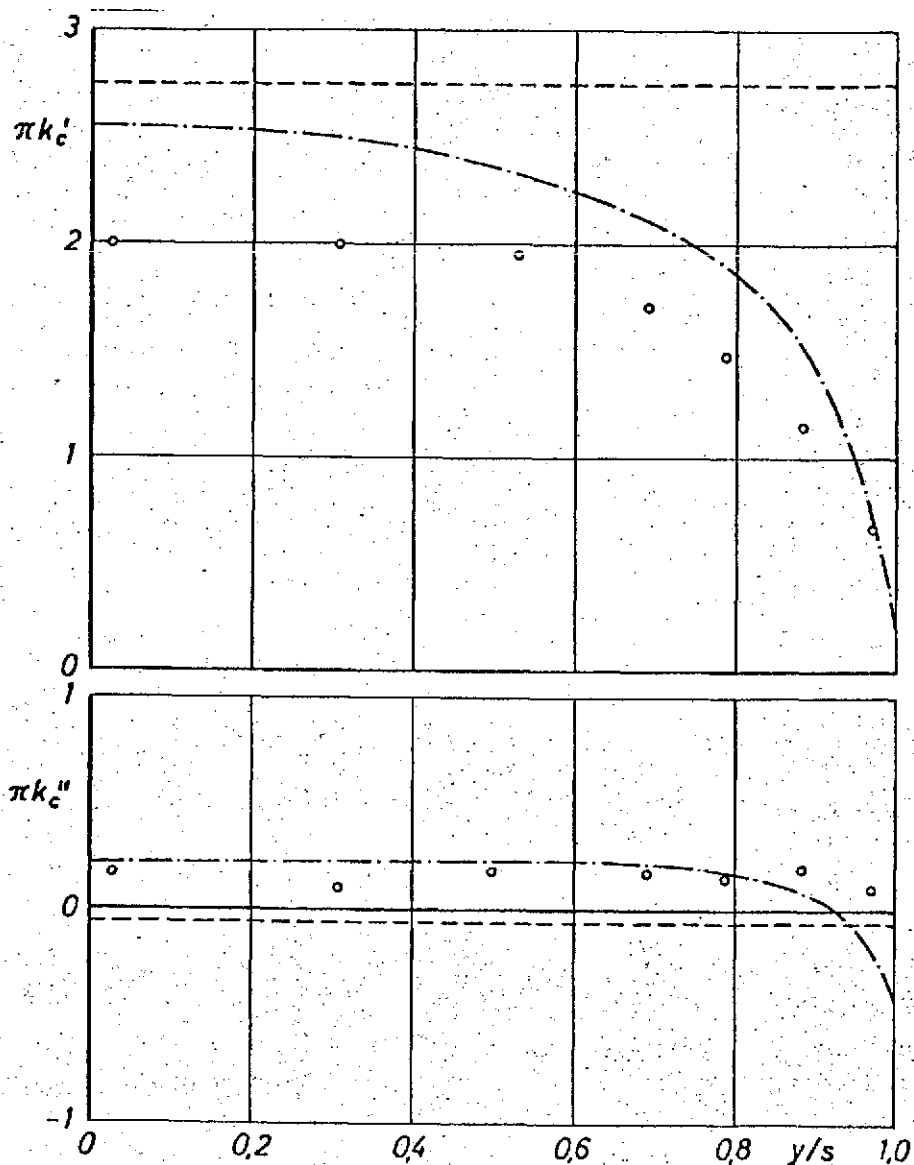


Figure 60. Distribution of wing aerodynamic force over rectangular wing for rudder rotational oscillations
 $\Lambda = 3, 1$; $\nu = 6$ Hz; $|\omega^*| = 0, 349$; o - measurement; -·- large aspect ratio theory; --- two-dimensional theory.

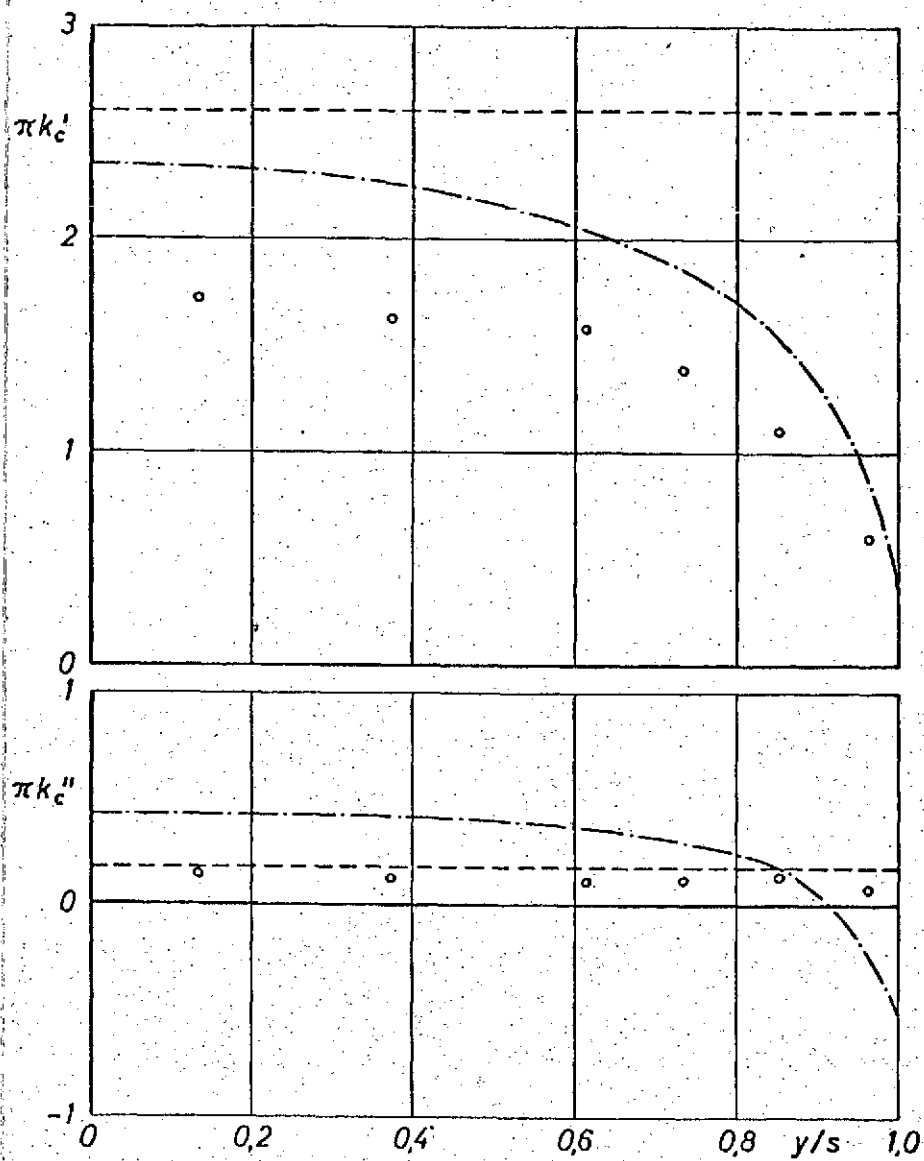


Figure 61. Distribution of wing aerodynamic force over rectangular wing for rudder rotational oscillations; $|\lambda| = 2.5$; $\nu = 10$ Hz; $|\omega^*| = 0.454$; o— measurement; --- large aspect ratio theory; --- two-dimensional theory.

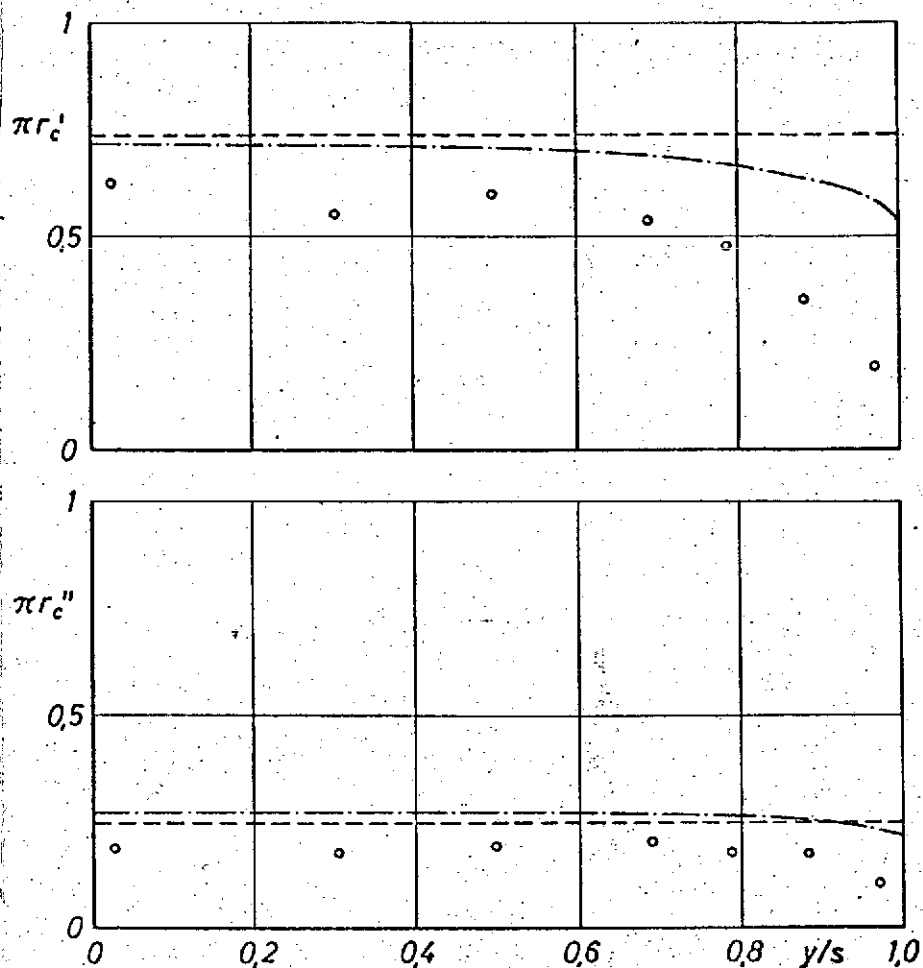


Figure 62. Distribution of rudder aerodynamic force over rectangular wing for rudder rotational oscillations ($\Lambda = 3, 1$; $\nu = 6 \text{ Hz}$; $|\omega^*| = 0,349$); o- measurement; --- large aspect ratio theory; --- two-dimensional theory.

Figures 64 to 67 show pressure distributions for rudder rotational oscillations of the sweptback wings. The measurement results do not deviate essentially from the results for the rectangular wings. The same is true for the large aspect ratio theory. Figures 66 and 67 show two pressure distributions at the same reduced frequency $|\omega^*| = 0.445$ but for different Reynolds numbers. For the real part, the measured values often coincide, whereas there are slight deviations in the imaginary

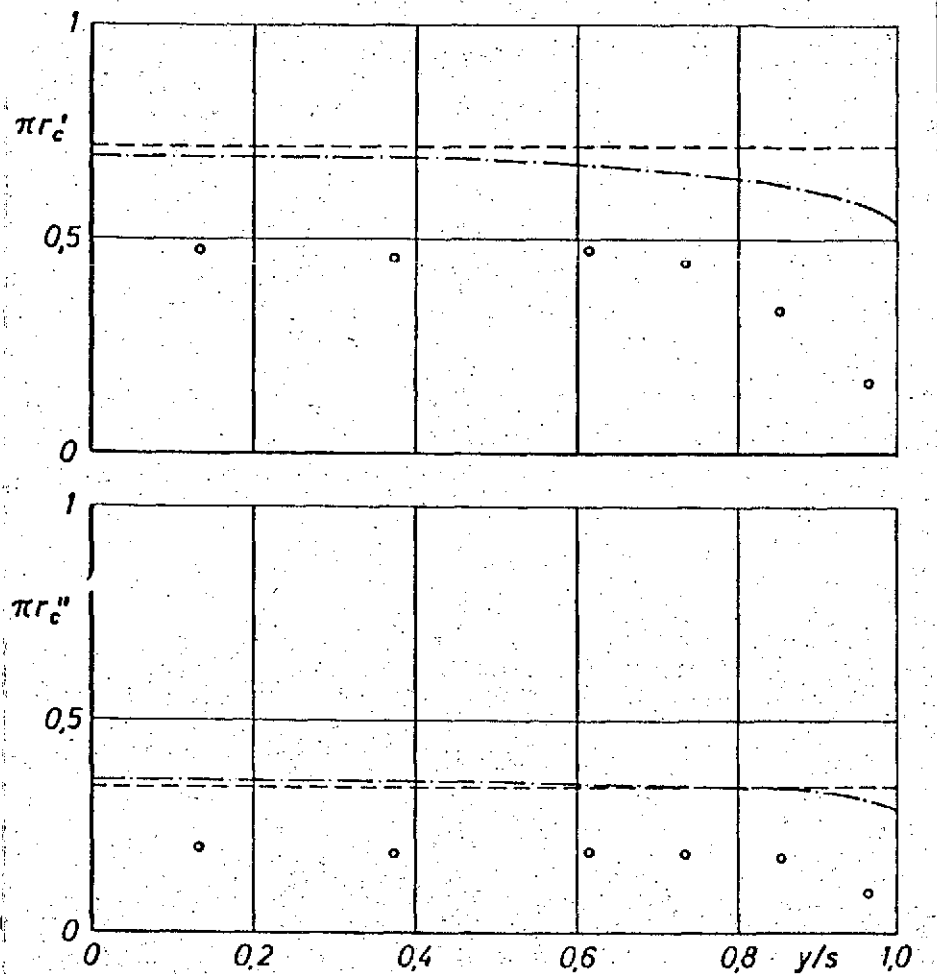
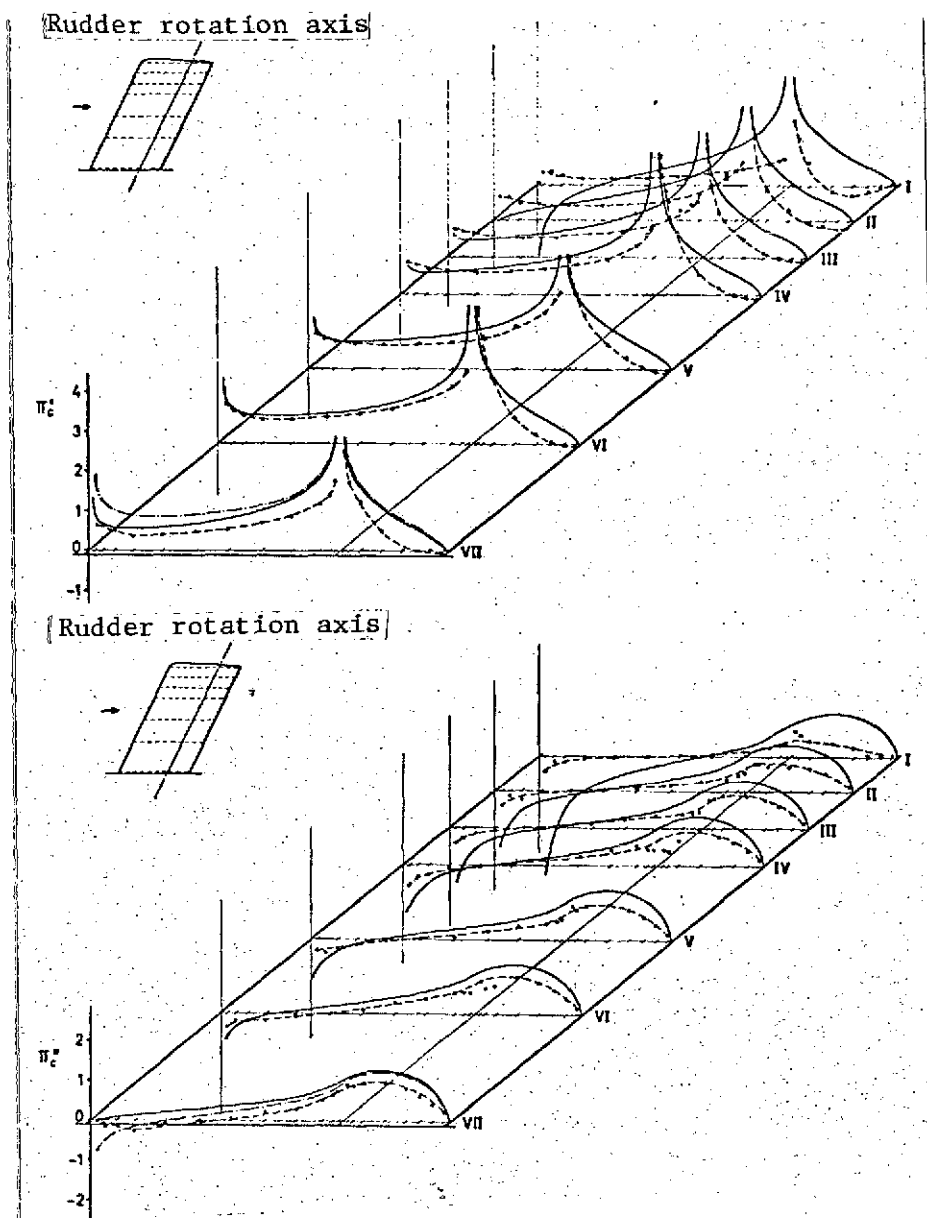
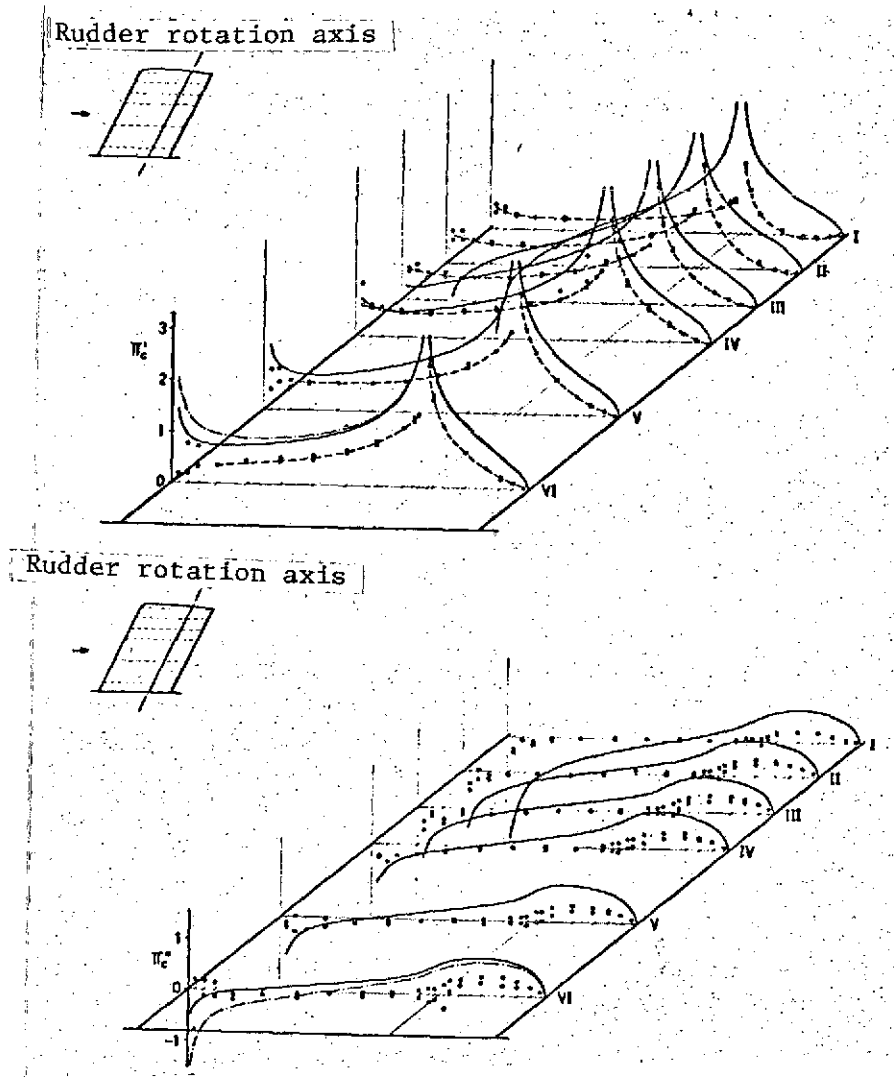


Figure 63. Distribution of rudder aerodynamic force over rectangular wing for rudder rotational oscillations $\Lambda = 2.5$; $\nu = 10$ Hz; $|\omega^*| = 0.454$; o- measurement; --- large aspect ratio theory; --- two-dimensional theory.

part. This deviation cannot be immediately attributed to the influence of a Reynolds number effect, because there is a certain scatter in the measured values, which is unavoidable because of the tunnel turbulence. On the other hand, any deviation of the measured value of the reference line would be transferred to all of the measured points.



Figures 64 and 65. Pressure distribution $|\pi_c' + i\pi_c''|$ over sweptback wing for rudder rotational oscillations; $\Lambda = 3.1$; $\nu = 6 \text{ Hz}$; $|\omega^*| = 0.752$; -O- measurement; — large aspect ratio theory; --- two-dimensional theory.



Figures 66 and 67. Pressure distribution $\pi_c = \pi_c' + i\pi_c''$ over sweptback wing for rudder rotational oscillations for two different Reynolds numbers: $\Lambda = 2.5$; $|\omega^*| = 0.445$

-○- $Re = 1.64 \cdot 10^6$; $\nu = 10 \text{ Hz}$ } measurement
 -●- $Re = 0.98 \cdot 10^6$; $\nu = 6 \text{ Hz}$ }
 — large aspect ratio theory; --- two-dimensional theory

As already established for the rectangular wings, the spatial derivatives are far below the theoretical values [32] for rudder rotational oscillations of the sweptback wing. This result is emphasized by plotting the aerodynamic and moment derivatives of both wing shapes, as was done in Figures 68 to 75. Here the measured aerodynamic force derivatives lie considerably below the values for the large aspect ratio theory already for the aspect ratio $\Lambda = 3.1$. At $\Lambda = 2.5$, they only amount to about 60% of the theory. The deviations of the moment derivatives are even larger. This fact can be seen from the pressure distribution over the rudder, because the measured values deviate the most from the theoretical values at the trailing edge; but here again, it is the pressures which have the greatest effect on the rudder moment. This phenomenon is primarily to be observed in the real part (see Figures 54, 56, 64, and 66). /96

The measurement results clearly show that the aerodynamic forces and moments on oscillating rudders cannot be given with sufficient accuracy even by the large aspect ratio theory. No usable results could be expected from the two-dimensional theory for this oscillation form, because there are clear deviations already when measurements are carried out with two-dimensional flow [39]. The reasons for this are primarily the influences of the friction boundary layer (Kutta condition) which is only considered phenomenologically in the theory. In addition, the effects of profile thickness and rudder slit play a role here, which is also not considered by the theory.

It is possible and likely that this discrepancy will be reduced by improving the solution methods of the three-dimensional lifting surface theory. The main task consists in the theoretical consideration of all the friction influences, which has not been successful up to the present. At the present time, nothing else

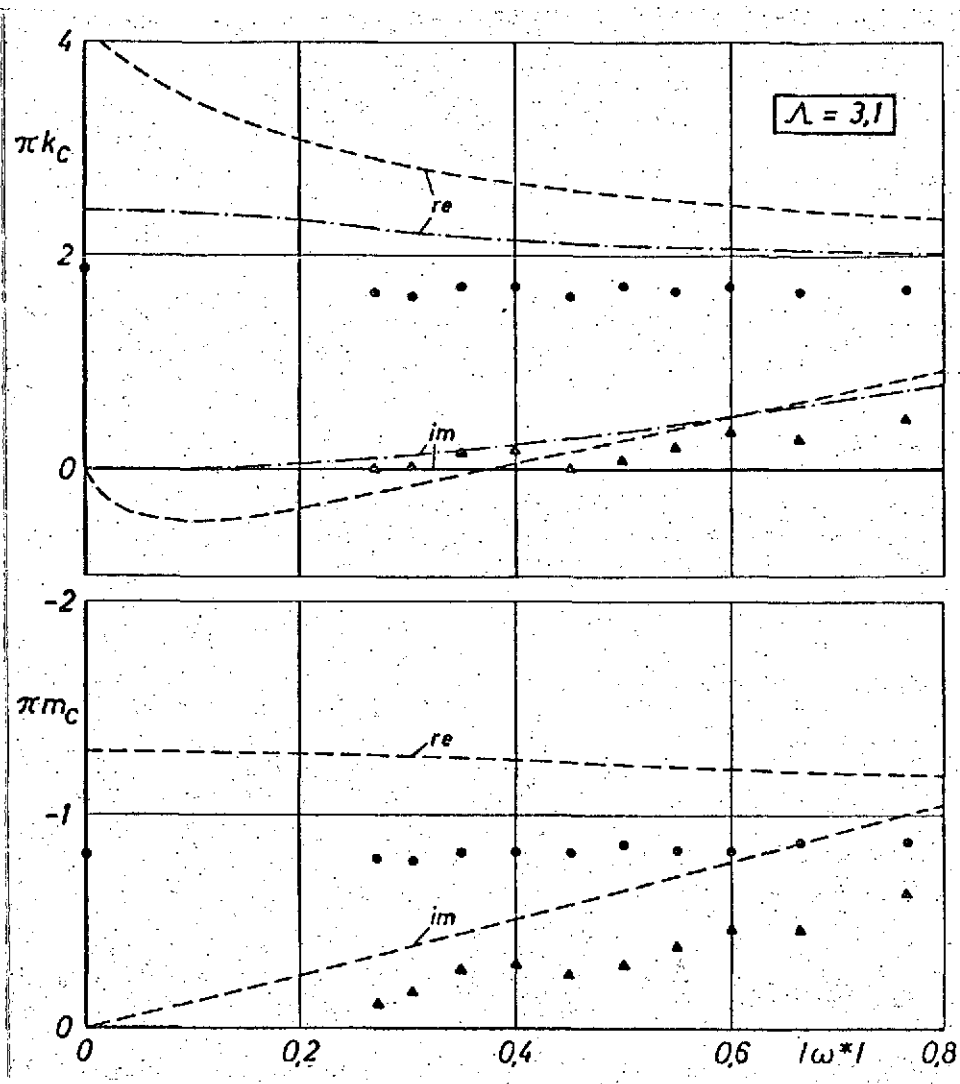


Figure 68. Global wing aerodynamic forces and moments over rectangular wing for rudder rotational oscillations.

●- real part
 ▲- imaginary part } measurement at $Re = 1,6 \cdot 10^6 - 0,55 \cdot 10^6$
 --- large aspect ratio theory; --- two-dimensional theory.

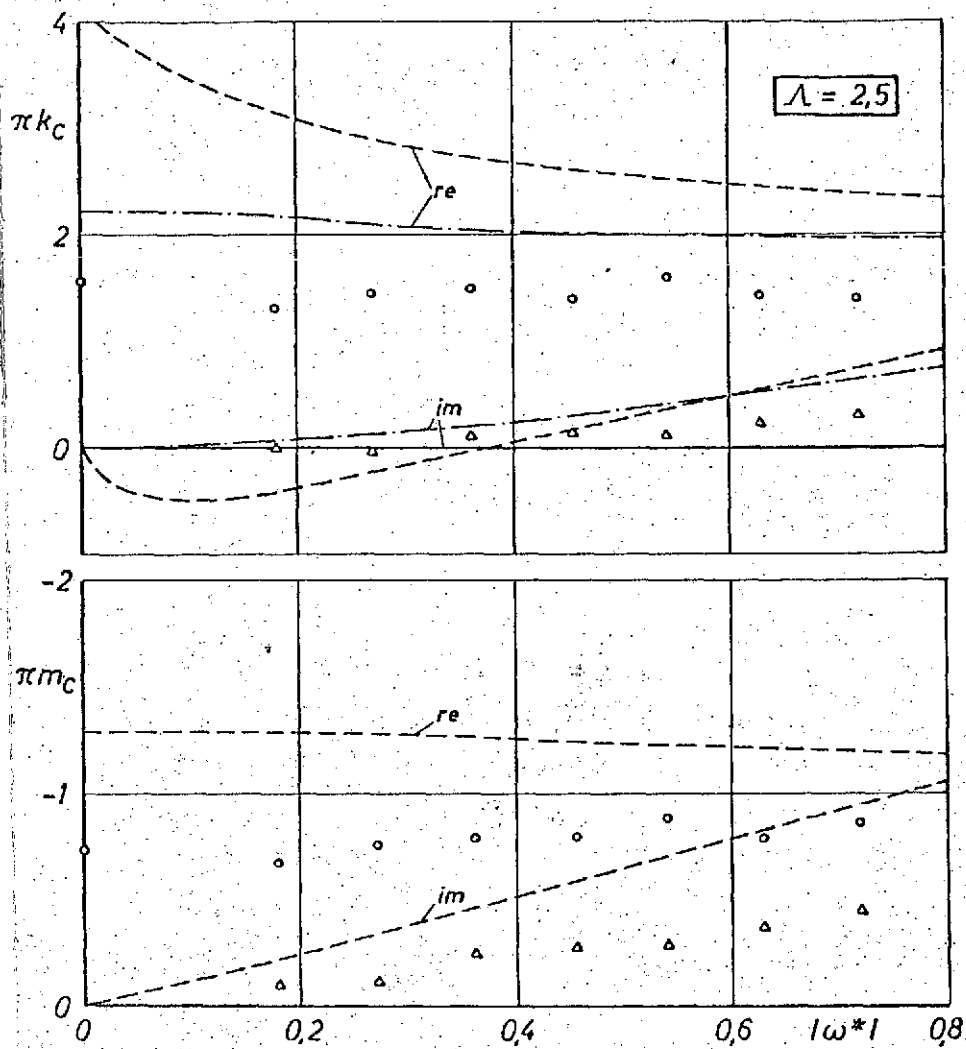


Figure 69. Global aerodynamic forces and moments over rectangular wing for rudder rotational oscillations.

o- real part
 Δ- imaginary part } measurement at $Re = 1.6 \cdot 10^6 = \text{const}$
 --- large aspect ratio theory
 -.- two-dimensional theory

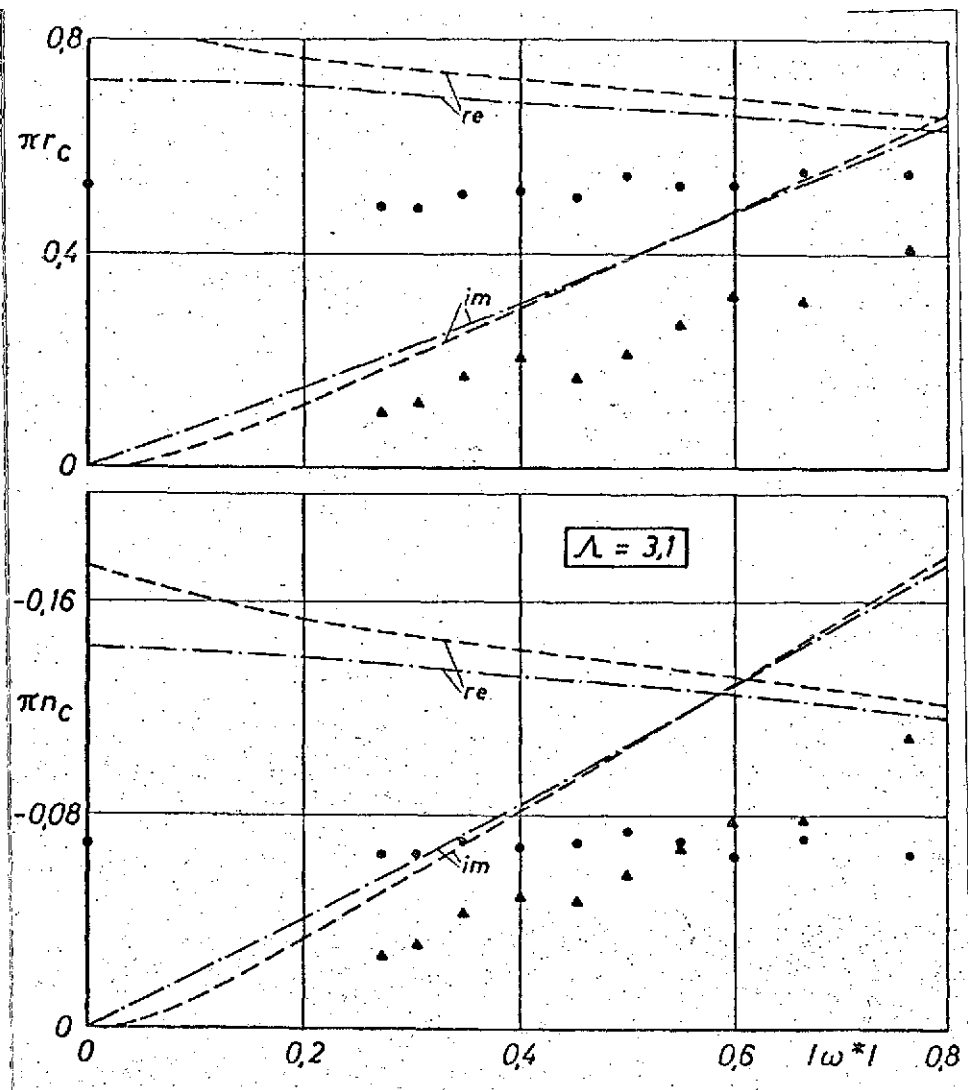


Figure 70. Global aerodynamic forces and moments over rectangular wing for rudder rotational oscillations.

- real part
 - ▲- imaginary part
 - large aspect ratio theory
 - two-dimensional theory
- } measurement at $Re = 1.6 \cdot 10^6 - 0.55 \cdot 10^6$

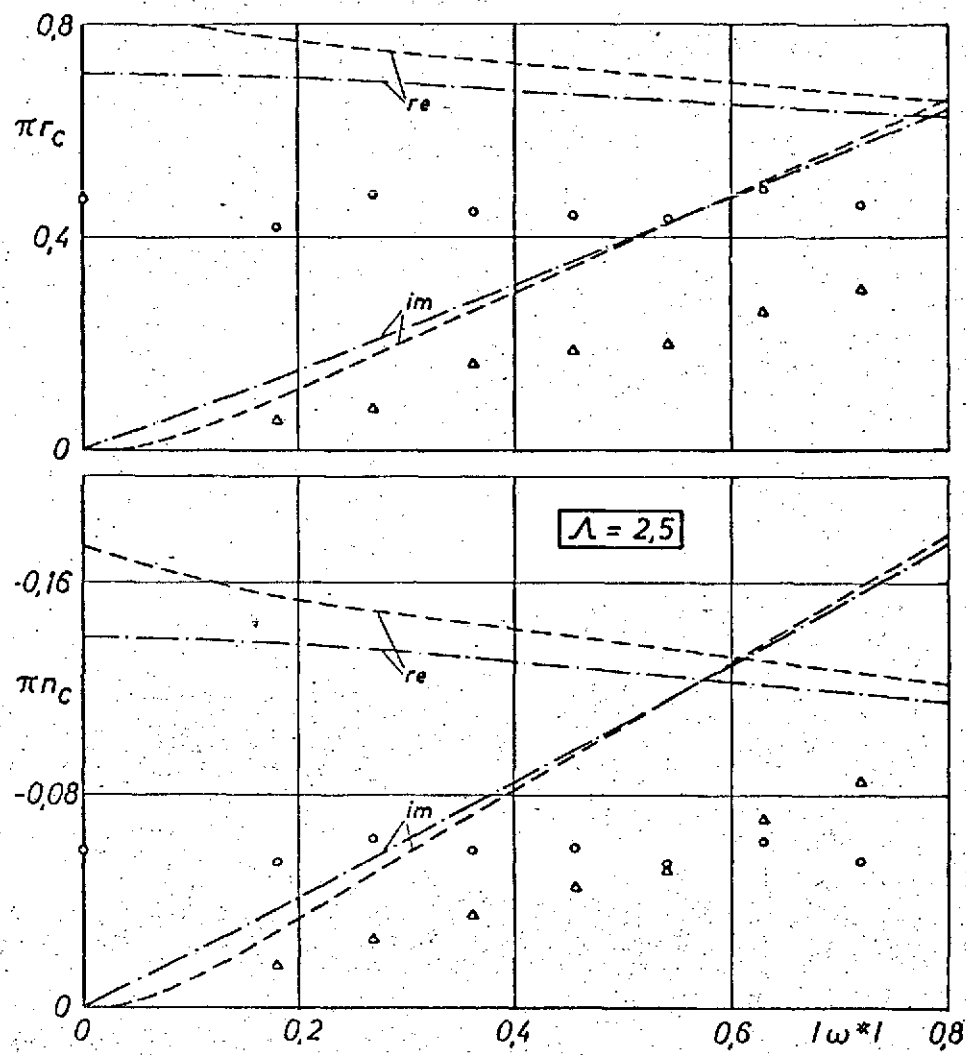


Figure 71. Global aerodynamic forces and moments over rectangular wing for rudder rotational oscillations.

o- real part
 Δ- imaginary part } measurement at $Re = 1,6 \cdot 10^6 = \text{const}$
 --- large aspect ratio theory
 -.- two-dimensional theory.

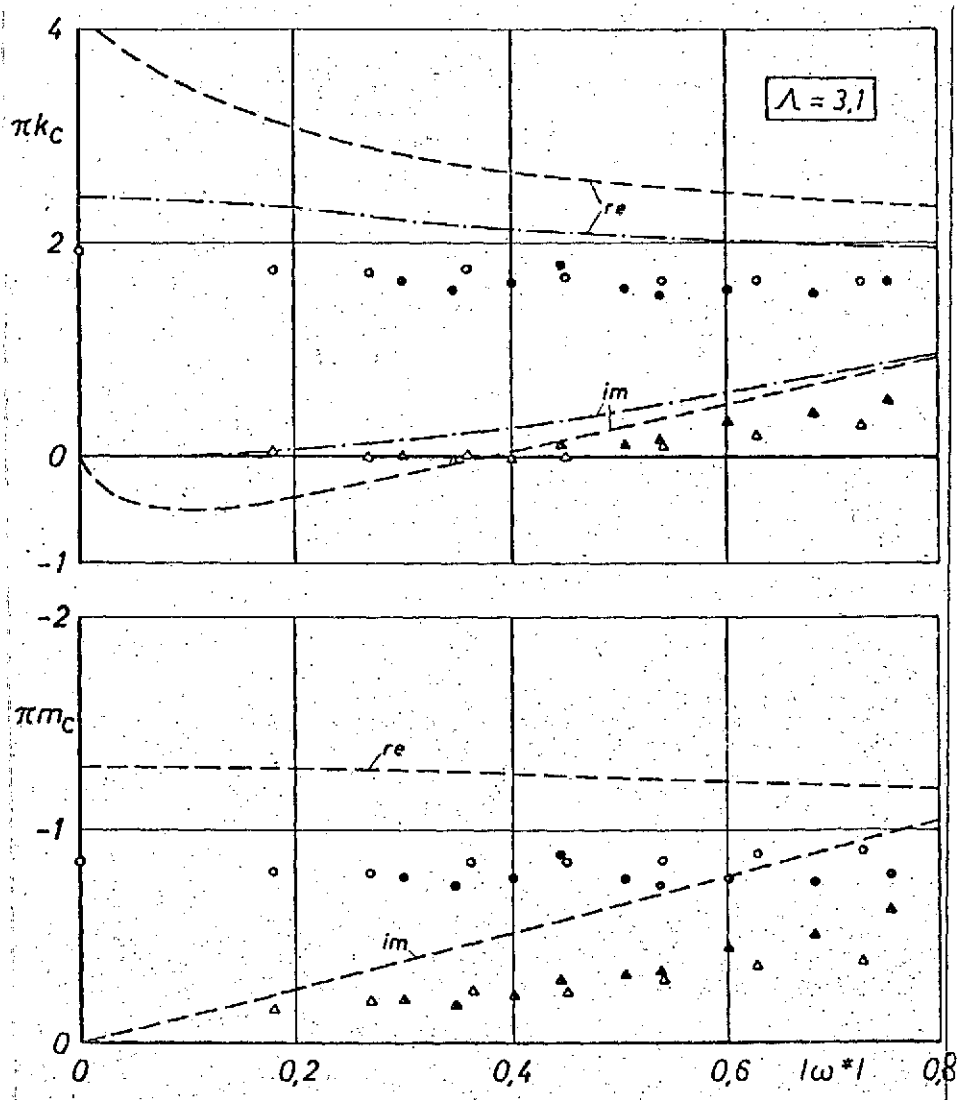


Figure 72. Global wing aerodynamic forces and moments over sweptback wing for rudder rotational oscillations.

- real part
 - △- imaginary part
 - real part
 - ▲- imaginary part
 - large aspect ratio theory
 - two-dimensional theory
- } measurement at $Re = 1,6 \cdot 10^6$ = const
 } measurement at $Re = 1,4 \cdot 10^6 - 0,55 \cdot 10^6$

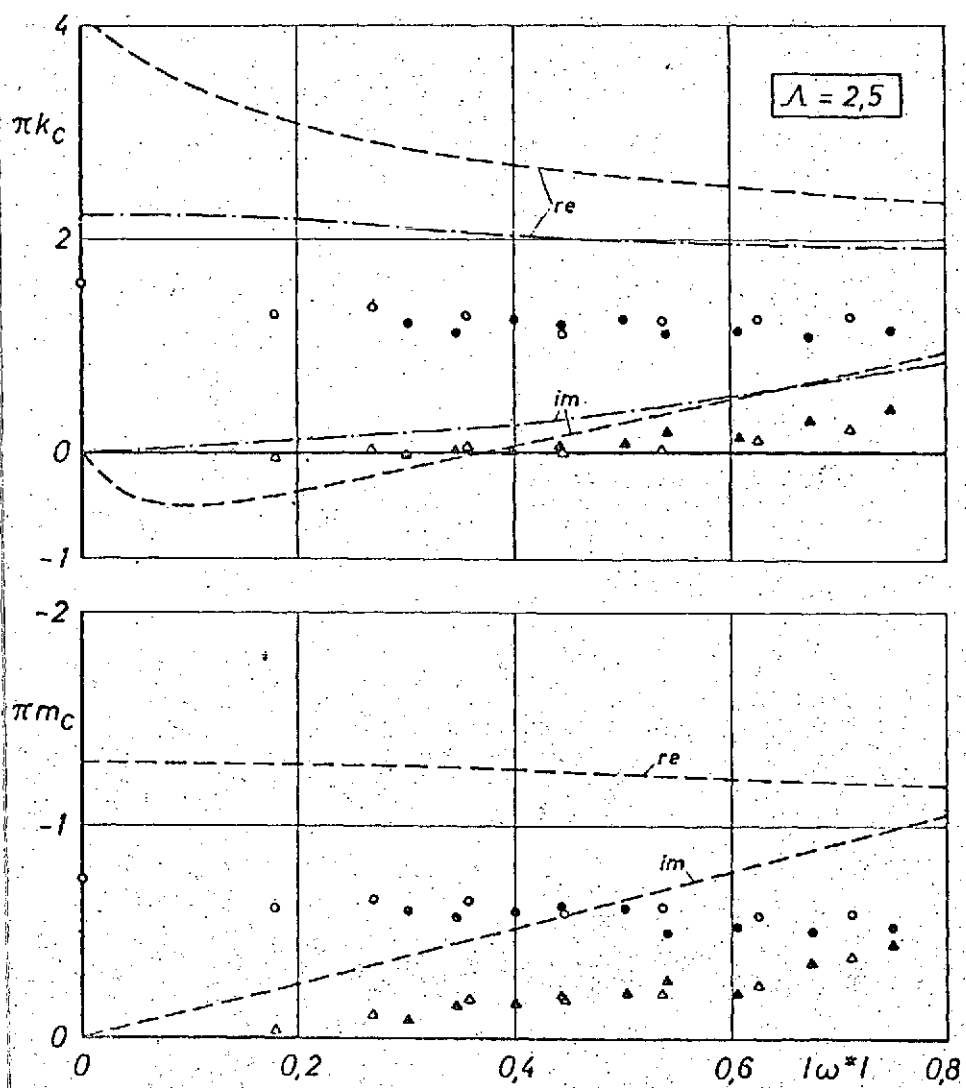


Figure 73. Global wing aerodynamic forces and moments over sweptback wing for rudder rotational oscillations.

- real part
 - △- imaginary part
 - real part
 - ▲- imaginary part
 - large aspect ratio theory
 - two-dimensional theory
- } measurement at $Re = 1,6 \cdot 10^6$ = const
 } measurement at $Re = 1,4 \cdot 10^6 - 0,55 \cdot 10^6$

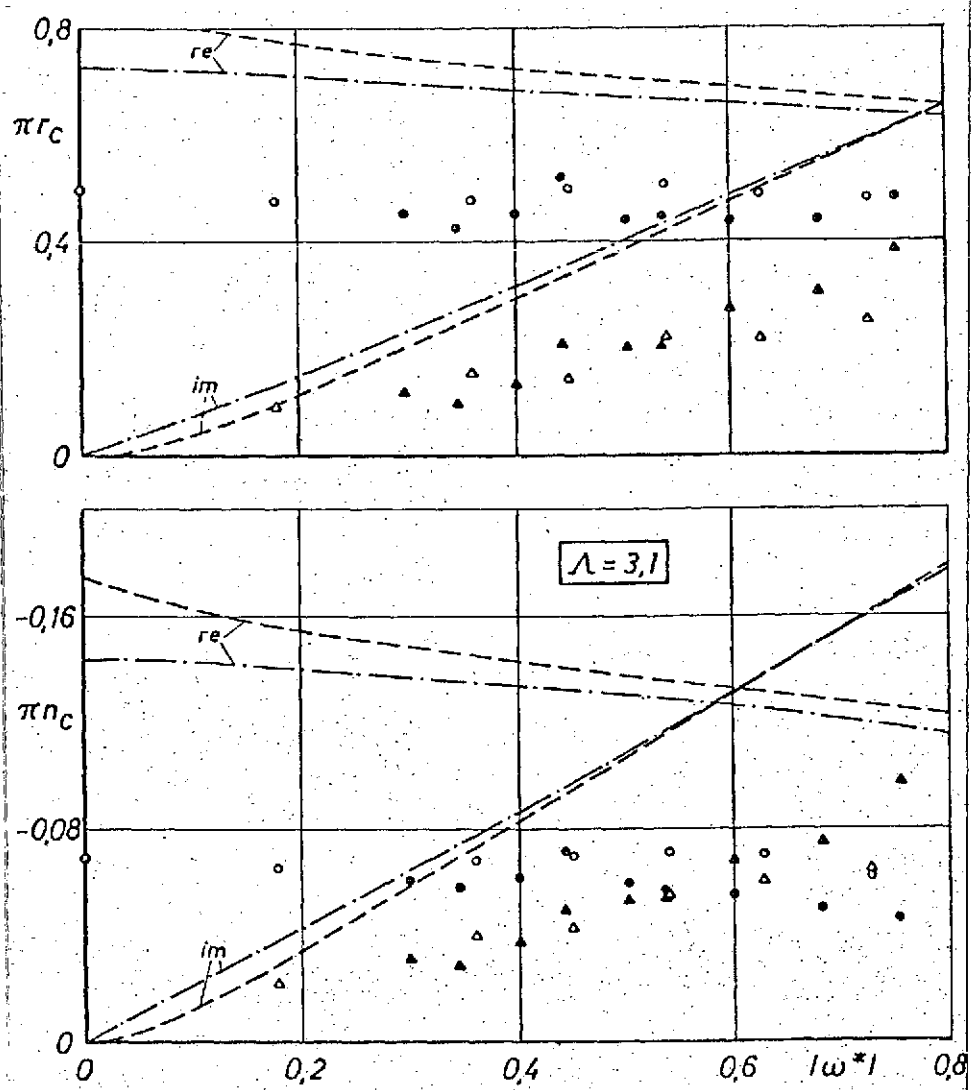


Figure 74. Global wing aerodynamic forces and moments over sweptback wing for rudder rotational oscillations.

- o- real part
 - Δ - imaginary part
 - real part
 - \blacktriangle - imaginary part
 - large aspect ratio theory
 - two-dimensional theory
- } measurement at $Re = 1,6 \cdot 10^6$ = const
 } measurement at $Re = 1,4 \cdot 10^6 - 0,55 \cdot 10^6$

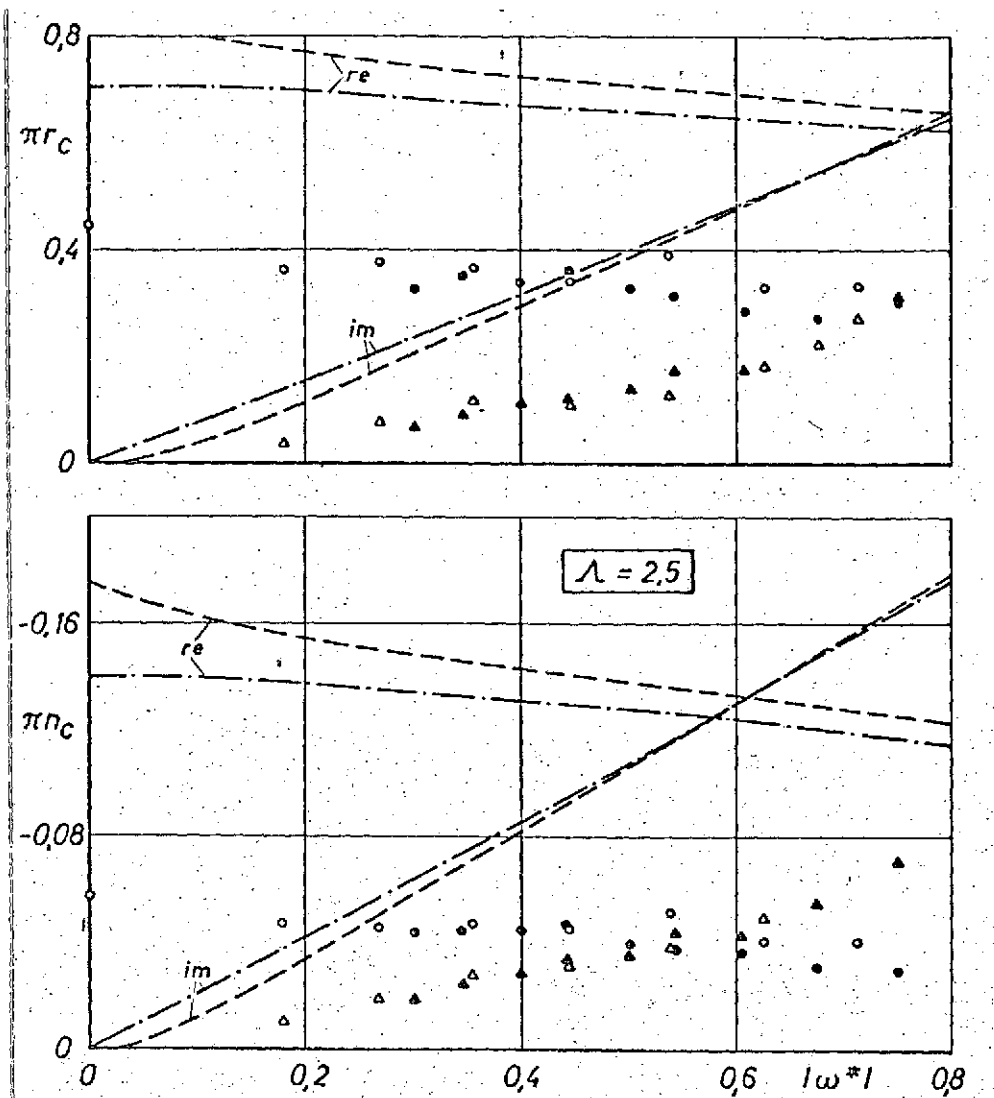


Figure 75. Global wing aerodynamic forces and moments over sweptback wing for rudder rotational oscillations.

o- real part
 Δ- imaginary part
 ●- real part
 ▲- imaginary part

} measurement at $Re = 1,6 \cdot 10^6$
 } measurement at $Re = 1,4 \cdot 10^6 - 0,55 \cdot 10^6$

--- large aspect ratio theory
 --- two-dimensional theory

can be done but to reduce the theoretical pressures by the correction factors, which can be obtained from the present measurements and similar ones made with other wings [42].

Figures 72 to 75 do not show a clear influence of Reynolds number. Considering the large deviations between the measured results and the theories considered, one can at least say that a possible Reynolds number influence will continue to be negligible as long as no better theory becomes available.

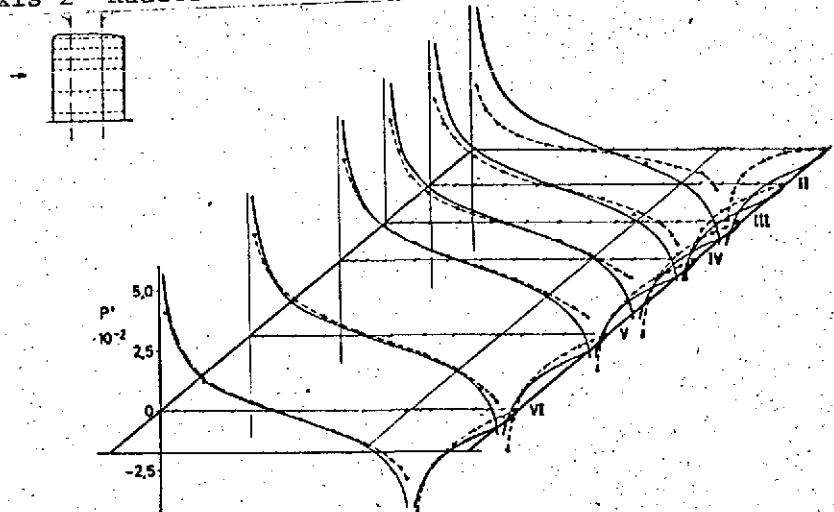
/105

7.3.4. Simultaneous fin and rudder rotation

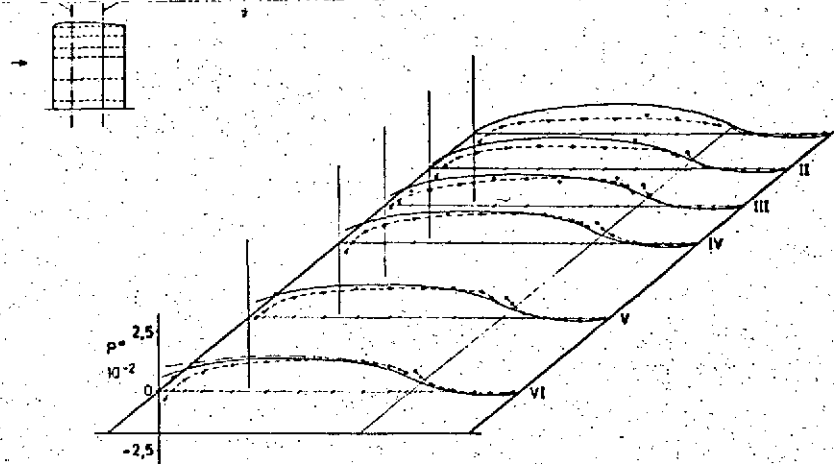
Figures 76 and 77 show a pressure distribution for simultaneous fin and rudder oscillations of the rectangle model. The phase angle between the oscillation forms is 180° . The fin carries out rotational motions around the neutral axis. The rotational amplitude of the rudder is almost twice as great as that of the fin. Therefore, the singularity at the rudder slit is just as pronounced. Except for the outermost section, the agreement between measured values and large aspect ratio theory is very good. The reason for this is probably that the deviations of the theory for pure wing oscillations and for pure rudder oscillations cancel to an increased degree when both oscillation forms are superimposed, the more the phase displacement approaches 180° . This is also true for the two-dimensional theory in the area of the wing root. For the case where the phase displacement between the two oscillation forms vanishes, we should expect an addition of the theoretical deviations.

The measurement confirms the superposition principle of the two theories under consideration. As far as flutter calculations are concerned, it is remarkable that the deficiencies of the large aspect ratio theory for rudder oscillations discussed in

Rotation axis 2 Rudder rotation axis



Rotation axis 2 Rudder rotation axis



Figures 76 and 77. Pressure Distribution $P = P' + iP''$ over rectangular wing for simultaneous rotational oscillations around axis 2 and around the rudder rotational axis ($\Lambda = 2,5$; $\delta = 180^\circ$; $\nu = 6 \text{ Hz}$; $|\omega^*| = 0,555$; $B = 0,0079$; $C = 0,0140$)

-o- measurement; — large aspect ratio theory; --- two-dimensional theory.

the previous section are not as serious as they first appear, because aircraft rudders are often tuned so softly that they will oscillate out of phase with the fin. Apparently, the large aspect ratio theory would produce good results in flutter calculations of such aircraft.

8. Summary

/107

Numerous pressure distribution measurements over oscillating half-wing models in incompressible flow were carried out for an experimental test of three unsteady lifting surface theories. We have considered a lifting surface theory, a lifting line theory, and the exact two-dimensional theory. The measurements were done on a rectangular wing and a sweptback wing model with a constant chord of $l = 0.6$ m. The sweepback of the sweptback wing was 25° . In addition, we measured a wing with a full span rudder with a constant rudder chord of 30% of wing chord. All wings had a NACA 0012 profile. The models were attached perpendicularly to a plate in the form of half-wings. The plate extended from the lower edge of the wind tunnel nozzle through the free test section up to the capture funnel. The plate has the function of a symmetry plane, and the half-model can be considered to be reflected at this plane. The aspect ratio of the models could be reduced from $\Lambda = 3.1$ to $\Lambda = 2.5$.

The models were excited to perform pitch oscillations around various axes perpendicular to the incident flow direction. Also, rudder rotational oscillations around the rudder leading edge were performed. Measurements of simultaneous fin and rudder rotational motions were carried out for the rectangular wing as well. The wind tunnel measurements were carried out at the reduced frequencies $|\omega^*| = 0.13$ to 0.76 , as well as for steady flow ($\omega^* = 0$). They were complemented by measurements of oscillations in quiet air.

In the case of wing pitch oscillations, the measurement results agree well with the lifting surface method. The theory of the large aspect ratio lifting surface (lifting line method) is quite favorable. It represents an essential improvement of the two-dimensional theory.

In the case of rudder rotational oscillations, the large aspect ratio theory produces good agreement for the aspect ratio $\Lambda = 3.1$. At $\Lambda = 2.5$, the deviations are quite large, however, Especially the measured derivatives of the rudder aerodynamic force and the rudder moment are considerably below the theoretical values. These deviations are probably primarily due to the friction influences which are ignored in the theory. However, we were not able to establish any noticeable influence of Reynolds number on the measurement results for the investigated range between $Re = 0.55 \cdot 10^6$ to $1.6 \cdot 10^6$.

/108

When there are simultaneous rotational oscillations of the fin and of the rudder, the measured pressure distribution agrees well with the large aspect ratio theory. The reason for this is that the deviations in the theory for pure wing oscillations and for pure rudder oscillations cancel to a considerable extent when these two oscillation forms are superimposed, if the oscillations are performed out of phase, that is, with a phase displacement of 180° .

9. References

/109

1. Watkins, C. E., H. L. Runyan, and D. S. Woolston. On the Kernel Function of the Integral Equation Relating the Lift and Downwash Distributions of Oscillating Finite Wings in Subsonic Flow. NACA Rep. 1234, (1955).

2. Watkins, C. E., D. S. Woolston, and H. J. Cunningham. A Systematic Kernel Function Procedure for Determining Aerodynamic Forces on Oscillating or Steady Finite Wings at Subsonic Speeds. NASA TR-R-48, 1959.
3. Laschka, B. The Theory of Harmonically Oscillating Lifting Surface for Subsonic Flow. Z. flugwiss, Vol. 11, 1963, pp. 265 - 292.
4. Runyan, H. L., and D. S. Woolston. Method for Calculating the Aerodynamic Loading on an Oscillating Finite Wing in Subsonic and Sonic Flow. NACA TR 1322, 1957.
5. Stark, V. J. E. A Method for Solving the Subsonic Problem of the Oscillating Finite Wing with the Aid of High Speed Digital Computers. SAAB TN 41, 1958.
6. Stark, V. J. E. Aerodynamic Forces on a Rectangular Wing Oscillating in Subsonic Flow. SAAB TN 44, 1960.
7. Kuessner, H. G., and L. Schwarz. The Oscillating Wing with Aerodynamically Balanced Rudder. Luftfahrtforschung, Vol. 17, 1940, pp. 337 - 354.
8. Kuessner, H. G. A Review of the Two-Dimensional Problem of the Unsteady Lifting Surface Theory during the Last Thirty Years. Inst. for Fluid Dynamics and Applied Mathematics, University of Maryland, Lecture Ser. No. 23, April, 1953.
9. Kuessner, H. G. General Lifting Surface Theory. Luftfahrtforschung, Vol. 17, 1940, pp. 370 - 379.
10. Dingel, M.; and H. G. Kuessner. Large Aspect Ratio Oscillating Lifting Surface. AVA Report 41/6/17, 1941. Dtsch. Luftfahrtforschung, FB 1774, 1943.
11. Reissner, E. Effects of Finite Span on the Airload Distribution for Oscillating Wings. I. Aerodynamic Theory of Oscillating Wings of Finite Span. NACA TN 1194, 1947. /110
12. Kuessner, H. G., and H. Hertrich. Theory of the Large Aspect Ratio Oscillating with the Surface. DLR-FB 64-19, 1965.
13. Kuessner, H. G., and H. Hertrich. Approximate Theory of the Large Aspect Ratio Oscillating Lifting Surface in the Subsonic Range with Computation Examples. Jb. 1965, of the WGLR, pp. 268 - 275.

14. Kuessner, H. G., and H. Goellnitz. Tables of Aerodynamic Derivatives of the Oscillating Segment Profile with Bends and Depths. DLR-FB 64-05, 1964.
15. Goellnitz, H. Tables and Diagrams of the Auxiliary Functions S_n for the Theory of the Large Aspect Ratio Oscillating Lifting Surface. DLR-FB 64-20, 1965.
16. Drescher, H. Pressure Distribution Measurements of a Lifting Wing with Slit Flap for Fast Change of the Flap Deflection. Dtsch. Luftfahrtforschung, FB 1082, 1937.
17. Drescher, H. Experimental Determination of the Aerodynamic Reaction on a Wing with an Oscillating Rudder. Dissertation TH Graz 1949, Oesterr. Ing.-Arch., Vol. IV, NO. 3/4, 1950, pp. 270 - 290.
18. Molyneux, W. G., and F. Ruddlesden. A Technique for the Measurement of Pressure Distribution on Oscillating Aerofoils with Results for a Rectangular Wing of Aspect Ratio 3.3. ARC C.P. 233, 1955.
19. Laidlaw, W. R. Experimental Pressure Distributions on Oscillating Low Aspect Ratio Wings. I.A.S. Preprint No. 499, 1955.
20. Bergh, H. Unsteady Pressure Measurements on a Wing with an Oscillating Flap in Two-Dimensional Incompressible Flow. NLL-TM F.217, 1958.
21. Destuynder, R. A Method for Interpretation of Unsteady Pressure Measurements. Communication presented at the Nineteenth Meeting of the Materials and Structures Group of the AGARD, Paris, October 12 - 17, 1964. /111
22. Rainey, G. Measurement of Aerodynamic Forces for Various Mean Angles of Attack on an Airfoil Oscillating in Pitch and on Two Finite Span Wings Oscillating in Bending with Emphasis on Damping in the Stall. NACA Report 1305, 1957.
23. Bergh, H. A New Method for Measuring the Pressure Distribution on Harmonically Oscillating Wings of Arbitrary Planform. Vortrag auf dem IV. Kongress des International Council of the Aeronautical Sciences (ICAS), Paris; August 24 - 28, 1964.

24. Lessing, H. C., J. L. Troutman, and G. P. Menees. Experimental Determination of the Pressure Distribution on a Rectangular Wing Oscillating in the First Bending Mode for Mach Numbers from 0.24 to 1.30. NASA TN D-344, 1960.
25. Destuynder, R., and J. Bony. New Measurement Chain for Unsteady Pressure. La Rech. Aerospatiale, No. 99, 1964, pp. 49 - 50.
26. Iberall, A. S. Attenuation of Oscillatory Pressures in Instrument Lines. J. Res. Nat. Bureau Stand., RP 2115, Vol. 45, 1950.
27. Bergh, H., and H. Tijdemann. Theoretical and Experimental Results for the Dynamic Response of Pressure Measure Systems. NLR-TR F.238, 1965.
28. Hertrich, H. Experimental Determination of Aerodynamic Reactions with Oscillating Half-Wing Models in the Subsonic Wind Tunnel. Part I: Description and Theoretical Investigation of the Planned Test Stand. AVA Report 64 J 10, 1964.
29. Hertrich, H. Experimental Determination of Aerodynamic Reactions with Oscillating Half-Wing Models in the Subsonic Wind Tunnel. Part II: Measurements with a Rectangular Wing. AVA Report 65 J 10, 1965. /112
30. Hertrich, H. Experimental Determination of Aerodynamic Reactions with Oscillating Half-Wing Models in the Subsonic Wind Tunnel. Part III: Measurements with a Rectangular Wing with Rudder. AVA Report 66 J 08, 1966.
31. Hertrich, H. Experimental Determination of Aerodynamic Reactions with Oscillating Half-Wing Models in the Subsonic Wind Tunnel. Part IV: Measurements with a Sweptback Wing. AVA Report 66 J 09, 1966.
32. Hertrich, H. Experimental Determination of Aerodynamic Reactions with Oscillating Half-Wing Models in the Subsonic Wind Tunnel. Part V: Measurements with a Sweptback Wing with a Rudder. AVA Report 66 J 10, 1966.
33. Wagener, J. Development of an Automatic Measurement Installation for Determining Unsteady Pressure Distributions. AVA Report 66 J 03, 1966.

34. Hertrich, H., and J. Wagener. A Method for Measuring and Automatic Recording of Unsteady Pressure Distributions. DLR-FB 67-54, 1967.
35. Truckenbrodt, E. Lifting Surface Theory for Incompressible Flow. Jb. 1953 of the WGL, pp. 40 - 65.
36. Multhopp, H. Methods for Calculating the Lift Distribution of Wings (Subsonic Lifting Surface Theory). ARC R. and M. 2884, 1955.
37. Hertrich, H. Pressure Distribution Measurements of Semi-wing Models with a Rudder in Unsteady Subsonic Flow. AVA Report 66 J 12.
38. Laschka, B. The Pressure, Lift, and Moment Distribution over a Harmonically Oscillating Sweptback Wing with Small Aspect Ratio in the Low Subsonic Range. Comparison between Theory and Measurement. Lecture at the IV Congress of the International Council of the Aeronautical Sciences (ICAS), Paris, August 24 - 28, 1964. /113
39. Bergh, H. Results of Pressure Measurements on a Three-Part Wing-Tube Combination in Incompressible Flow. NLR-Verslag FF 12, 1963.
40. Lohmann, K. Calculation of Pressure Distribution for Finite Span Oscillating Lifting Surfaces for Compressible Subsonic Flow. AVA Report 66 J 05, 1967.
41. Triebstein, H. Calculation of Pressure Distribution According to the Theory of the Oscillating Lifting Surface with a Large Aspect Ratio. AVA Report 65 J 09, 1966.
42. Gyett, P. R. Empirical Values of Derivatives. Manual on Aeroelasticity, Vol. II, 1961, Chapter 11.
43. Scholz, N. Force and Pressure Distribution Measurements for Small Aspect Ratio Lifting surfaces. Dissertation TH Braunschweig, 1949. Forsch. Ing.-Wes., Vol. 16, 1949-50, pp. 85 - 91.
44. Fuetterer, H. Measurement of the Lifting Increases of Five Symmetric Wings with End Dics. AVA Report 62 A 26.

APPENDIX

Auxiliary Functions $\Phi_n(\varphi)$

/114

$$\Phi_1(\varphi) = \pi - \varphi + \sin \varphi$$

$$\Phi_2(\varphi) = (\pi - \varphi) (1 + 2 \cos \varphi) + \sin \varphi (2 + \cos \varphi)$$

$$\Phi_3(\varphi) = \pi - \varphi + \sin \varphi \cos \varphi$$

$$\Phi_4(\varphi) = (\pi - \varphi) \cdot 2 \cos \varphi + \sin \varphi \cdot \frac{2}{3} (2 + \cos^2 \varphi)$$

$$\Phi_5(\varphi) = \sin \varphi \cdot (1 - \cos \varphi)$$

$$\Phi_6(\varphi) = 2(\pi - \varphi) + \sin \varphi \cdot \frac{2}{3} (2 - \cos \varphi) (1 + 2 \cos \varphi)$$

$$\begin{aligned} \Phi_7(\varphi) &= (\pi - \varphi) \left(\frac{1}{2} + 2 \cos \varphi \right) \\ &+ \sin \varphi \cdot \frac{1}{6} (8 + 5 \cos \varphi + 4 \cos^2 \varphi - 2 \cos^3 \varphi) \end{aligned}$$

$$\Phi_8(\varphi) = (\pi - \varphi) (-1 + 2 \cos \varphi) + \sin \varphi (2 - \cos \varphi)$$

$$\Phi_{10}(\varphi) = \Phi_{31}(\varphi) \cdot \Phi_5(\varphi)$$

$$\Phi_{11}(\varphi) = \Phi_2(\varphi) \cdot \Phi_3(\varphi)$$

$$\begin{aligned} \Phi_{12}(\varphi) &= (\pi - \varphi)^2 \left(\frac{1}{2} + 4 \cos^2 \varphi \right) + (\pi - \varphi) \sin \varphi \cos \varphi \\ &\cdot (7 + 2 \cos^2 \varphi) + \sin^2 \varphi \left(2 + \frac{5}{2} \cos^2 \varphi \right) \end{aligned}$$

$$\Phi_{31}(\varphi) = \pi - \varphi - \sin \varphi$$

$$\Phi_{32}(\varphi) = \pi - \varphi + \sin \varphi (1 + 2 \cos \varphi)$$

$$\Phi_{33}(\varphi) = 2 \sin^2 \varphi$$

$$\Phi_{36}(\varphi) = \Phi_{32}(\varphi) \cdot \Phi_3(\varphi) + 2 \sin^4 \varphi$$

$$\Phi_{37}(\varphi) = \Phi_3(\varphi) \cdot [\Phi_2(\varphi) - \Phi_3(\varphi)]$$